



UNIVERSITÀ  
DEGLI STUDI  
FIRENZE

DOTTORATO DI RICERCA IN

SPETTROSCOPIA ATOMICA E MOLECOLARE  
ATOMIC AND MOLECULAR SPECTROSCOPY

CICLO XXVI

COORDINATORE PROF. PAVONE FRANCESCO SAVERIO

**STRUCTURE AND REACTIVITY OF MODEL  
MOLECULES UNDER PRESSURE BY NON-LINEAR  
SPECTROSCOPY**

SETTORE DISCIPLINARE CHIM/02

Dottorando

DOTT. FANETTI SAMUELE

Tutore

PROF. BINI ROBERTO

Coordinatore

PROF. PAVONE FRANCESCO SAVERIO

Anni 2011/2013



*Take into account that great love and great achievements involve great risk.*

*Tenzin Gyatso, the 14<sup>th</sup> Dalai Lama*





# Contents

<b>Introduction</b>	<b>1</b>
<b>1 Two photon induced fluorescence and reactivity of model aromatics</b>	<b>9</b>
1.1 Benzene . . . . .	9
1.2 Pyridine . . . . .	14
1.2.1 High pressure polymorphism . . . . .	14
1.2.2 High pressure and photoinduced reactivity . . . . .	22
1.2.3 Electronic properties . . . . .	25
1.2.4 Summary . . . . .	34
1.3 Triazine . . . . .	37
1.3.1 Electronic properties . . . . .	41
1.3.2 Summary . . . . .	45
1.4 Picene . . . . .	46
1.4.1 Single molecule and crystal electronic properties . . . . .	46
1.4.2 Pressure evolution of electronic structure . . . . .	54
1.4.3 Chemical reactivity . . . . .	60
1.4.4 Summary . . . . .	63
<b>2 Two photon induced reactivity of simple R-OH molecules</b>	<b>65</b>
2.1 Electronic properties of R-OH . . . . .	65
2.2 Ethanol . . . . .	67
2.2.1 Photoinduced reactivity of fully hydrogenated ethanol . . .	67

2.2.2	Isotopically marked ethanol: enlightening the effect of pressure on the excited electronic states . . . . .	73
2.3	Methanol . . . . .	77
2.3.1	Photoinduced reactivity and product identification . . . . .	77
2.3.2	Pressure effects on the reaction mechanisms . . . . .	79
2.4	Summary . . . . .	84
<b>3</b>	<b>Water dynamics by ultrafast transient infrared spectroscopy</b>	<b>87</b>
3.1	Anomalous behaviours of water . . . . .	87
3.2	Rotational and vibrational dynamics of water . . . . .	92
3.2.1	Infrared analysis of water stretching mode . . . . .	99
3.2.2	Computational analysis and data interpretation . . . . .	102
3.3	Summary . . . . .	109
<b>4</b>	<b>Experimental setup</b>	<b>111</b>
4.1	FT-IR . . . . .	111
4.2	Raman . . . . .	113
4.3	Two photon induced fluorescence . . . . .	115
4.4	Femtosecond transient IR (TRIR) . . . . .	118
	<b>Conclusions</b>	<b>121</b>
	<b>List of publications</b>	<b>127</b>
	<b>Bibliography</b>	<b>129</b>

# Introduction

Chemistry and physics of any system are governed by the chemical potential and by the thermodynamical variables. Among them, pressure is a powerful tool to rule the behaviour of molecular systems, which are known to have high compressibility [1, 2]. The effect of an external pressure is to induce in this kind of systems a remarkable reduction of the molar volume resulting in an increased density. While the shortening of the intramolecular distances requires drastic density conditions, the intermolecular distances are shortened also at mild pressures, determining stronger interactions leading the system to a high energy state. The system can then explore regions of its potential energy surface that are inaccessible at ambient thermodynamic conditions and possibly can find new local or global energy minima. In the case of molecular crystals this can correspond to transitions to new dense phases [3], amorphisation, ionisation or in more drastic conditions to a complete reorganisation of the chemical bonding structure, leading to the formation of new products.

The effect of pressure on the electronic structure through the molar volume reduction is of particular interest for the aims of this study. A clear rationalisation can be given by the density functional theory, that explains the dependence on density of the repulsive electron-electron potential and the attractive nuclei-electrons potential in the limit case of the electron gas [4]. It is shown that on reducing the molar volume the repulsive term increases more rapidly up to becoming equal to the attractive one, causing deep modifications and also a possible rearrangement of the whole electronic structure that can lead

to transformations and chemical reactions [5, 6]. The aforementioned effects can be well explained taking into account a simple two-electronic state system, in which the higher energy state represents the molecular state in which an electron is excited from the highest occupied molecular orbital (HOMO) to the lowest unoccupied molecular orbital (LUMO) as reported in figure 1.

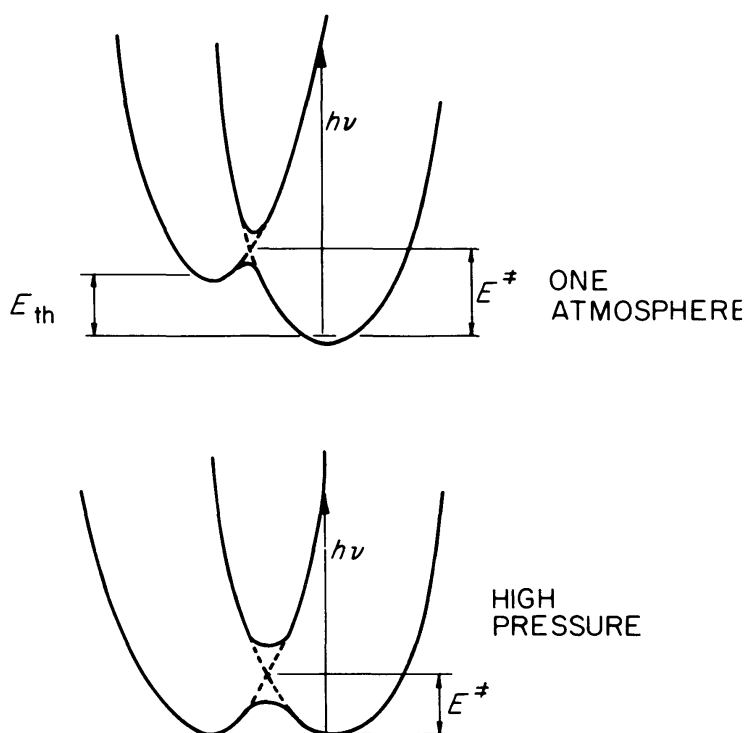


**Figure 1:** Effect of the molar volume reduction on the frontier molecular orbital in the simplest case of a two-state system described by harmonic potentials in a single internal coordinate [5].

The theory predicts a red shift of the vertical electronic transition due to a reduction of the HOMO-LUMO energy gap and a substantial broadening of the electronic absorption band on rising pressure. This results from a complex and different pressure effect on the ground and excited electronic states determining relative vertical and horizontal displacements, corresponding respectively to an energy shift and to a shift in the equilibrium geometry. The energy gap can be reduced in such a way that the LUMO can be thermally populated even at ambient temperature, implying deep modifications on the chemistry of the system. In fact, the electronic and structural changes char-

acterising the excited molecule can trigger, thanks to the high density conditions attainable at high pressure, chemical reactions with the neighbouring molecules. These arguments also suggest how the efficiency of photochemical reactions can be enhanced by pressure.

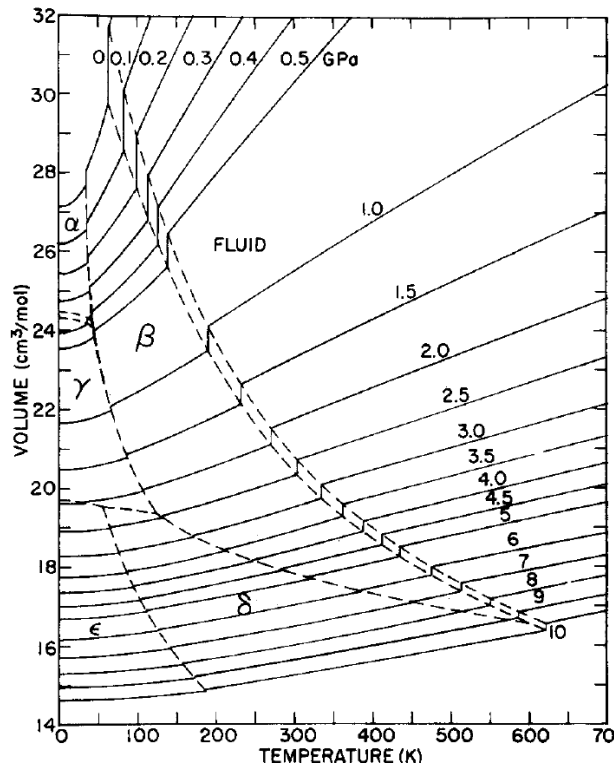


**Figure 2:** Effect of pressure and temperature on the molar volume of a typical molecular system ( $N_2$ ). Notice that the change in the molar volume induced by increasing the pressure from ambient up to about 10 GPa is larger than the one attainable by reducing the temperature down to 0 K along each isobar [7].

It is important to notice that the molar volume reduction needed to observe the described effect can be realised only by applying external pressure, as the one attainable by reducing the temperature is much smaller (figure 2), in other words, acting on pressure allows to explore a much more extended region of the free energy surface than by changing the temperature. From that, the fundamental importance of the study of matter under extreme pressure appears, even considering that the range of pressures encountered in the universe spans over decades, reaching at the centre of a neutron star the impressive value of  $10^{30}$  times the pressure at Earth sea level.

As Earth is concerned, pressure reaches the value of about 360 GPa \* at its centre, then high pressure science becomes fundamental part of geochemistry and geophysics [8] allowing to understand and reproduce the peculiar syntheses occurring at the pressures and temperatures typical of the Earth interiors. Then it becomes more and more relevant in the field of material science as some of the synthesised materials can be recovered at ambient condition and often they have interesting proprieties as extreme hardness. One example over all is represented by the diamond, the thermodynamic unstable allotrope of carbon at room conditions that became the stable form at high pressure and temperature [9].

As the pressure favours denser molecular arrangements, matter at high pressure is generally found in the solid state, often crystalline. The peculiarity of the solid-state reactions is to be controlled by the relatively fixed distances and orientations between potentially reactive centres, involving a reduced molecular mobility, determined by the particular crystal structure. The chemistry in these conditions is ruled by the topochemical principle [10], postulating that reaction in the solid state occurs with a minimum amount of atomic or molecular movement. Moreover the reaction cavity principle [11] should be taken in account for the rationalisation of the reactive processes in the crystal phase. This principle is based on the definition of a cavity formed by the space occupied by the molecules involved in the reaction, whose surface is defined by the force field exerted by the neighbouring molecules. As the deformation of the cavity is energetically unfavourable, being associated to a decrease of attractive forces or an increase in the repulsive ones, only the reaction implying minimum cavity distortions will be favoured. One of the consequences is that for each reaction a critical intermolecular distance should exist under which the reaction can be observed and among the possible reactive paths, only the ones favoured by the crystal arrangement will be effective. Molecular mobility has also a fundamental role the solid state reactivity, be-

---

\*1 GPa (gigaPascal) is equal to  $10^9 Pa$ , where the Pa is defined in the International System as a force equal to 1 Newton applied on a surface of 1 square meter

ing involved in the nucleation and propagation step of the reaction. Molecules have almost fixed positions in the crystal structure and the mobility is limited to the amplitude of the thermal motions. The only way in which favourable configurations in terms of orientations and distances can be instantaneously achieved, able to start a chemical reaction, is represented by the lattice phonons. Moreover, lattice motions are involved also in the propagation of the reaction, in which the perturbation due to the reactive event at the nucleation site is transmitted to the other sites. Due to the collective nature of the phonons, the propagation process is expected to be highly cooperative possibly involving all the molecules of the crystal. Applying an external pressure is an effective way to reduce the intermolecular distances in soft matter and to enhance the amplitude of the cooperative translational and librational motions [12], being a reliable way to induce the solid state reactivity. From the picture, solid state reactions are expected to take place between nearest neighbours, then the molecular structure of the product might be a function of the geometric relation in the crystal lattice of reactant molecules, inducing a certain selectivity of the activated reaction pathways. For several molecular crystals, in addition, the selectivity and the efficiency of the solid state reaction can be enhanced, and the pressure threshold at which the reactivity is induced can be significantly lowered, by combining high pressure to a suitable light irradiation. This is the case of benzene, that is explained in details in section 1.1, whose reaction threshold pressure is lowered by a factor of about two, using a laser wavelength absorbed also by a two photon mechanism, meaning that the initiator species are effective even in catalytic concentration.

Very elegant examples of different selectivity induced by the combination of pressure and light with respect to the only pressure are represented by the ethylene [13, 14] and butadiene case [15]. Ethylene is also an interesting case in which the selectivity of the polymerisation reaction is highly affected by pressure through crystal structure modifications. The higher selectivity in the crystal phase at 3.6 GPa is due to the particular molecular orientation in the crystal, as the polymer growth occurs along only one crystalline axis, charac-

terised by the shorter molecular distances. As the pressure is increased at 5.5 GPa, and due to different compressibility along the different axes, other molecular approaches become competitive resulting in a lesser selectivity and an high branched polymer. Conversely, when the fluid phase is irradiated with suitable light at pressures in the order of 1 GPa, the reaction has total selectivity, as the excitation of the  $\pi^*$  antibonding molecular state causes a change in the molecular geometry able to promote the formation of only ordered linear chains leading to the formation of a denser and high ordered polymer crystal. Instead in the butadiene case the pressure induced reaction leads to the formation of only butadiene dimer (vinylcyclohexene), due to the particular molecular orientation in the crystal. Using the combination of pressure and light, due to the different molecular structure in the electronic excited state, the reaction leads to trans-polybutadiene, a polymer with high technological appeal. However this is not valid in general, as in other cases the photoactivation has no effect on the reactivity of the crystals, because the structural requirements still play a key role in the reaction activation. Indeed, in some of cases in which the only photoactivation is not able to lower the reaction threshold pressure, an interesting reactivity can be triggered using mixtures with molecular species that can be properly activated by optical excitation in pressure and temperature conditions in which the mixture is otherwise stable. The proper mixture should contain a molecular specie that once activated gives very reactive species as radicals, that are the best choice for acting as reactive seeds, being able to induce reactivity also in stable host compounds. This is the case of water mixtures of small hydrocarbons [16] and also more stable compounds like  $N_2$ , the molecule with the more stable bond observed in nature [17], giving rise to a complex reactivity triggered by the aggressive radicals generated by photoexcitation of water itself, also in mild pressure conditions (0.5–1.0 GPa).

The study on the reactivity of molecular systems have been so far limited to the detection of the transformation by frequency resolved optical techniques, but for a clear understanding of most of the aforementioned phenomena a



characterisation of the time-dependent fast dynamics of the system under investigation and how they are influenced by pressure are mandatory. This information can be reliably attained by means of time-resolved ultrafast spectroscopic techniques whose application in conjunction with ultra-high pressure devices unfortunately presents several technical limitations, mainly due to the small quantities of the sample with respect to the thickness of the optical windows in which it is contained. The time resolved techniques can give access to the complete characterisation of the excited electronic states, which is needed for driving the full pressure effect on the molecular electronic structure. For example, the lifetime of an electronic state is directly connected to stability of the state itself, being dependent on phenomena like radiative and non-radiative decays and even on crossings between different electronic states or molecular dissociation or ionisation. Thus its determination as a function of pressure can be analysed in terms of the perturbation induced to such phenomena, having consequences on both optical and chemical properties of the molecular system itself. The time-resolved techniques can also give useful information about transient intermediates following an electronic excitation and possibly involved in the photoinduced reactions. The spectral characterisation of these intermediates, both from electronic and vibrational point of view, is fundamental for the description of the intermediates themselves, by the identification of their fingerprints and their formation mechanism. The characterisation of the reactive path by the identification of the pressure effect on the reaction intermediates and transition states allows in principle an effective rationalisation of the reactivity and of the selectivity among several reactive paths. Indeed, the lifetimes of those species are useful for the understanding of the pressure effect on the efficiency of the reactions in which they are involved. Time-resolved studies are also fundamental in the study of liquids and solutions for the characterisation of the fast dynamics concerning the rotational and vibrational motions and the dynamics of the intermolecular interactions in the ground molecular state. These dynamics are intimately connected to the molecular motions, having huge influence on properties like

transportation and coordination ability, affecting both reaction efficiency and kinetics. This is particularly evident in the case of hydrogen bonded liquids like alcohols or water, in which the hydrogen bond interaction itself and the related dynamics determine the characteristics and the peculiarities of such liquids [18].

## Outline

In this work several new experimental results obtained by different steady state and time resolved spectroscopic techniques unveiling how the pressure can affect the crystal structure, the electronic structure and the fast dynamics of simple model molecules will be shown.

In the first chapter structural studies made by means of Raman and FT-IR spectroscopy on model aromatic and etheroaromatic crystals will be reported. In addition the effect of pressure on the electronic structure of these species evidenced by means of two photon induced fluorescence studies as a function of pressure, and the implication on the reactivity of such systems will be provided.

In the second chapter a study of the reactivity induced by the combination of pressure and laser irradiation in simple alcohols will be presented, with the aim of better understanding the effect of high density on the electronic structure of these species and on the mechanism of the photoinduced reactions and how pressure influences the photodissociation.

In the third chapter the application of ultrafast time-resolved transient infrared pump-probe spectroscopy, in conjunction with the high pressure devices, will be reported for the first time for describing the dynamical properties of liquid water and how they are influenced by the high density conditions attained at high pressure.

In the fourth chapter a detailed description of the techniques and the instrumentation used in the work will be given.

# Two photon induced fluorescence and reactivity of model aromatics

In this chapter the relationship between the modifications induced by the application of an external pressure on crystalline simple molecular systems, and their electronic structure, and the implication on the reactivity, will be discussed. To this purpose an ideal class of compounds is represented by the aromatics, characterised by high compressibility [1, 2] that can result in deep modifications of both structural and optical properties as a function of pressure.

## 1.1 Benzene

The simplest aromatic compound is benzene, which represents a fundamental model for the whole class and whose reactivity and electronic properties under pressure have been well characterised [19, 20]. As benzene is compressed up to the reaction threshold pressure, an extended solid-state chemical reaction is observed which produces an amorphous hydrogenated carbon, generally identified as a-C:H [21–23]. The high hydrogen content of the amorphous carbon prepared in this way makes this reaction appealing from a technological point of view. Indeed, the product presents enhanced mechanical properties with respect to that prepared via chemical vapour deposition due to the

higher content of  $sp^3$  C, while retaining all the properties typical of the material as high wear resistance, low friction coefficient, low dielectric constant and high breakdown strength [22]. Hence, the interest in understanding and the developing this kind of reactions, and thus the need to explain the microscopic mechanisms that lead to different paths and products as pressure and temperature are modified.

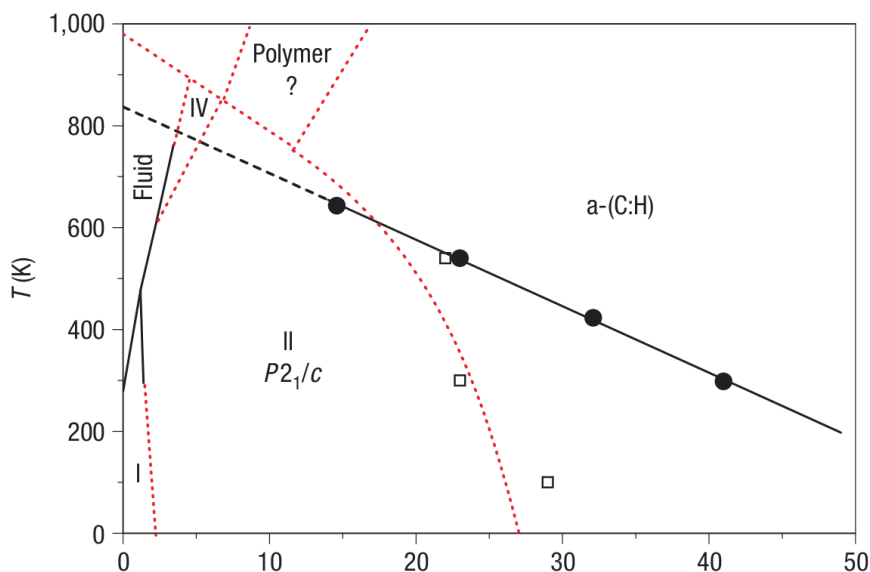


**Figure 1.1:** Chemical-stability boundaries of clean phase II of benzene (black dots) reported onto the phase diagram [19, 22].

It has been shown that as a pure phase II crystal of benzene is compressed at different temperatures, a reaction always occurs when the minimum instantaneous C $\cdots$ C distance between two nearest neighbours, taking in account the thermal motions, approaches a critical value of 2.6 Å [19]. The chemical stability boundaries are reported in figure 1.1. The mechanisms of the reaction initiation are well explained by ab initio molecular dynamics simulation showing that the reactive events are initiated by the formation of a  $\sigma$  bond between two molecules in a slipped parallel configuration. Once the first bond is formed, a reactive zwitterionic species is generated from which the reaction propagates to the whole crystal. The lattice phonons, have a key role in both tuning the instantaneous intermolecular distances favouring the overlap of the  $\pi$  electronic densities that lead to the formation, of the reaction seeds,

and in propagating the reaction to the whole crystal allowing the formation of the amorphous C:H system [22]. This represents a clear evidence of the intimate relationship between the crystal structure and the reactivity in molecular crystals.

The reaction pressure threshold can be significantly reduced by a suitable laser irradiation of the crystal, showing an active role of the electronic excited states in the formation of the reaction seeds [24]. It is shown that when the CW laser line employed for the irradiation is absorbed even by a two-photon mechanism exciting some molecules, the reaction seeds are formed also at a pressure of about half the value required for spontaneous reaction. Both methods of initiation (high pressure and high pressure plus photoactivation) lead to the same product and have similar reaction features, indicating that a similar mechanism occurs in both cases. The interpretation of this phenomenon, fundamental for the correct understanding of the microscopic mechanisms of the pressure induced reactivity, was given by a two-photon induced fluorescence study of the benzene crystal using pulsed sources in the picosecond timescale allowing the characterisation of the  $S_0 \rightarrow S_1$  transition as a function of pressure [20]. By the analysis of the intensity distributions of the Frank-Condon progression as a function of pressure, a relative horizontal displacement between  $S_0$  and  $S_1$  is found, consisting in an increased similarity of the two potential surfaces driven by the greater compressibility of the molecule in the  $S_1$  excited state leading to an increased superposition of the two minima. In addition, the formation of excimers\* was identified by the observation of an unstructured fluorescence emission laying about  $5000\text{ cm}^{-1}$  on the red side of the monomer emission [25–29]. This emission band intensifies on rising pressure, meaning that the excimer itself is stabilised by pressure, becoming the 9/10 of the total emission intensity above 11 GPa as reported in figure 1.2. The emission features are perfectly reversible on decompression, meaning that there is a structural origin for its formation. Indeed, the

---

\* an excimer, originally short for excited dimer, is a supramolecular structure formed by a molecule in the excited electronic state and a molecule in the ground state.

molecules along  $a$  and  $b$  axes in benzene phase II structure are arranged in a slipped-parallel configuration, a geometry that is supposed to allow the formation of excimers.

This evidence can explain the reaction mechanism at the microscopic level. In particular it appears that the reaction initiation through the  $S_1(^1B_{2u})$  state to which the system decays prior to any reactive event or emission, is not led by a reduction of the intermolecular C $\cdots$ C distance, as the molecular geometry of benzene is only slightly altered in the excited state, especially compared to the displacement due to thermal motions (lattice phonons) in the same  $P$ - $T$  conditions. Instead, it is shown that the charge-transfer processes that gives rise to the excimer are allowed by the phase II benzene structure and become dominant at high pressure. These structural excimers are then responsible for

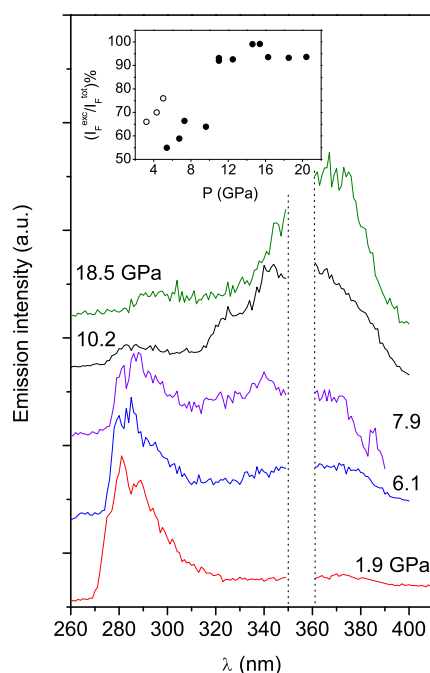


**Figure 1.2:** Pressure evolution of the two photon induced fluorescence in benzene crystal [20]. The high frequency band is the fluorescence band attributed to the monomer, while the low frequency one belongs to the excimeric specie. In the inset the pressure evolution of the ration of the integrated area of the two bands is reported in compression (full dots) and decompression (empty dots), showing a good reversibility but a little hysteresis.

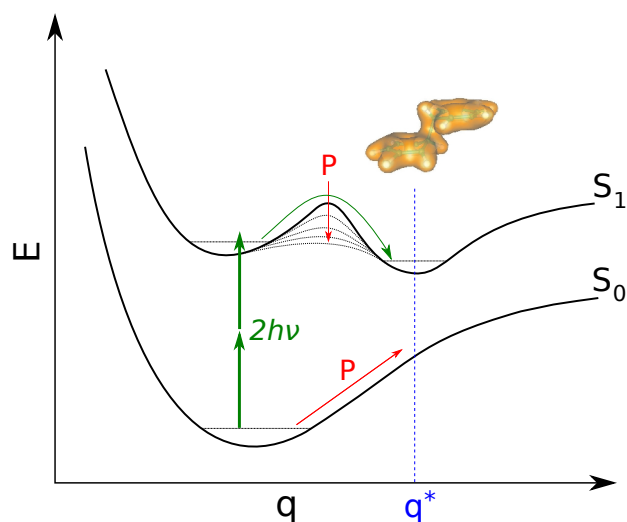


**Figure 1.3:** Sketch of the pressure effect of electronic structure of benzene explaining the pressure induced reactivity and the photoinduced high pressure reactivity

seeding the reaction, suggesting that the dimerisation of benzene is the first step also of the photo-assisted amorphisation reaction. As shown in figure 1.3, the effect of pressure in the pressure induced reaction is to lower the energy barrier for the formation of the reaction seeds by bringing the molecules close up the critical distance to the dimer formation. The same reaction seeds can be formed by electronic excitation through the excited states at lower pressure.

From this introductory picture appears evident how much the knowledge of the pressure evolution of both the crystal and the electronic structures are important for a clear understanding of the high pressure reactivity for this kind of molecules. In the next sections the results obtained for other model aromatic and etheroaromatic systems will be illustrated, with the aim of understanding the effect of pressure on the electronic states and their implications in the reactivity of molecular crystals.

## 1.2 Pyridine

Pyridine is the prototype of etheroaromatics and its brute formula is  $C_5H_5N$ , presenting the same six-ring structure of benzene with one methine group ( $=CH-$ ) replaced by a nitrogen atom. Due to the presence of the nitrogen, pyridine shows a neat dipole moment as the  $\pi$ -electron density is not equally distributed over the ring and a resulting weaker aromatic stabilisation. Due to the different valence of nitrogen with respect to carbon, pyridine lacks of one hydrogen atom with respect to benzene, that is replaced by an electron lone pair localised in a  $sp^2$  hybrid orbital of the nitrogen atom not shared on the ring and responsible for the basicity and the ability to form H-bonds of the molecule [30].

Pyridine is a good subject of study within the framework of the reactivity in molecular crystal, for its rich high pressure polymorphism [31]. The study of the high pressure stability of the pyridine crystal phases is motivated by the purpose of a better understanding of the connection between the crystal structure and the reactivity. In analogy to benzene a chemical transformation to an amorphous material is expected [31,32], making the high pressure reaction appealing for the high pressure synthesis of nitrogen rich hydrogenated carbons, which may add the property of electronic conductivity to the others typical of the material.

### 1.2.1 High pressure polymorphism

Two different crystalline phases of pyridine are known [33]. Pyridine is a colourless malodorous liquid at room conditions that crystallises upon increasing pressure at about 0.55 GPa [34]. This phase, known as phase I, is orthorhombic  $Pna2_1$  ( $C_{2v}^9$ ) with four molecules in the asymmetric unit cell. This is the same crystal attainable on cooling pyridine down to 231 K at ambient pressure [35,36]. The second crystalline phase (phase II) is attainable at ambient pressure and low temperature only for deuterated pyridine ( $d_5$ -pyridine) or in pentane solution of  $h_5$ -pyridine, but never in neat  $h_5$ -pyridine which is



stable in phase I down to 5 K [35]. Indeed, it is known that neat pyridine crystallises in phase II (orthorhombic  $P2_12_12_1$ ,  $D_2^4$ ,  $z=4$ ) when compressed above 1 GPa [35].

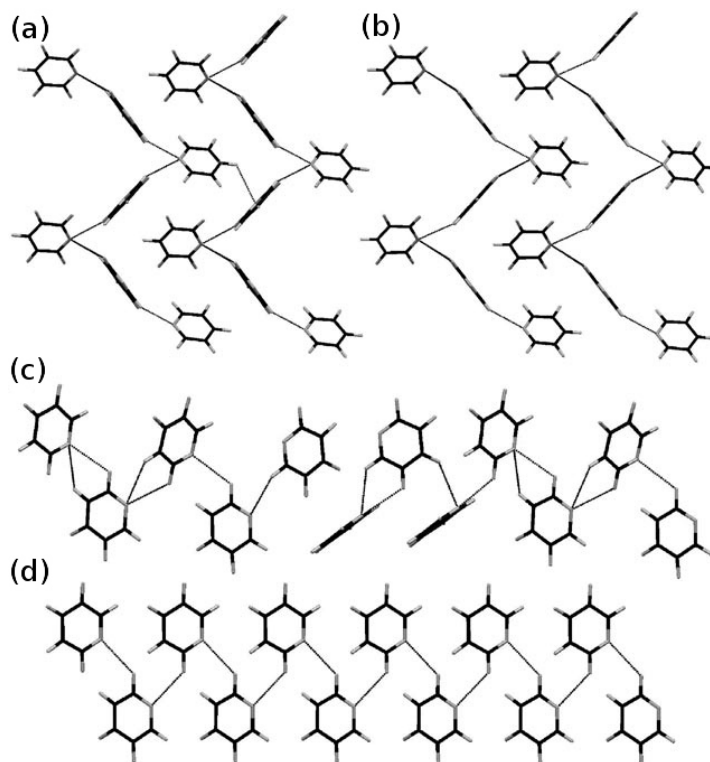


**Figure 1.4:** Molecular arrangement in the two crystalline phases of pyridine. As phase I presents layers parallel to the (100) plane (a), similar layer are present in phase II parallel to the (110) plane (b). From the staking of the molecules perpendicular to the aforementioned planes we can notice that the  $\text{CH}\cdots\pi$  interaction of phase I (c) are converted in  $\text{CH}\cdots\text{N}$  contacts in phase II (d) [35]

The molecular arrangements in the two phases are reported in figure 1.4. Both polymorphs contain layers lying parallel to the (100) planes in the phase I, and to the (110) planes in phase II. The most prominent molecular interactions in both phases are  $\text{CH}\cdots\text{N}$  and  $\text{CH}\cdots\pi$  interactions, shown to be very similar in terms of bond energy ( $8\text{--}10\text{ kJ mol}^{-1}$ ) [37]. As it is clear from figure 1.4, the change in molecular orientation occurring as a result of the transition from phase I to phase II replaces some  $\text{CH}\cdots\pi$  by  $\text{CH}\cdots\text{N}$  contacts. Despite the similarities between the two phases and the almost negligible volume change at the transition, the transition itself is reported to be high destructive, not al-

lowing the formation of a single phase II crystal [35], as the inversion of two molecular dipoles and the rotation by  $90^\circ$  of other two molecules are required [38].

In our work we performed an extensive study of the high pressure condensed phases of pyridine by Raman and infrared spectroscopy, evidencing three different polymorphs and establishing the pressure condition in which they exist as stable or metastable forms [32].

When compressing liquid pyridine at room temperature we observed a phase transition to a crystal phase generally between 1.2 - 1.3 GPa, although higher pressure values up to 1.8 GPa were observed. The crystallisation was detected by visual observation of the formation of large crystallites, and by the abrupt changes appearing in the Raman spectrum (figure 1.5). The Raman spectrum in the low frequency region ( $25\text{-}200\text{ cm}^{-1}$ ), almost unstructured be-

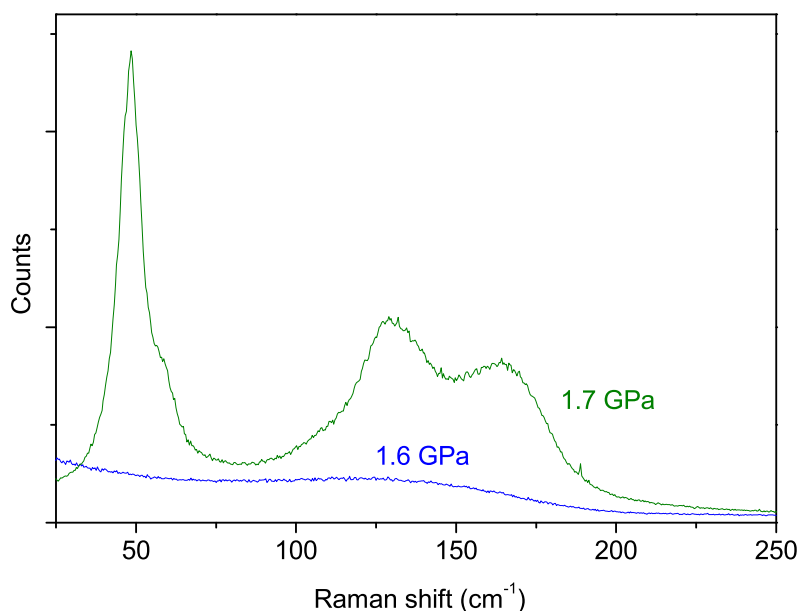


**Figure 1.5:** Raman spectra in the lattice phonons region recorded in a compression experiment of liquid pyridine showing the spectral changes occurring on crystallisation from the supercompressed liquid at 1.6 GPa (blue trace). The phonon pattern appearing at 1.7 GPa (green trace) is typical of phase II [33]

fore the transition, showed the typical phonon pattern of the crystalline phase II [33]. This observation together with the discrepancy in the pressure transition value reported for the equilibrium crystallisation of a single phase I crystal to be about 0.55 GPa [34], suggest that liquid pyridine can be easily supercompressed above the melting pressure, and in a straight compression ramp the crystallisation occurs directly in phase II.

We verified this hypothesis by a careful analysis of the low frequency Raman spectra as a function of pressure in compression experiments up to the observation of the crystallisation. The Raman susceptibility, calculated according the formula 1.1, is reported in figure 1.6.

$$\chi''(\omega) = \frac{I(\omega)}{n(\omega) + 1} \quad (1.1)$$

where  $n(\omega)$  is the thermal population factor.

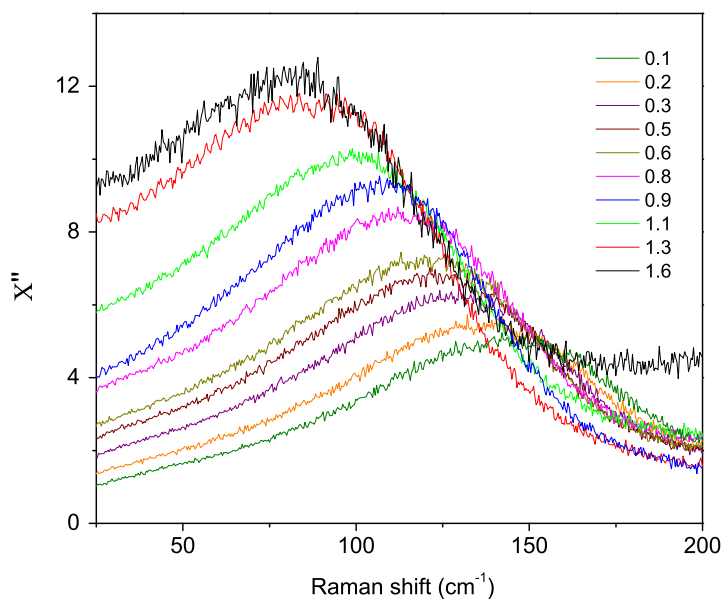


**Figure 1.6:** Raman susceptibility recorded upon compressing liquid pyridine calculated according to the formula 1.1. Pressure values are in GPa.

The low frequency Raman spectra of liquids in our experimentally accessible range (Raman shift  $> 20 \text{ cm}^{-1}$ ) is essentially composed by the quasielastic

scattering and a broad band due to molecular librations typically at about  $100\text{ cm}^{-1}$  of Raman shift [39]. On rising the pressure up to 1.6 GPa a decrease in the intensity of the quasielastic band which is related to the relaxation dynamics [40], and a neat blue shift in the librational peak are observed, due to an increased density and viscosity in the liquid. Then, up to 1.6 GPa a clear lack of crystallisation is observed, despite the pressure values are much higher than the room temperature melting pressure of 0.55 GPa.

Once phase II is decompressed under about 1 GPa, the sample appearance abruptly changes, consisting in a complete fragmentation of the crystal domains, associated to a splitting of infrared absorption bands [32]. Both the transition pressure and the destructive character of the transformation agree with the observation reported for the I–II phase transition [34]. The Raman spectra recorded before and after the change observed in decompression (reported in fig 1.7) confirm that a phase transition occurs, as the spectra in the region of the lattice phonons become from typical of pyridine phase II to typical of phase I [33].

Some authors [31,41], report several other high pressure transitions to claimed new and not characterised crystal phases of pyridine, principally based on spectral features of questionable interpretation. Conversely, in all our experiments, no signature of any other phase than phase II is observed up to the reaction threshold pressure. In figure 1.8 the pressure evolution of the lattice phonon peaks are reported as a function of pressure, together with some Raman spectra recorded at same pressure in the same sample for different crystallite orientations, taking advantages of our higher Raman spatial resolution of about  $2\text{ }\mu\text{m}$ . Despite these spectra appear quite different from one another, the decomposition into Voigt profiles through a fitting procedure, shows that these spectra are composed by the same bands with different relative intensity, confirming that they originate from crystallites of the same phase but different orientations. No discontinuity is observed in the pressure evolution of the lattice phonon peaks frequency for the 20 identified out of 21 expected phonon bands for the phase II, in both compression and decompression ex-

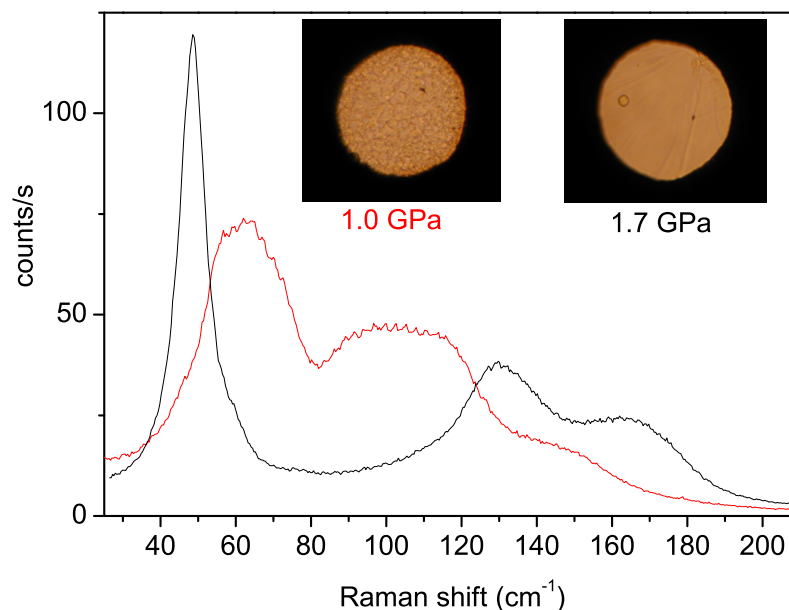


**Figure 1.7:** Raman spectra recorded before and after the abrupt change observed decompressing the crystalline sample under about 1.0 GPa as shown in the photographs, confirming that a transition from the phase II (black line, corresponding to the 1.7 GPa photo) to phase I (red line, corresponding to the 1.0 GPa photo) occurred.

periments, ruling out any other phase transition of pyridine up to the spontaneous reaction threshold pressure.

As a high quality phase I crystal is compressed at room temperature no clear phase transitions were observed up to 9.4 GPa, although the I→II transition pressure is 1.2 GPa, showing a high metastability of the phase I (figure 1.9). Indeed, excluding the new peak appearing at about 1340 cm<sup>-1</sup> and gaining intensity on further compression and a loss of intensity of the 1350 cm<sup>-1</sup> phase I band, no spectral changes indicating a phase transition are observed and the spectral features of phase II are never obtained in compression. A thermal annealing of the sample at 460 K and 9.4 GPa causes detectable changes in both sample appearance and IR spectra. The IR spectrum resembles that of the phase II at the same pressure, although the relative intens-

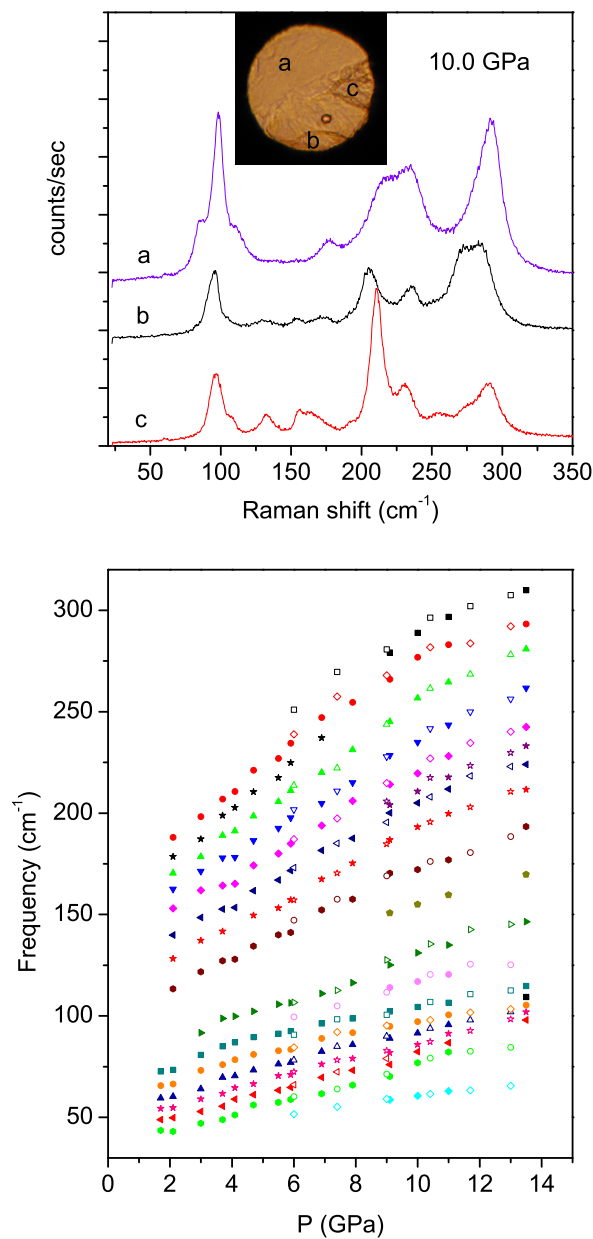


**Figure 1.8:** Upper panel: Raman spectra of the lattice phonon region measured in differently oriented crystallites in pyridine phase II at 10.0 GPa. Lower panel: Pressure evolution of the lattice phonon peak frequencies deriving from a fitting procedure using Voigt profiles. 20 out of 21 phonon bands expected for phase II were identified and no signature of any phase transition in this range of pressure was observed in both compression (full symbols) and decompression cycle (empty symbols).

ities of some Davydov components are different, meaning that the thermal annealing favoured the conversion to phase II, but remnants of phase I still remain.

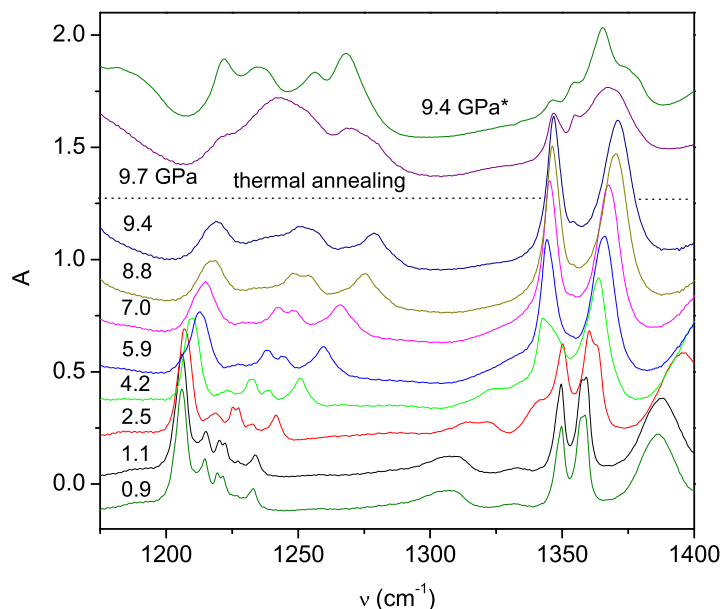


**Figure 1.9:** Pressure evolution of IR spectra measured on compressing a clean pyridine phase I crystal in the pressure range of stability of phase II. No clear transition is detected, showing a high metastability up to 9.4 GPa of the phase I and a sluggish I→II transition. A better transformation (but not complete) to phase II is observed after a thermal annealing. The upper trace is an IR spectra of a clean phase II reported here for better comparison.

In some compression experiments liquid pyridine apparently did not crystallise remaining perfectly homogeneous, transparent and apparently stable for further compression. Raman spectra measured in those samples do not show any signs of lattice phonons and also the IR spectra resemble that of the liquid, leading to conclude that this form is a metastable amorphous solid already observed by other authors [33, 42]. Compressing the amorphous form up to 20 GPa no spectral change is observed but a blue shift of all the bands [32]. A thermal annealing performed up to 490 K is not able to promote the transition to the stable phase II till the pressure is lowered down to few GPa,

remarking the key role of pressure in determining the metastability. Decompressing the amorphous under 1 GPa, brings the formation of phase I. Again it is shown the sluggish nature of the phase transitions in pyridine and the high metastability of the pyridine forms.

### 1.2.2 High pressure and photoinduced reactivity

When pyridine is compressed above 22 GPa an irreversible chemical transformation occurs consisting in the destruction of the aromatic ring and the formation of an extended amorphous material [31]. The reaction is detectable by the appearance in the IR spectra of the C-H stretching bands involving  $sp^3$  saturated carbons, as already reported for benzene (see section 1.1). In our compression experiments we detected the onset of the chemical reaction for a clean and annealed pyridine phase II crystal at about 18 GPa, when a broad band centred at about  $1300\text{ cm}^{-1}$  and a narrower one above  $3000\text{ cm}^{-1}$  appear in the IR spectra (figure 1.10), slightly intensifying on further compression. An intensification of the product bands is observed in decompression, especially in the last steps. The reaction threshold found for not annealed pyridine, presenting much more crystal defects, is similar (17 GPa), but the compression-decompression cycle leads to the formation of larger amount of product. Indeed, the reaction is never quantitative as a lot of unreacted pyridine is always recovered at ambient pressure and the more defected crystals give rise to the larger amounts of recovered product. On compressing the amorphous pyridine no sign of reactivity was observed for pressure up to 25 GPa and the original spectrum was recovered at ambient pressure, showing also in this case like in benzene, the remarkable role of the cooperative dynamics typical of ordered crystals (lattice phonon) in triggering and driving the solid state reactivity.

Similar to the case of benzene an irradiation with a suitable laser line is able to reduce the reaction threshold pressure by a factor of about 3 suggesting a similar reaction activation. In particular using few hundreds mW of a wavelength equal or shorter than 457 nm, laying into the two-photon absorp-



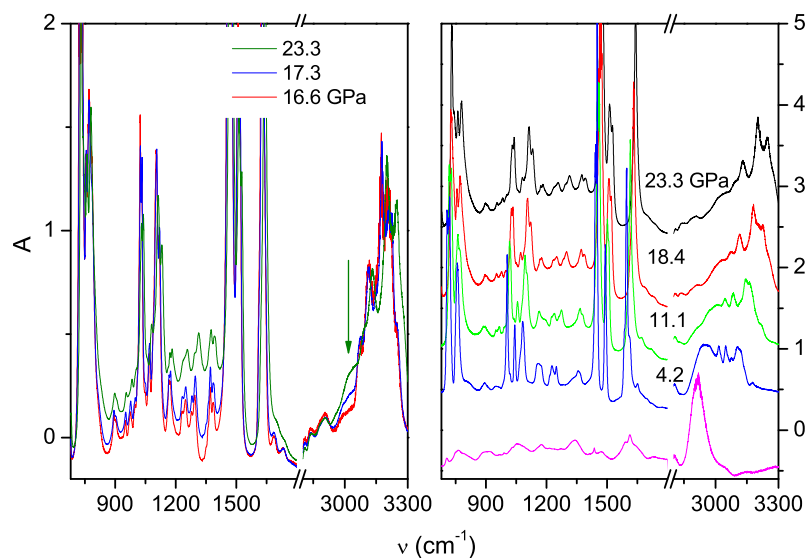


**Figure 1.10:** a) Infrared spectra of pyridine phase II at the onset of the chemical reaction detected by the formation of the novel bands 1300 and above  $3000\text{ cm}^{-1}$ . b) Infrared spectra recorded in decompression after the reaction is seeded. The last is the spectrum of open cell in which the unreacted pyridine was removed.

tion edge of the  $S_4$  ( $A_1$ ,  $\pi\pi^*$ ) electronic excited state (see section 1.2.3), the reaction is triggered also at 6.5 GPa. No effect is observed for longer excitation wavelength. Also for the photoinduced reaction, once triggered, it does not propagate on decompression. A comparison of the low pressure recovered product for the photoinduced and the pressure induced products obtained for thermally annealed and not annealed phase II crystals are reported in figure 1.11. Despite the different intensities corresponding to different product amounts, the observed spectral features are almost the same suggesting an identical reaction product and a same reaction mechanism for the photoinduced and the spontaneous high pressure reactions.

Although the pyridine high pressure reaction is similar to that observed in benzene it has some fundamental differences. First the reaction does not extend to the whole crystal on releasing pressure and second, more defected crystals led to larger amounts of product. This observation could indicate a

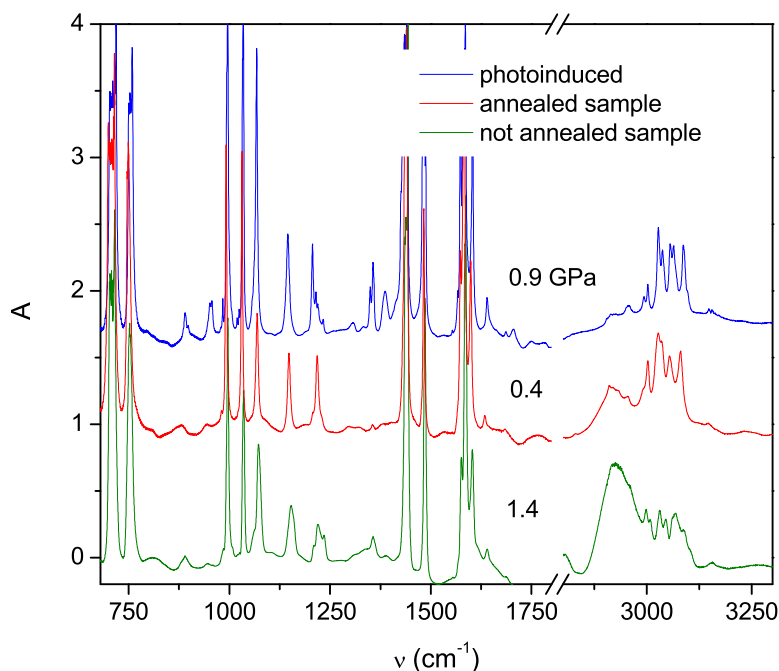


**Figure 1.11:** Infrared spectra of spontaneous and photoinduced high pressure reaction of pyridine phase II

defect-driven nature of the high pressure reaction in pyridine. Indeed in contrast to benzene, the molecular arrangement in pyridine phase II (figure 1.12), which we demonstrate to be the stable phase up to the reaction threshold, does not allow the formation of structural excimers able to trigger the reaction. As already discussed, the prerequisite to the formation of dimers able to trigger the reactivity is a slipped-parallel configuration, mandatory for an efficient overlap of the  $\pi$  densities of neighbour molecules. The only nearest equivalent molecules in this configuration at sufficient short distances lie along the  $a$  axis which  $\text{C}\cdots\text{N}$  and  $\text{C}\cdots\text{C}$  contacts are slightly larger than 3.5 Å at 1.1 GPa [43]. However the approach of these molecules through zone boundary acoustic modes is hindered by a complex three-dimensional network of hydrogen bonds as each molecule is connected to four pyridine molecules by hydrogen bond interactions, two involving the nitrogen atom and two the hydrogen atoms bonded to the carbon in  $\alpha$  position to the nitrogen ( $\text{N}\cdots\text{H}$  dis-

tances are respectively  $\sim 2.6$  and  $\sim 2.8$  Å at 1.2 GPa [43]). By these consideration we can conclude that the reaction seeds are generated only at crystal defects and once the reaction is triggered it can't extend to the whole crystal because the peculiar H-bond structure severely hinders an effective contact through acoustics modes.

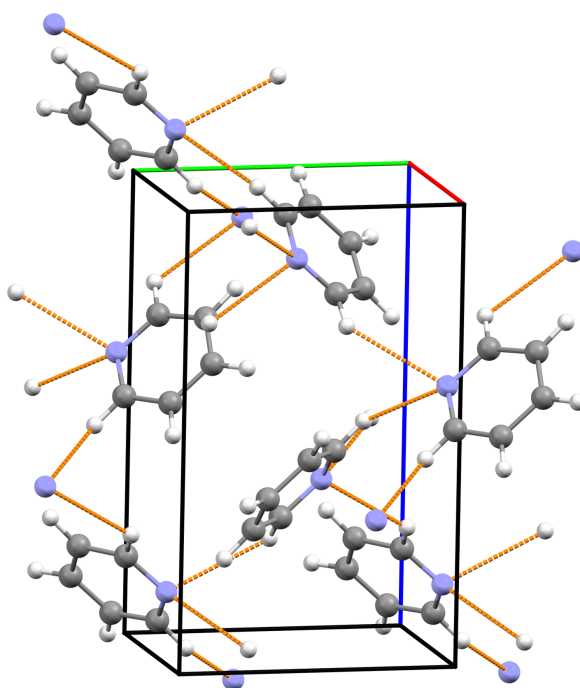


**Figure 1.12:** Molecular arrangement in pyridine phase II at 1.1 GPa (data elaboration from [43]). The  $a$  axis is reported in red, the  $b$  in green and the  $c$  in blue.

### 1.2.3 Electronic properties

As discussed in the section 1.2.2, the threshold pressure for the reaction in pyridine crystal is strongly lowered by a suitable photoactivation. From the latter observation and a comparison with the benzene case, the importance of an experimental characterisation of the low lying electronic states evolution as a function of pressure appears mandatory for a correct understanding of the

mechanisms regarding the photoinduced reaction.

In the ambient pressure absorption spectra of pyridine, four excited singlet electronic states have been identified for wavelength longer than 200 nm (see the scheme in figure 1.13) [44, 45]. The first excited electronic state  $S_1$  has  $n\pi^*$  character<sup>†</sup>, belongs to  ${}^1B_1$  symmetry in  $C_{2v}$  point group, has electronic origin at 287.1 nm and maximum around 260 nm.  $S_2$  ( ${}^1B_2$ ) and  $S_4$  ( ${}^1A_1$ ) have both  $\pi\pi^*$  character and maxima at about 250 and 200 nm respectively.  $S_3$  ( ${}^1A_2$ ) is another  $n\pi^*$  which maximum lays at 230 nm. All these states are both one and two-photon active except  $S_3$  ( ${}^1A_2$ ) that is only two-photon active.

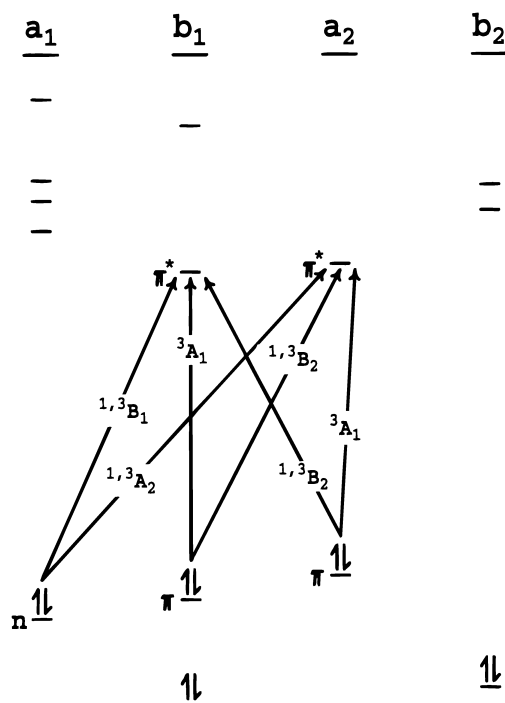


**Figure 1.13:** Hartree-Fock molecular orbitals and firsts single electron transitions and relative symmetry for the pyridine molecule [45].

In contrast to benzene, pyridine is a strongly non-fluorescent molecule, and a weak fluorescence is observed only in the low pressure gas phase with a quantum yield  $\Phi_F$  ranging from  $10^{-4}$  to  $10^{-6}$  at 130 Pa [46]. This is strictly correlated to the  $n\pi^*$  character of the lowest electronic state [47, 48] as  $n\pi^*$

<sup>†</sup> with  $n\pi^*$  and  $\pi\pi^*$  state are identified the molecular electronic excited state generated by a single electron excitation respectively from a non-bonding  $n$  and a bonding  $\pi$  type state to a non-bonding  $\pi^*$  state (named after the representations in the  $D_{\infty h}$  point group)

transitions are characterised by a cross section of about two orders of magnitude lower than  $\pi\pi^*$ , due to the smaller overlap between  $n$  and  $\pi^*$  molecular orbitals. In addition the radiative lifetime of  $n\pi^*$  states is two order of magnitude longer than that of  $\pi\pi^*$  states, allowing the non-radiative processes to be dominant of the radiative ones. Also the inter-system crossing is 2-3 orders of magnitude more efficient when it involves a  $^1n\pi^*$  state and a lower energy  $^3\pi\pi^*$  state with respect to molecules lacking of the  $^1n\pi^*$  state [49]. These pieces of evidence justify the lack of fluorescence of pyridine which has never been observed before in condensed phase.

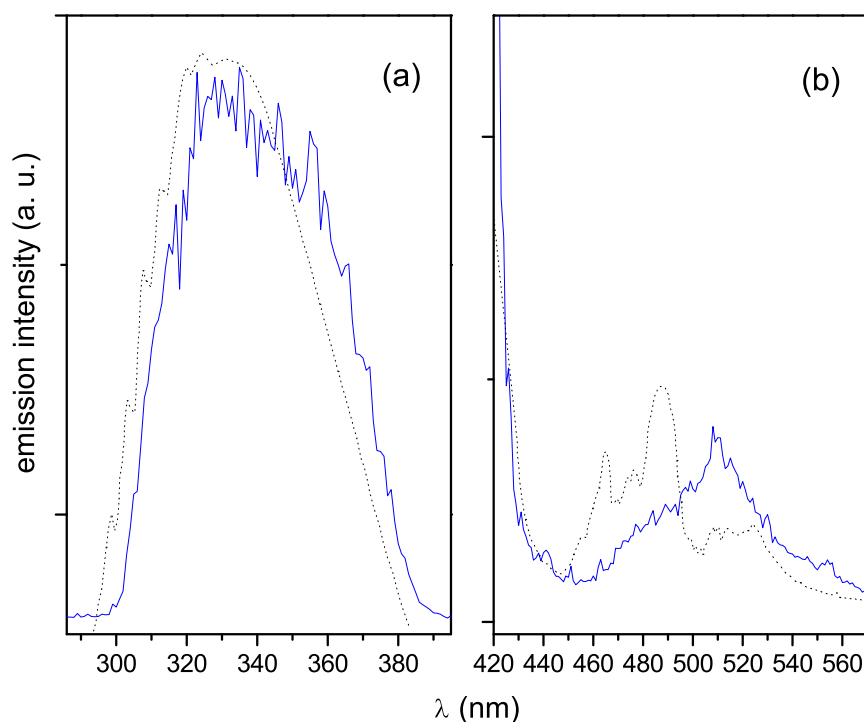


**Figure 1.14:** a) Fluorescence spectrum of liquid pyridine (blue trace) measured in a 10 mm thick quartz cuvette using an high energetic pulsed source (30  $\mu$ J/pulse, 30 ps of pulse duration, 485 nm) superimposed to that of the gas phase (P=2600 Pa, excitation at 285 nm) [46]. b) Two photon excitation profile of same sample (blue trace) compared to the two photon absorption spectrum measured by thermal lens technique [44].

For the first time we were able to observe the ambient pressure two photon induced fluorescence of liquid pyridine in a 10 mm quartz cuvette and to measure the relative excitation profile [50]. The fluorescence spectrum and the excitation profile of liquid pyridine at room conditions are reported in figure 1.14. The fluorescence spectrum is in very good agreement with that of the gas phase, the only one previously reported [46], being only slightly red-shifted. No dependence from the excitation wavelength in the range 420-540 nm was observed leading to exclude any other phenomenon but relaxed fluorescence. The two photon excitation profile is in good agreement with the two photon absorption spectra measured by thermal lens technique [44] regarding the excitation frequencies, but the relative intensities of  $S_2$  ( $^1B_2$ , TP:500 – 540 nm) and  $S_3$  ( $^1A_2$ , TP:460 – 500 nm) are inverted probably because of the intrinsic difference between the two techniques. The first transition to  $S_1$  is not observed in both experiments as expected by the extremely low absorption cross section.

No fluorescence can be observed from liquid pyridine in the diamond anvil cell for the strongly different conditions of the experiment, namely a very thin sample ( $\sim 50 - 100 \mu\text{m}$ ) and a very different energy of excitation that we can employ to avoid diamond damage (up to a maximum of few  $\mu\text{m}/\text{pulse}$  compared to the over 30  $\mu\text{m}/\text{pulse}$  necessary to observe fluorescence in the quartz cuvette).

When solid phase II of pyridine was compressed up to  $\sim 3$  GPa, a weak fluorescence signal centred at about 330 nm appeared upon excitation in the 420 – 440 nm range. The fluorescence spectra and the relative excitation profile are reported in figure 1.15. The fluorescence spectrum is slightly blue-shifted with respect to that measured in liquid pyridine, resembling closer the gas phase spectrum [46]. The excitation profile is quite different, being the bands assigned to the transition to  $S_2$  ( $^1B_2$ , TP:500 – 540 nm) and  $S_3$  ( $^1A_2$ , TP:460 – 500 nm) barely detectable and the edge of the strongest absorption to  $S_4$  ( $^1A_1$ ) quite red shifted.

On rising the pressure up to about 8 GPa, the fluorescence emission in-

tensity further increase, whereas above this pressure it decreases again remaining still detectable up to about 16 GPa (figure 1.16). By a fitting procedure using the minimum number of Voigt profiles four peaks were identified (figure 1.17a). The first three high frequency bands have the same pressure behaviour, increasing in intensity up to about 6 GPa then decreasing for higher pressure, and the sum of their integrated areas is reported in figure 1.17c. The intensity of the lowest frequency band has a different pressure dependence with maximum at  $\sim 12$  GPa (figure 1.17b). This band is red-shifted from the highest frequency band of about  $5000\text{ cm}^{-1}$ , typical for an aromatic excimer formed in the crystal [20, 25–29]. To understand the nature of the excimer, investigation was performed on phase II crystals of different qualities, mixed

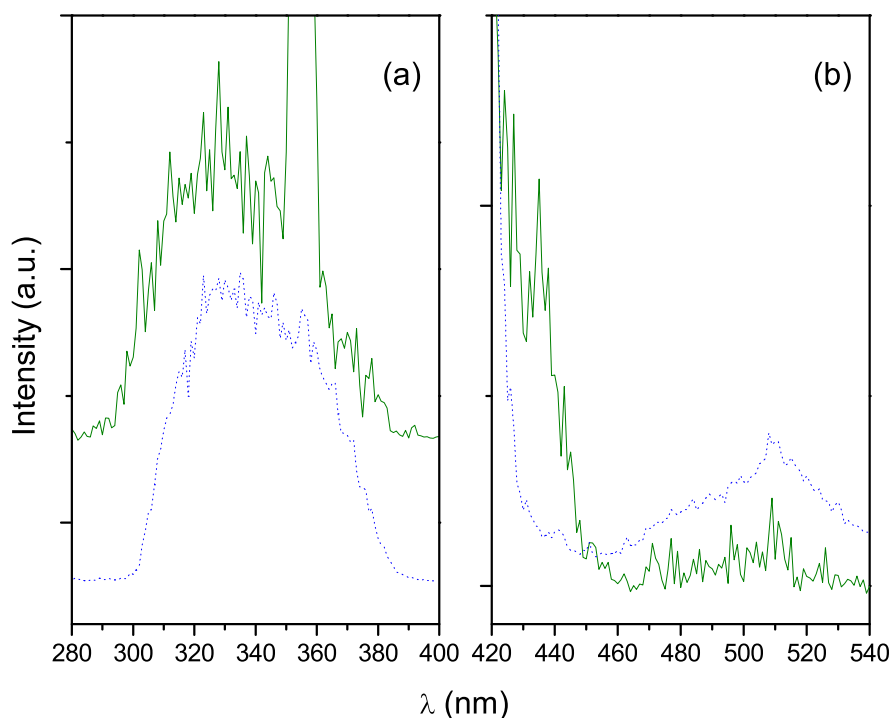


**Figure 1.15:** Two photon induced fluorescence spectra (a) and TP excitation profile (b) of solid phase II pyridine measured in the diamond anvil cell at 3.1 GPa (green traces) compared to that ones measured in liquid pyridine in the quartz cuvette (dashed lines).

high defected I+II phases and amorphous forms of pyridine. The relative intensities of the excimer band with respect to the overall fluorescence intensity is reported in figure 1.18b.

For all the samples, the pressure evolution of the band frequencies are almost identical and perfectly reversible in decompression with the exception of a little hysteresis as reported in figure 1.18a. Conversely, the relative intens-

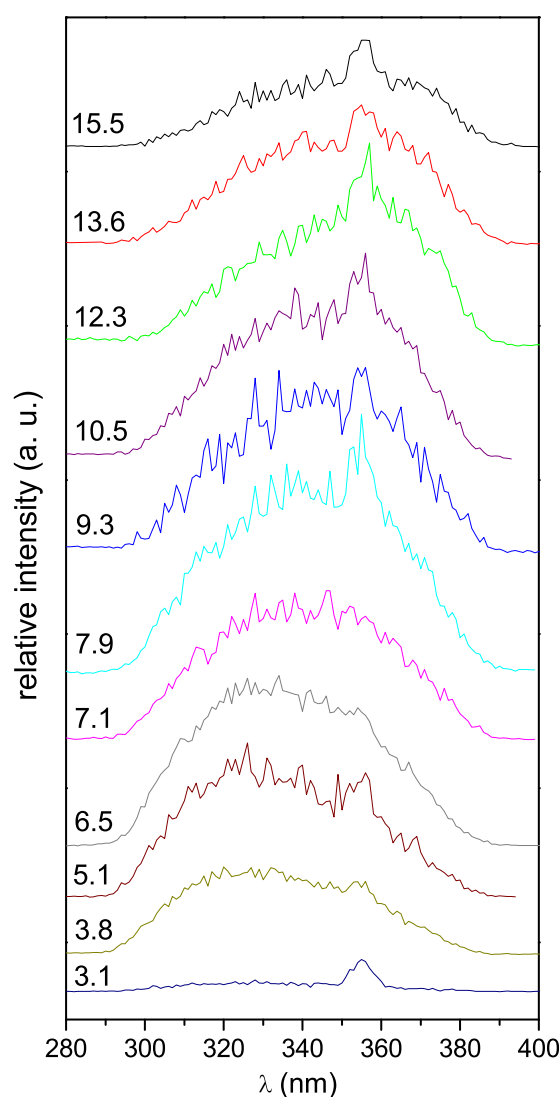


**Figure 1.16:** Two photon induced fluorescence spectra of solid phase II pyridine measured in the diamond anvil cell as a function of pressure. Pressure is reported in GPa.



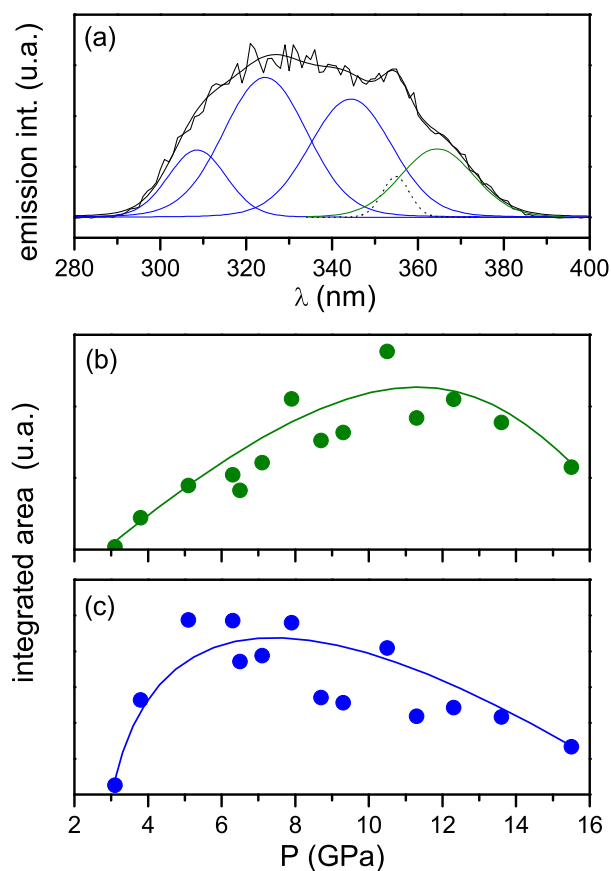


**Figure 1.17:** a) Example of decomposition of the fluorescence emission by use of the minimum number of Voigt profiles for a not annealed pyridine phase II crystal at 6.5 GPa. b) Integrated area as a function of pressure of the lowest frequency band. c) Sum of the integrated area of the three highest frequency bands reported as a function of pressure.

ity of the excimer band depends on the amount of crystal defect being larger for more stressed samples and not reversible in compression-decompression cycles, as more intensity is recovered at low pressure in the decompression step. The observation can be rationalised on the same basis previously invoked to discuss the pressure induced reactivity (section 1.2.2), leading to conclude that this specie is not a structural excimer as the arrangement in the crystal structures of pyridine does not allow the correct molecular approach. Then excimers are formed only at crystal defect and as a further proof, the amorphous form, in which molecules are not constrained by the crystalline

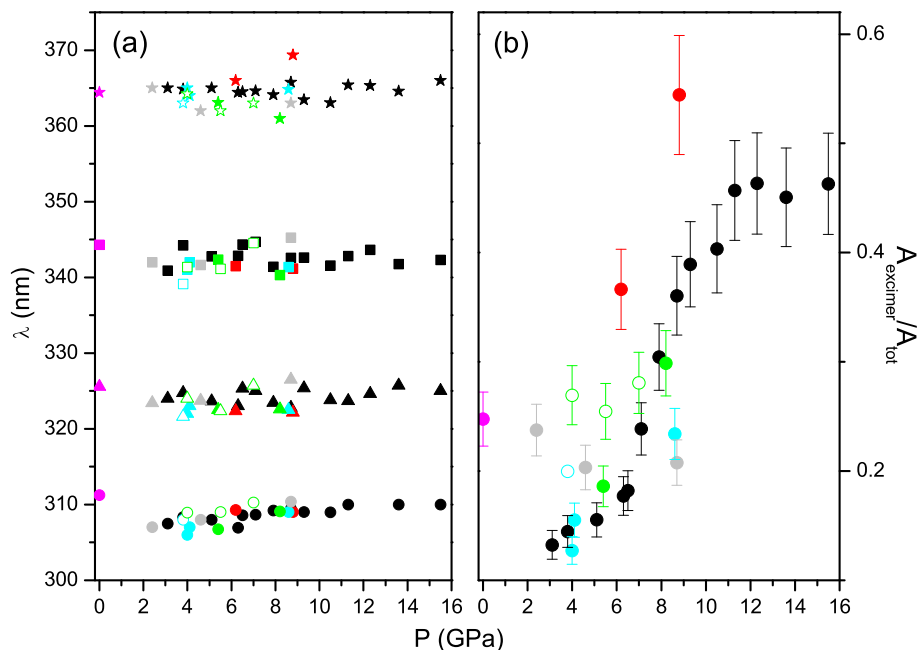


**Figure 1.18:** a) Central frequency of the fluorescence emission bands resulting from the fit procedure for several samples reported as a function of pressure. b) Relative area attributed to the pyridine excimer fluorescence band reported as a function of pressure in compression (full dots) and decompression (empty dots) experiments for: thermally annealed phase II (green), not annealed phase II (black), phase II obtained from phase I (grey), phase I (cyan), amorphous form (green), liquid at room conditions (violet).

order, presents at the same pressure almost about twice the excimer contribution to the total fluorescence (figure 1.18b).

It is also fundamental to notice that the total fluorescence emission is about 1-2 orders of magnitude more intense for the crystal compared to the amorphous in similar pressure conditions suggesting a structural origin for the emission enhancement induced in the crystal. Similar systems characterised by a  $n\pi^*$  character of the  $S_1$  as mono- and di-alkyl-pyridines are non-fluorescent also in the gas phase, although a weak fluorescence is observed in acidic solution due to the protonation of these molecules. It is shown that the generated emission came from a  $\pi\pi^*$  state becoming the lowest excited electronic

state in the protonated system [51]. We demonstrated that also for pyridine an acidification causes an enhancement of the fluorescence emission, as reported in figure 1.19 in which the fluorescence of solution of equal concentration of pyridine in ethanol and acetic acid are reported [50]. This behaviour was never observed before for pyridine because of experimental difficulties due to its very low fluorescence yield.

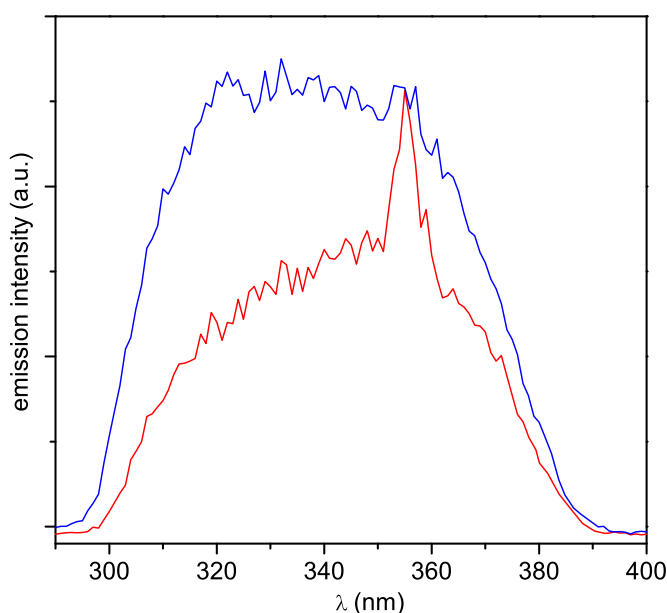


**Figure 1.19:** Comparison of the fluorescence emission of two equally concentrated pyridine solutions in ethanol (blue trace) and acetic acid (red trace) recorded in same conditions in a 10 mm quartz cuvette, showing an enhancement of the fluorescence emission especially in the blue region of the spectrum for the acidic solution

The strong intensification of emission in the crystal, estimated to be about 4-5 orders of magnitude compared to the liquid, is then connected to the structural changes induced by pressure. Each molecule in the crystal phase II has the nitrogen atom involved twice in  $N\cdots H$  contacts becoming stronger on raising pressure. This progressively lowers the energy of the non-bonding molecular orbital, mainly localised on the nitrogen  $sp^2$  hybrid orbital and directly involved in the H-bonds. This is consistent with the blue shift of the first

$n\pi^*$  transition with respect to the liquid phase, as also observed in acidic solution. We can thus conclude that the electronic structure of pyridine is strongly perturbed by the intermolecular interactions in the crystal, which become stronger on increasing the pressure up to the energy inversion of the  $n\pi^*$  and  $\pi\pi^*$  states, the latter becoming the  $S_1$  at high pressure, from which the fluorescence emission is allowed. Support to this theory came also from calculation performed for the pyridinium ion in which the energy sequence of  $\pi\pi^*$  and  $n\pi^*$  is inverted with respect to pyridine [52] and also from other examples in which the  $\pi\pi^*$  and  $n\pi^*$  inversion is claimed as cause for the enhancement of emission intensity observed upon crystallisation and compression of some heterocyclic aromatics [53].

#### 1.2.4 Summary

The high pressure polymorphism of pyridine at ambient temperature was studied by means of Raman and FT-IR spectroscopy to identify the stability regions of the thermodynamic phases and the connection between crystal structure and chemical reactivity. Two different crystalline phases and an amorphous form were identified and their pressure ranges of stability and metastability were investigated. Despite phase I is the stable solid phase at the lower pressures (0.6 - 1.0 GPa), it was never obtained on a direct compression of the liquid. Indeed, the liquid is easily supercompressed above the melting pressure (0.6 GPa) and it crystallises at higher pressure always in the phase II whose range of stability spans from 1.0 GPa up to the reaction threshold pressure. In some cases the crystallisation of the liquid was never observed, remaining in an amorphous form. Both amorphous form and phase I can be supercompressed in the stability range of phase II without observing any phase transition. These indications suggest that the three polymorphs have very similar energies and the energy barriers among them are so high that the phase transitions become kinetically driven, making the transformations sluggish and unclear. Any other proposed phase transition was ruled out and the phase II was found to be the stable phase up to the reaction threshold pres-

sure. The spontaneous reaction starts at about 17-18 GPa consisting in the destruction of the aromatic ring and the formation of an extended amorphous material. Despite some analogy with the reaction of benzene, the pyridine high pressure reactivity seems to be controlled by crystal defect, as the molecular approach needed for the seeding, by the formation of the initiator dimer, and the propagation of the reaction by lattice phonons is severely hindered by the network of highly energetic  $N\cdots H$  interactions. The reaction can be seeded by a suitable photoactivation at much lower pressure using two photon absorption, suggesting an activation process similar to that already observed for benzene through the formation of excimeric species. A confirmation to this hypothesis was given by a two-photon induced fluorescence study of pyridine in all its condensed forms as a function of pressure, using a picosecond pulsed source. For the first time the fluorescence emission of liquid and solid pyridine was observed and characterised as a function of pressure. The fluorescence quantum yield rapidly increases from the liquid up to the crystal phase II at 8 GPa of about 5-6 orders of magnitude. This intensification can be explained by the inversion of the lowest energy  $n\pi^*$  ( $^1B_1$ ) and  $\pi\pi^*$  ( $^1B_2$ ) excited electronic states as sketched in figure 1.20, due to the  $N\cdots H$  interac-

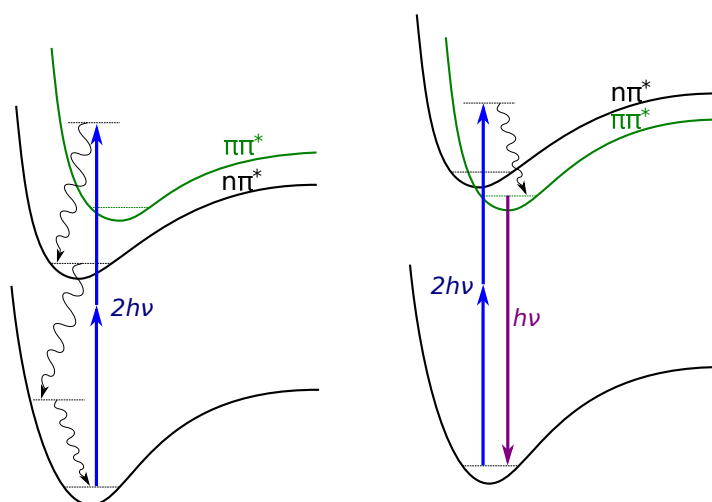


**Figure 1.20:** Sketch of the pressure effect on the electronic states of pyridine: the ambient pressure structure is reported on the left, while the hypothesised one at high pressure is reported on the right.

tions, strengthening in the crystal on raising pressure. In addition an emission band due to an excimeric form of pyridine was found, displaced by about  $5000\text{ cm}^{-1}$  from the exciton band. The non reversibility of the excimer emission intensity and the poor reproducible relative intensity among samples of different crystal quality suggest a non-structural nature of the excimer formation, suggesting that excimers are formed in solid pyridine only at crystal defects. This is in perfect agreement with the observation of a poor and not reproducible pressure induced reactivity among different samples. The pyridine case, in analogy with that of benzene, relates again the pressure induced reactivity to the formation of aggregate structures in crystals characterised by a peculiar electronic structure and able to trigger the chemical reaction, showing the importance of the characterisation of the electronic structure in high pressure conditions for a correct understanding of the chemistry in molecular crystals. Once more it is shown the key role of the molecular arrangement in the crystal structure in favouring or preventing the reactivity.

### 1.3 Triazine

In this section the modification induced on the electronic structure of the s-triazine (IUPAC name: 1,3,5-triazabenzene) and the connection with the high pressure induced reaction will be discussed. The s-triazine is an etheroaromatic compound which brute formula is  $C_3H_3N_3$ , being very rich in nitrogen. At room conditions s-triazine is a rhombohedral crystal belonging to the  $R\bar{3}c$  space group with two independent molecules in the unit cell [54]. A phase transition is observed on lowering the temperature at about 198 K [54, 55]. The low temperature phase is a monoclinic crystal with  $C2/c$  space group and two molecules in the primitive cell, differing from the  $R\bar{3}c$  structure by a shear in the  $a^*c$  plane of the non primitive hexagonal cell and by a rotation of the molecule about an axis parallel to the  $b$  crystallographic axis. The same phase transition is observed at ambient temperature on rising pressure at about 0.5 GPa [56]. Upon raising pressure at room temperature we could observe the re-

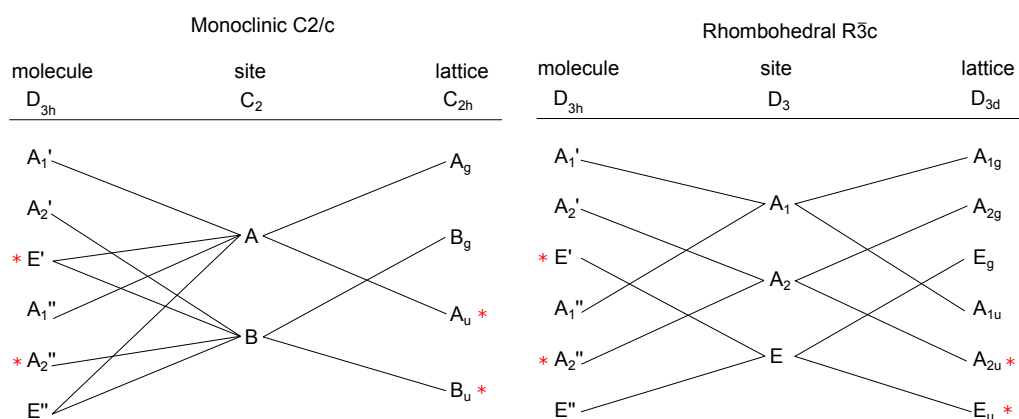


**Figure 1.21:** Correlation diagrams for the two crystalline phases of s-triazine. The stars indicate the IR-active modes.

ported phase transitions [54] by monitoring the infrared spectrum. Indeed, a strong and discontinuous modification in the infrared spectrum was observed between 0.45 and 0.75 GPa, as evidenced in figure 1.22 for the most significant regions. All the observed spectral features are easily accountable taking in account the correlation diagrams for the two crystalline phases reported in figure 1.21 as a confirmation of the occurred phase transition between the

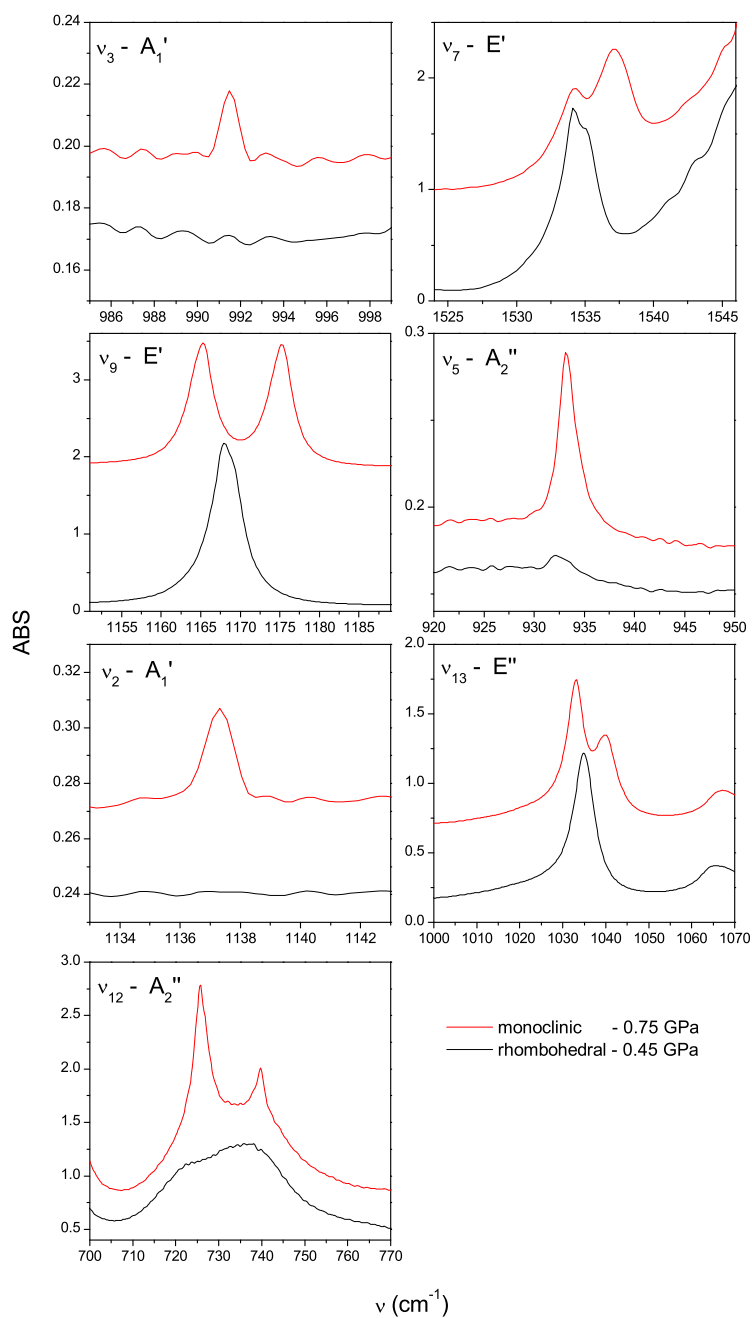


**Figure 1.22:** Infrared spectra recorded before and after the solid-solid phase transition observed at ambient temperature on rising pressure. The modes are labelled using the Wilson's notation for benzene [57], and for each mode is reported the symmetry in the  $D_{3h}$  molecular point group [54].

rhombohedral and the monoclinic crystal.

In figure 1.23 the pressure shift of some normal modes and the relative fit pro-



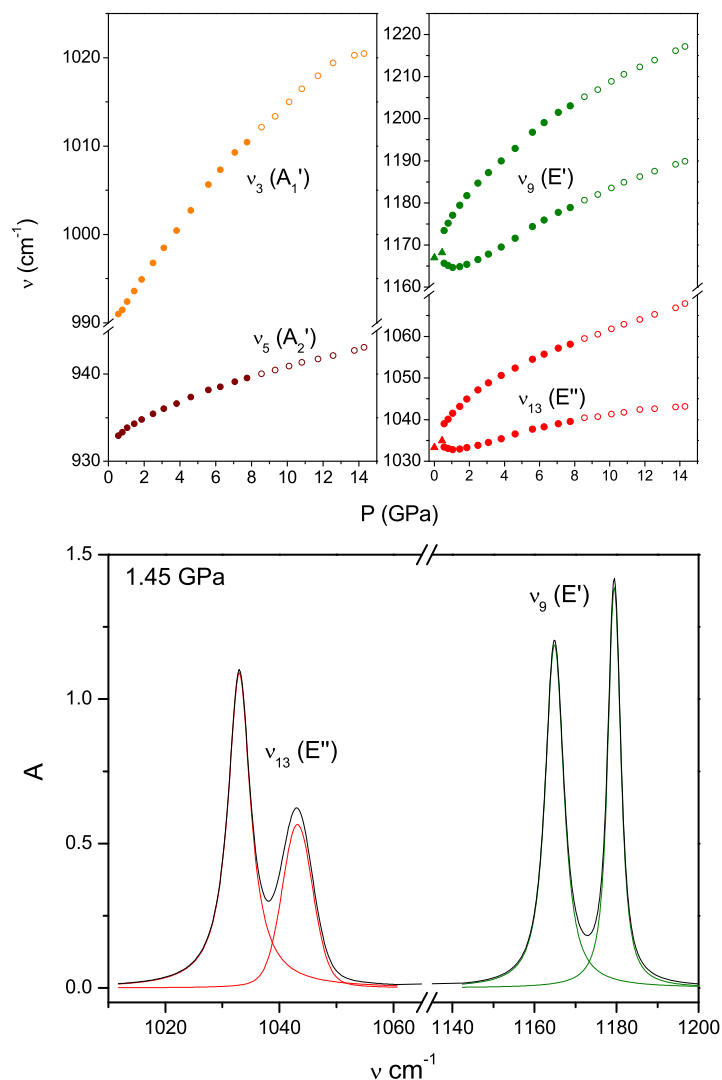


**Figure 1.23:** Central frequency evolution for the  $\nu_3$ ,  $\nu_5$ ,  $\nu_9$ ,  $\nu_{13}$  normal modes as a function of pressure as obtained by fitting the infrared spectra by Voigt profiles. In the upper panels triangles indicate data obtained from the phase I, dots from the phase II. Empty dots indicate values obtained from a sample which shows signs of the pressure induced chemical reaction. In the lower panel an example of fit is shown for the  $\nu_9$  and  $\nu_{13}$  modes.

cedure are shown. The  $\nu_3$  ( $A_1'$ ) and  $\nu_5$  ( $A_2'$ ) normal modes, that are not infrared active neither in the isolated molecule nor in the rhombohedral crystal, become active in the monoclinic phase, while the  $\nu_9$  ( $E'$ ) and  $\nu_{13}$  ( $E''$ ) modes are split each in two active infrared components. No signature of other phase

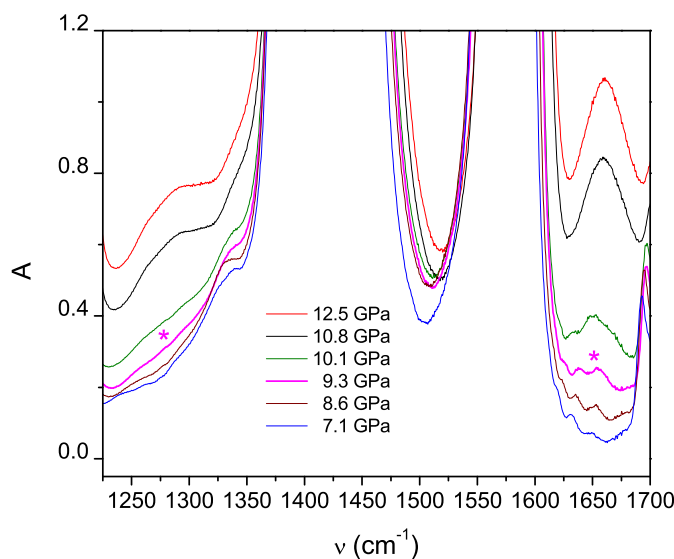


**Figure 1.24:** Infrared spectra of the triazine monoclinic phase as a function of the pressure in the spectral region typical of the C–N and C=N stretching mode. Compressing the crystal at pressure over about 8–9 GPa new broad bands not reversible in decompression appear in this region (evidenced by a star) indicating that a chemical reaction is observed.

transitions, such as discontinuities in the frequency or in the number of the modes, were observed on increasing pressure up to 15 GPa, a value greater than the pressure of the spontaneous reaction, meaning that the monoclinic crystal is the stable phase up to the reaction threshold. Indeed a spontaneous reaction is observed when triazine is compressed over 8-9 GPa, when new bands that are not reversible in decompression appear in the infrared spectra. In figure 1.24 the main bands that can be attributed to an amorphous compound rich in nitrogen, are shown. The product bands intensify almost immediately for any further compression step, indicating a progressive consumption of triazine. The almost complete transformation of the triazine is observed in a compression-decompression cycle up to about 20 GPa.

### 1.3.1 Electronic properties

The highest energy occupied molecular orbitals of triazine are of non-bonding  $n$ -type character, mainly localised on the three nitrogen atoms, while the lowest unoccupied electronic molecular orbitals are  $\pi^*$  [61]. As reported in figure 1.25 two groups of  $n\pi^*$  transition are predicted. The lowest energy  $n\pi^*$  transition set involves the  $n$ -orbitals of  $E'$  symmetry and the  $E''$   $\pi^*$  states, giving four states having respectively  $A_2''$ ,  $E''$  and  $A_1'$  symmetry, among which only the transition to the  ${}^1A_2''$  state is dipole allowed from the ground state [59]. Both

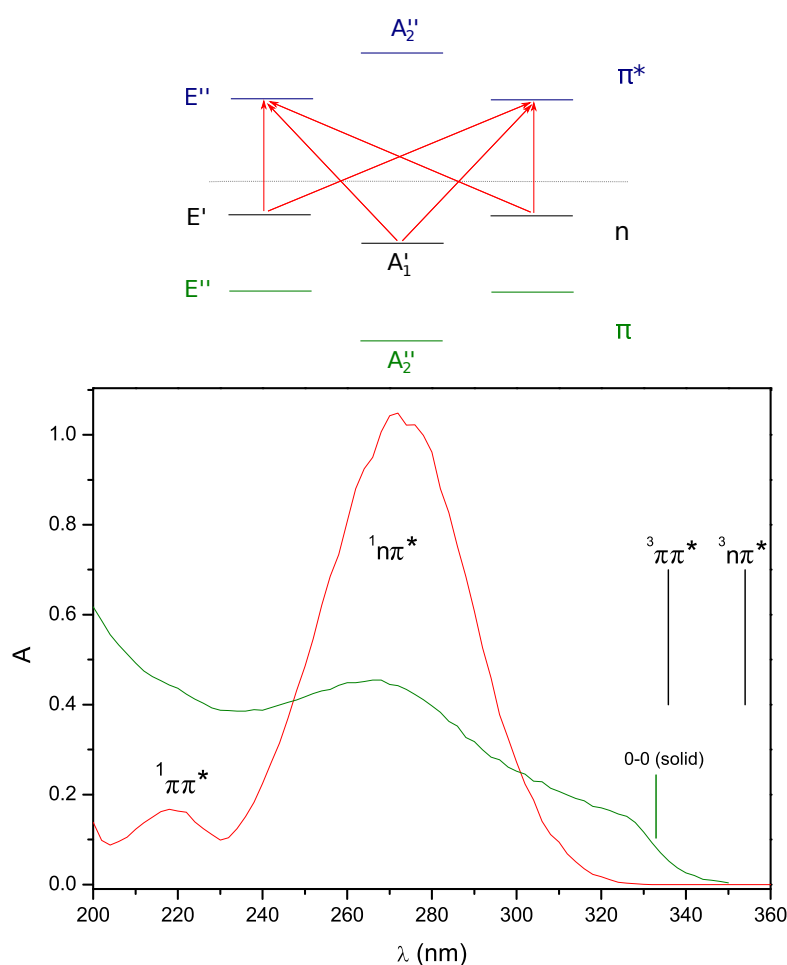


**Figure 1.25:** Scheme of the frontier orbital energy for the single molecule of *s*-triazine and of the measured UV absorption spectra in a isooctane solution (red trace) and in the rhombohedral crystal triazine at room conditions (green trace) and relative assignment [58–60]. The red arrows represent the  $n\pi^*$  transitions and near each orbital is reported the relative symmetry.

calculations [61, 62] and experiments [63] show that the lower energy singlet  $n\pi^*$  state corresponding to the electronic origin for the single molecule belongs to the  $E''$  symmetry. The second set of  $n\pi^*$  transitions involves the lower energy  $n$ -orbital of  $A'_1$  symmetry and the  $E'' \pi^*$  orbitals, giving another  $E''$  state, that can interact with the state of same symmetry given by the previous set, through higher order configurational interaction. These features are observed both in the gas phase and in solution giving rise to an intense absorption band centred at about 272 nm in apolar solution of cicloesane. At higher energy lies the first  $\pi\pi^*$  transition that is assigned to the dipole moment forbidden  ${}^1A'_1 \rightarrow {}^1A'_2$  transition whose absorption maximum is observed in the apolar solution at about 222 nm [58] with a cross section that is almost 1/3 with respect to that of the allowed  $n\pi^*$  transition. Indeed the first set of  $\pi\pi^*$  transitions involves the couple of  $\pi$  and  $\pi^*$  molecular orbitals of  $E''$  symmetry giving rise to the  $E'' \otimes E'' = A'_1 + A'_2 + E'$  states. Among them only the transition to the  $E'$  state is one-photon allowed in the isolated molecule and its energy is predicted to be over 7.7 eV above the ground state, with the transition laying in the vacuum-UV (160 nm). The transition from the ground state to the  $A'_2$  is two photon allowed. The electronic origin corresponding to the first  $n\pi^*$  transition ( ${}^1E''$  state), that is activated in the crystal, is observed in the rhombohedral phase at room conditions at 333 nm [60]. We measured the UV absorption spectra of s-triazine in solution of an apolar solvent and in a thin layer of crystal at room conditions, as reported in figure 1.25. The spectra are perfectly consistent with the previous discussion. In the high pressure monoclinic phase all the aforementioned electronic transition are predicted to be active for both one and two photon mechanism. Triazine is known to be fluorescent at least in the vapour phase, emitting from the  ${}^1E''$  electronic state of  $n\pi^*$  character [64–66]. We performed a two photon induced fluorescence study as a function of pressure in the whole range of stability of the monoclinic phase up to the reaction threshold pressure, evidencing how the electronic structure is modified by the increasing density. In figure 1.26 the two photon excitation and fluorescence spectra recorded on increasing pressure

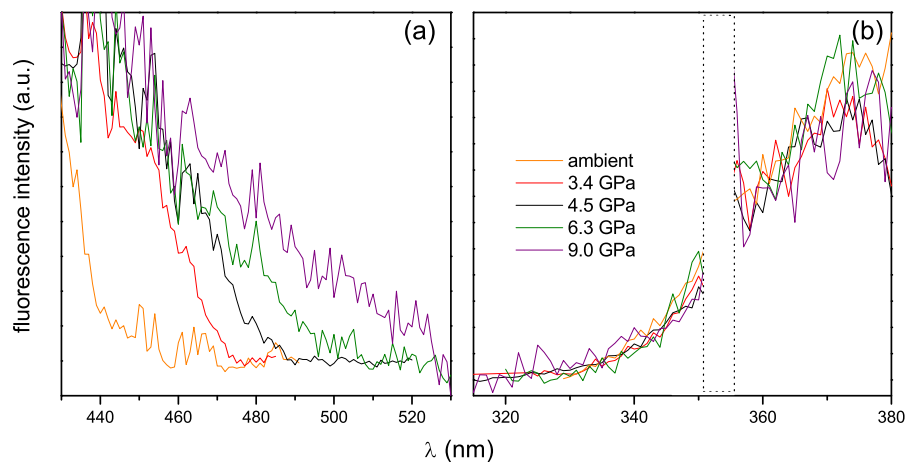


**Figure 1.26:** Two photon excitation (a) and relative induced fluorescence (b) spectra of solid triazine as a function of pressure recorded in the diamond anvil cell. The excitation spectra are recorded revealing the fluorescence around the maximum emission while all the fluorescence spectra are recorded exciting at 436 nm.

are reported. The first evidence, looking at the two photon excitation profile recorded at ambient pressure (orange trace in figure 1.26), is that the cross section for all the  $n\pi^*$  transitions is so low that the emission induced by two photon exciting triazine in the DAC on these states is under our sensitivity. The lowest energy signal in the excitation profile correspond to the  $\pi\pi^*$  transition at about 444 nm ( $\sim 45000\text{ cm}^{-1}$ ). Correspondingly, the fluorescence spectra could only be measured by exciting on the  $\pi\pi^*$  states. For this reason, the red part of the emission can not be observed due to the overlap between the excitation and detection wavelengths. We have then access to two important data about the electronic structure of the triazine crystal. The blue edge of the fluorescence spectrum is the electronic origin of the lowest energy  $n\pi^*$  state ( $S_1$ ) and can be taken as a measure of the energy separation between the  $n$  and  $\pi^*$  molecular orbitals. The red edge of the observed excitation profile, on the other hand, can be considered as the energy separation between the  $\pi$  and  $\pi^*$  molecular orbital. On rising the pressure a macroscopic red shift of the  $\pi\pi^*$

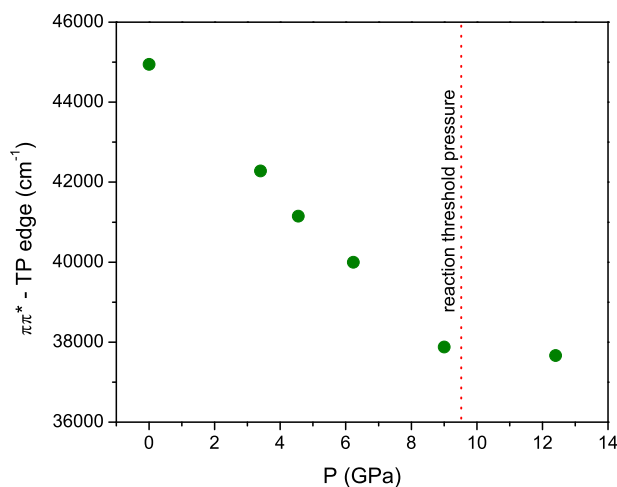


**Figure 1.27:** Estimation of the edge of the  $\pi\pi^*$  transition obtained from the excitation spectra of triazine as a function of the pressure. The pressure at which the first signs of reaction were observed from the infrared spectra is reported in the graph and indicated as reaction threshold pressure

transition is observed, whereas the blue edge of the fluorescence spectrum is not affected by pressure. We can correlate the behaviour of the spectroscopic data just described with the pressure effect on the molecular orbitals involved in the absorption and emission phenomena. In detail, the pressure independence of the emission means that the energy separation between the  $n$  and  $\pi^*$  molecular orbitals is constant as a function of pressure. Instead, the red shift of the  $\pi\pi^*$  transition can be correlated to a pressure induced decrease in the energy separation between  $\pi$  and  $\pi^*$  molecular orbitals. Then, looking at the sequence of the molecular orbitals reported in figure 1.25, we can suppose that the  $\pi$  molecular orbitals are destabilised by the increased density with respect to the  $n$  molecular orbitals. Indeed, the energy difference between the  $n$  and  $\pi$  molecular orbitals, that is  $\sim 15000 \text{ cm}^{-1}$  at ambient pressure, is estimated to be  $\sim 7000 \text{ cm}^{-1}$  at 10 GPa.

In figure 1.27 is reported the evolution of the red edge of the  $\pi\pi^*$  transition estimated from the excitation profiles of triazine as a function of pressure to better understand the entity of the destabilisation induced on the  $\pi$

molecular orbitals. When the destabilisation of  $\pi$  molecular orbitals is such that the lowest energy of the  $\pi\pi^*$  transitions become  $\sim 37000\text{ cm}^{-1}$ , the edge is no more red-shifted by a further pressure increase, and a chemical reaction is induced, determining the aromatic ring breaking and the rearrangement of the molecular crystal to an amorphous compound.

### 1.3.2 Summary

The two photon induced emission from s-triazine was studied as a function of pressure in the range of stability of the monoclinic phase up to the threshold pressure of the spontaneous reaction at about 9 GPa. Using the single molecule description, that is demonstrated to be reliable also in the description of the solid emission by taking into account the crystal field effect, we assigned the observed spectral features in the monoclinic phase. By the comparative analysis of the two photon excitation spectra and the fluorescence emission we observed a huge red-shift of the  $\pi\pi^*$  transition induced by the increasing density, while the  $n\pi^*$  transition is substantially unaltered being constant up to the highest pressure reached. We were able to explain these features by a pressure induced destabilisation of the  $\pi$  molecular orbitals, that are connected to the aromatic stabilisation of the triazine ring. When the energy of the  $\pi$  orbitals is increased so much as to be comparable to the non bonding  $n$ -orbitals, meaning that the aromatic stabilisation is almost negligible, the ring becomes unstable and a chemical reaction to an extended system is observed. This pressure is found to be about 9 GPa, a value that is almost half of the pressure needed for the reaction in pyridine (see previous section). This is indeed a very explanatory example of how the pressure is a powerful tool to induce changes on the electronic structure of simple molecules with huge implications in the crystal phase reactivity.

## 1.4 Picene

Picene is a condensed aromatic hydrocarbon made by five fused benzene rings arranged in an armchair configuration. The armchair configuration gives to the molecule higher stabilisation energy with respect to the linearly arranged isomer, the pentacene [67], which corresponds to higher chemical stability and larger HOMO-LUMO energy gap. In addition to the interest aroused by the possibility of acting as good reactant for the high pressure production of amorphous hydrogenated carbon, which is of high technological appeal, the study of picene is also interesting for its potential use as a superconductor. Indeed it is shown that upon doping with potassium atoms, picene shows superconductivity at relatively high temperature ( $T_c = 18$  K for  $K_3$ -picene) [68]. The action of the alkali metal doping induces changes in the electronic structure and a reduction of about 6% of molar volume with respect to pristine picene [68], a typical volume reduction value obtained by applying to similar compounds an external pressure in the range of about 1 GPa [69]. In addition, it is shown a large positive dependence of the  $T_c$  on compressing the  $K_3$ -picene estimated in about 12.5 K/GPa up to 1.2 GPa [70]. As discussed in the previous sections, the effect of pressure on electronic structure of aromatic and etheroaromatic compounds can be extremely pronounced, and the effect of pressure could be fundamental for the attainment of superconductivity also in pristine picene. For a good understanding of the mechanism at the bases of these phenomena the characterisation of the pressure evolution of the electronic structure is then mandatory, searching for an eventual electronic band gap closure as precursor sign of an hypothetical superconductivity of the pristine picene crystal generated only by pressure.

### 1.4.1 Single molecule and crystal electronic properties

The only data available on the molecular electronic properties are the ambient pressure absorption, fluorescence and phosphorescence spectra of a glass solution of picene at 77 K in an apolar solvent [71]. As reported in figure



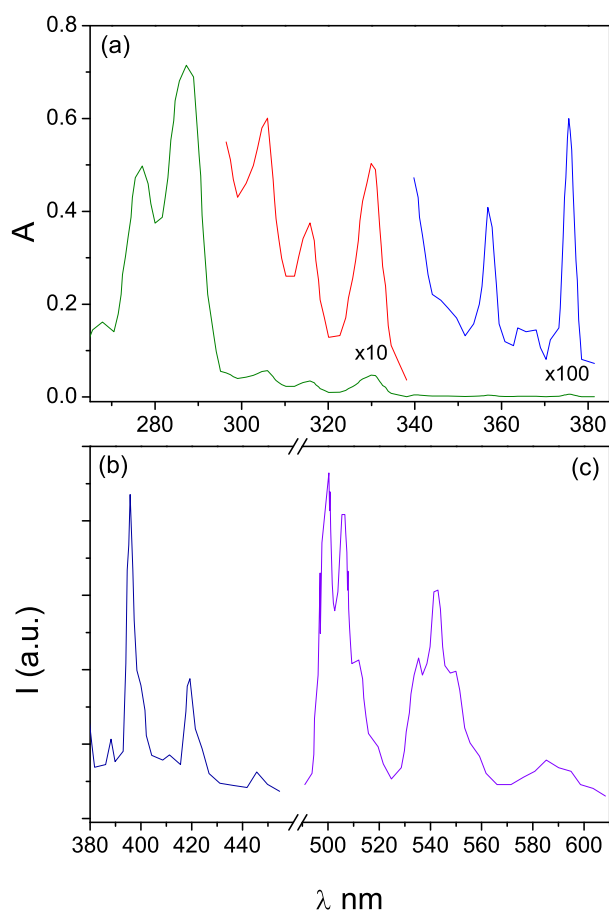


**Figure 1.28:** Absorption (a), fluorescence (b) and phosphorescence (c) spectra of a glass solution of picene in at 77 K [71].

1.28 the UV-visible absorption spectra is dominated by the transitions from the ground state to the four lowest energy electronic excited states, named for sake of simplicity using Platt's perimeter model [72] as  $L_a$ ,  $L_b$ ,  $B_a$ ,  $B_b^\ddagger$ . According to this model the first four singlet transitions arise from the excitation of a single electron from the HOMO or HOMO-1 to the LUMO or LUMO-1 molecular orbitals, mixed by configuration interaction. In particular the  $^1L_a$  state correspond to the HOMO-LUMO excitation and the  $^1B_a$  to the

<sup>‡</sup> The original free-electron model was extended in the LCAO-MO form by Moffit [73] and despite its simplicity it gives results in very good accordance with the experimental observation. It is nowadays of wide use because the nomenclature of the states is independent of the molecular symmetry allowing simple and fast qualitative identification of the observed electronic transitions for very different aromatic systems.

HOMO–1-LUMO+1 excitation while the *b* states originate from the mixing of the HOMO-LUMO+1 and HOMO–1-LUMO that are at very similar energy. The extent of the configuration interaction determines which is the lowest excited state between  $^1L_a$  and  $^1L_b$ . The  $^1L_b$  one-photon transition is easily recognisable from  $^1L_a$  because of the expected smaller transition moment, that is usually two orders of magnitude smaller than  $^1L_a$ . The *a* and *b* states can be distinguished also in polarized light, as they are mutually orthogonal, and by the different solvatochromic effect: *a* states have electronic densities mainly localized on atoms with nodal planes bisecting the bonds and the opposite holds for *b* states. Then, conversely to the *b* states, the energy of *a* states is strongly dependent on the molecular geometry and on the properties of the chemical environment, such as the solvent polarity. Picene molecular symmetry belongs to  $C_{2v}$  point group and in this symmetry  $^1L_b$  and  $^1B_b$  are  $^1a_1$  states and  $^1L_a$  and  $^1B_a$  are  $^1b_2$  states. Within this framework, we investigated the optical properties of picene in solution with solvents of different polarities and in the solid phase at ambient conditions [74], measuring the UV-visible absorption spectra, the fluorescence spectra and the excitation profiles using both one and two photon excitation mechanisms. The acquired knowledge was then employed to the interpretation of the changes induced by the application of an external pressure on picene crystal and of the mechanism of pressure induced reactivity [75]. The absorption and one-photon induced fluorescence spectra were measured in dilute solutions of about  $10^{-3} - 10^{-6}$  M of picene in an apolar (isopentane) and a highly polar solvent (acetonitrile) to better appreciate the solvatochromic effect. The low concentration is fundamental to limit phenomena like autoabsorbance of the fluorescence (inner filter effect), and avoid saturation and other effects not ascribable to the single molecule.

The absorption spectra measured in the different solvents present similar features. An example is reported in figure 1.29. The main difference is represented by an overall red shift of the whole absorption band in the polar solvent. As expected from the Platt's model and in accord to other con-

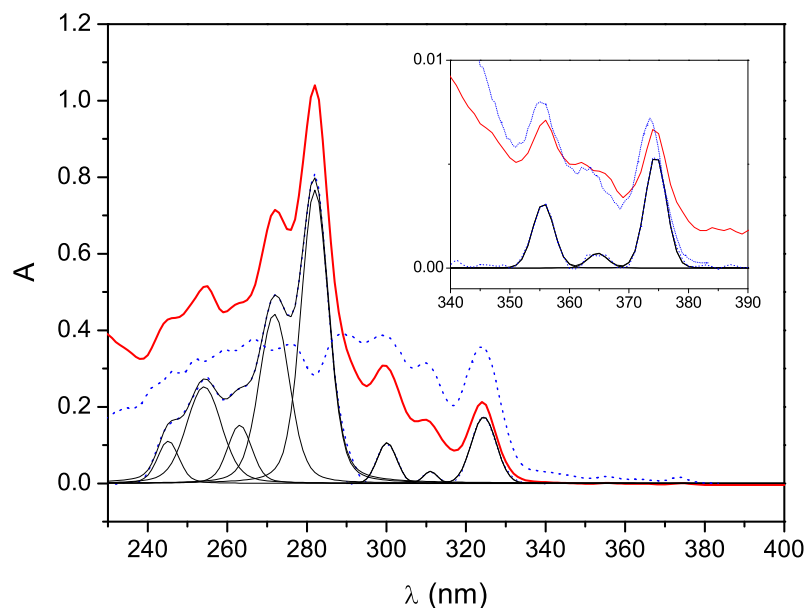


**Figure 1.29:** One photon absorption spectrum of a  $10^{-3}$  M solution of picene in isopentane (red trace) and relative deconvolution made by Voigt profiles superimposed to the one-photon excitation profile detecting fluorescence at 397 nm (blue dotted trace). In the inset a detail of the low frequency absorption is reported.

densed aromatics [76] we observe in the absorption pattern three distinct regions ( $S_1$  : 380–340 nm,  $S_2$  : 340–290 nm,  $S_3$ - $S_4$  : 290–240 nm), corresponding to the single electron transition from the ground state to  $^1L_b$ ,  $^1L_a$  and to the B states, respectively. The spectra were fit by Voigt profiles and the results are reported for the two solvents in table 1.3 in which an assignment is proposed [74].

According to previous data obtained in polarized light in the glass solution [71] and time dependent DFT-calculations [77], and in agreement with the solvatochromic effect (quantified by  $\Delta\nu^c$  in table 1.3), we can conclude that  $S_1$  is  $^1L_b$  and  $S_2$  is  $^1L_a$  with an energy separation between the two states of about  $4000\text{ cm}^{-1}$ . Indeed the red shift of the  $S_0 \rightarrow S_1$  transition due to the observed solvatochromic effect is about 1/3 of the one of the  $S_0 \rightarrow S_2$  transition as expected for the minor sensitivity of  $L_b$  transition energy to chemical envir-

assignment	isopentane			acetonitrile			$\Delta\nu^b$
	$\lambda$ (nm)	$\nu$ (cm <sup>-1</sup> )	$\Delta\nu^a$	$\lambda$ (nm)	$\nu$ (cm <sup>-1</sup> )	$\Delta\nu^a$	
0 - 0	375.2	26655		376.1	26588		67
0 - 0 + $\sim$ 250	378.4	26426	229	379.6	26340	247	86
0 - 0 + $\sim$ 865	387.8	25789	866	388.4	25743	844	46
0 - 1	395.9	25262	1393	396.6	25211		51
0 - 1 + $\sim$ 250	399.6	25024	1401	400.5	24969	1371	55
0 - 1 + $\sim$ 865	409.6	24413	1376	410.2	24381	1362	32
0 - 2	419.3	23853	1408	420.0	23810	1401	43
0 - 2 + $\sim$ 250	424.0	23588	1437	425.3	23515	1455	73
0 - 2 + $\sim$ 865	433.6	23061	1352	433.9	23048	1333	13
0 - 3	444.7	22485	1368	445.7	22436	1374	49
0 - 3 + $\sim$ 250	450.9	22176	1411	452.5	22099	1415	77
0 - 3 + $\sim$ 865	460.7	21707	1353	460.9	21699	1350	8

**Table 1.1:** Frequencies of fluorescence peak maxima of picene solutions, where  $\Delta\nu^a$  is the frequency difference between bands belonging to the same vibronic series or between the electronic origin and a vibronic origin and  $\Delta\nu^b$  is the frequency difference between corresponding vibronic bands in the two solvents.

onment changes [76]. Analogous conclusion can be drawn for the pattern in the 290 – 240 nm region, in which we can identify on the same basis the  $^1B_a$  state as  $S_3$  and  $^1B_b$  as  $S_4$ , which origins are separated by an energy of about 3700 cm<sup>-1</sup>.

An example of fluorescence spectra is reported in figure 1.30. The spectral features are found to be independent of the employed excitation wavelength in the range 375-270 nm, implying relaxed fluorescence from  $^1L_b$  which has been demonstrated to be the  $S_1$  state. Relaxed fluorescence is also confirmed by the independence on the detection wavelength of the excitation profile, that in addition well reproduces the absorption spectrum (figure 1.29). The proposed assignment is reported in table 1.1. Three series of vibronic bands were identified, starting from the 0-0 electronic origin and other two vibronic origin at 250 and 865 cm<sup>-1</sup> from the electronic origin<sup>§</sup>, and built on the  $a_1$  mode at about 1375 cm<sup>-1</sup> in  $S_0$ , in perfect agreement with the previously reported measurements[71].

<sup>§</sup> these two frequency agree with two vibrational mode of  $A_1$  symmetry at 261 and 864 cm<sup>-1</sup> [78, 79] that can be responsible for the vibronic coupling

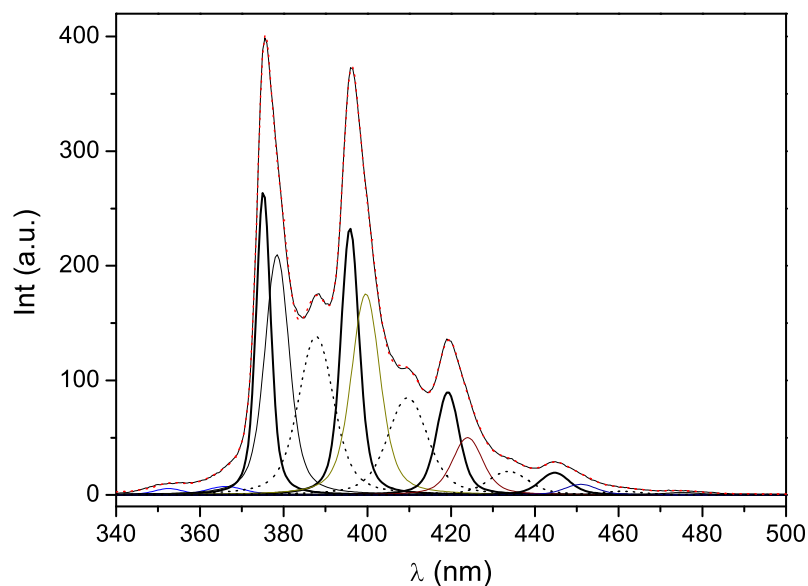


**Figure 1.30:** One photon induced fluorescence of a  $10^{-6}$  M solution of picene in acetonitrile and relative deconvolution made by Voigt profiles. The fluorescence spectral features are independent from the chosen excitation wavelength. For the reported spectrum  $\lambda_{exc}$  was 325 nm.

Pure pristine picene at room condition is a monoclinic  $P2_1$  crystal with two independent molecules in the asymmetric unit, constituted by layers of molecules arranged in a herringbone structure parallel to the crystallographic  $ab$  planes and with the main molecular axis roughly parallel to the  $c$ -axis [80]. The site group is  $C_1$  and the factor group is  $C_2$  implying that each vibronic state is split in two components of A and B symmetry both allowed by one and two photon absorption. However the perturbation induced by the crystal field is expected to be small, as confirmed by the vibrational spectrum of the crystal that can be assigned on the basis of the single molecule description [78, 79].

Both absorption and fluorescence spectra of solid picene are markedly red shifted with respect to the single molecule in solution (see figure 1.31, 1.32 and table 1.2). Indeed the electronic origin in the solid (383.5 nm) is red-shifted by  $\sim 625\text{ cm}^{-1}$  and, most relevant, the relative transition moment in the 340-385 nm region with respect to shorter wavelengths in one photon absorption

Absorption spectrum				Fluorescence spectrum			
assignment	$\lambda$ (nm)	$\nu$ (cm <sup>-1</sup> )	$\Delta\nu^a$	assignment	$\lambda$ (nm)	$\nu$ (cm <sup>-1</sup> )	$\Delta\nu^a$
$S_1$ 0 - 0	383.5	26076		0 - 0	385.5	25940	
$S_1$ 0 - 0 + ~ 600	374.3	26717	641	0 - 0 + 534	393.6	25406	534
$S_1$ 0 - 1	364.2	27457	1381	0 - 1	406.3	24612	1328
$S_1$ 0 - 2	346	28902	1445	0 - 1 + 534	415.7	24056	1350
$S_1$ 0 - 3	329.5	30349	1447	0 - 2	429.8	23267	1345
$S_2$ 0 - 0	319	31348		0 - 2 + 534	440.7	22691	1365
$S_2$ 0 - 1	313	31949	601	0 - 3	455.5	21954	1313
$S_2$ 0 - 2	307	32573	624	0 - 3 + 534	467.8	21377	1314
$S_3$	297	33670		0 - 4	484.7	20631	1323
				0 - 4 + 534	500.5	19980	1397

**Table 1.2:** Peak maxima in the absorption and fluorescence spectra of solid picene and proposed assignment.  $\Delta\nu^a$  is the frequency difference between bands belonging to the same vibronic series or between the electronic origin and a vibronic origin. The vibronic origins are reported in the “assignment” column indicating the frequency separation (in cm<sup>-1</sup>) with respect to the electronic origin for each excited state ( $S_n$  0 – 0). For each assigned band the vibrational quantum numbers, for the initial and the final state respectively, are also reported.

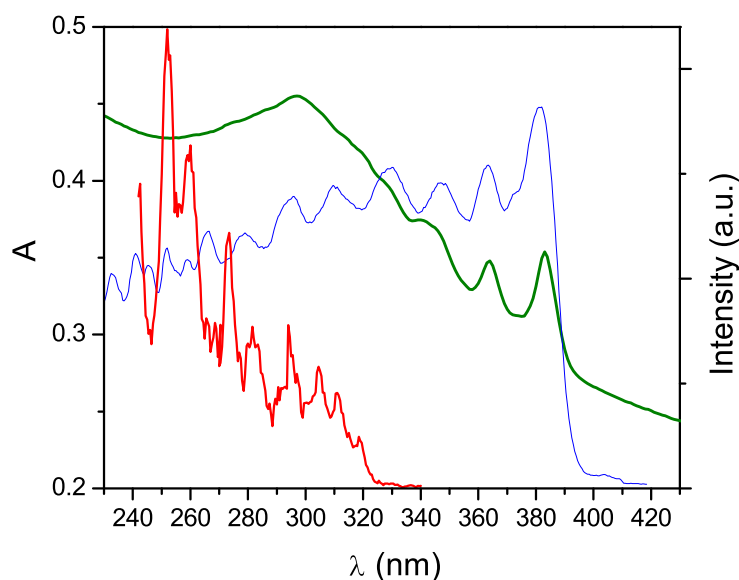


**Figure 1.31:** Absorption spectrum of a thin layer of solid picene in a quartz window (green trace) superimposed to one (blue trace) and two photon excitation profile (red trace) on the same sample revealing the maximum of fluorescence.

assignment	isopentane			acetonitrile			$\Delta\nu^b$	$\Delta\nu^c$
	$\lambda$ (nm)	$\nu$ (cm <sup>-1</sup> )	$\Delta\nu^a$	$\lambda$ (nm)	$\nu$ (cm <sup>-1</sup> )	$\Delta\nu^a$		
S <sub>1</sub> 0 - 0	374.6	26698	692 1418 1410	375.2	26650	669 1395 1435	48	74
S <sub>1</sub> 0 - 0 + ~ 680	365.1	27390		366.0	27319		71	46
S <sub>1</sub> 0 - 1	355.7	28116		356.6	28045		71	120
S <sub>1</sub> 0 - 1 + ~ 680	347.2	28800		347.8	28754		46	
S <sub>2</sub> 0 - 0	324.4	30825	1312 1193	325.9	30689	1320 1214	136	500
S <sub>2</sub> 0 - 0 + ~ 1315	311.2	32138		312.4	32009		129	452
S <sub>2</sub> 0 - 1 + ~ 1315	300.0	33331		301.0	33224		107	598
S <sub>3</sub> 0 - 0	282.0	35461		282.5	35403		63	678
S <sub>3</sub> 0 - 1	271.8	36792	1326 1302	272.3	36719	1316 1260	73	652
S <sub>3</sub> 0 - 2	262.5	38094		263.3	37979		115	766
S <sub>4</sub> 0 - 0	255.2	39178		255.3	39174		4	
S <sub>4</sub> 0 - 1	251.4	39777		251.4	39781		-4	
S <sub>4</sub> 0 - 2	247.3	40437	599 659 590	247.3	40441	606 660 596	-4	
S <sub>4</sub> 0 - 3	243.8	41026		243.7	41038		-12	

**Table 1.3:** Frequencies of peak absorption maxima of picene solutions, where:  $\Delta\nu^a$  is the frequency difference between bands belonging to the same vibronic series or between the electronic origin and a vibronic origin;  $\Delta\nu^b$  is the frequency difference between corresponding vibronic bands in the two solvents;  $\Delta\nu^c$  is the frequency difference between corresponding bands in isopentane and in organic glass at 77 K [71]. .

spectra is much larger in the solid than the apolar solution. In the two photon excitation spectra there is a steep increase of cross section at about 325 nm, indicating a red edge of the transition to another electronic excited state, implying a blue shift of 566 cm<sup>-1</sup> of the S<sub>2</sub> (<sup>1</sup>L<sub>a</sub>). Both blueshift of the L<sub>a</sub> state and the relative one photon absorption cross section increase in the low frequency region can be explained taking in account the crystal field effect through the coupling between the L<sub>a</sub> states of nearest molecules that form an upper and a lower state, the latter at similar energy of the L<sub>b</sub> state, already observed in similar cases [81]. This can give an explanation of the larger relative optical dens-

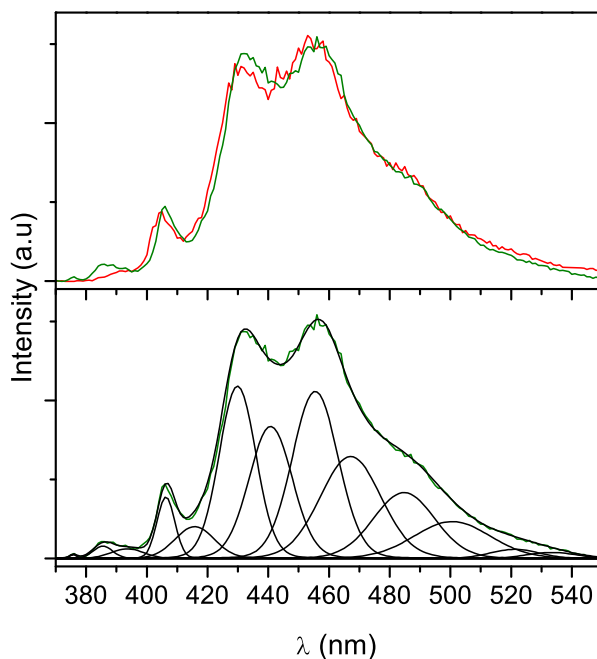


**Figure 1.32:** One (green trace) and two photon (red trace) induced fluorescence spectra of solid picene in the form of micrometric needles in a quartz window and deconvolution made by Voigt profiles of the OP fluorescence spectra.

ity in the low frequency observed for the solid, since the  $^1A_1 \rightarrow ^1L_a$  has much larger dipole transition moment with respect to the  $^1A_1 \rightarrow ^1L_b$  transition. All the observed bands of the crystal can be assigned to transitions between molecular electronic states (see table 1.2). The molecular character is maintained as demonstrated by the observation of a clean vibronic structure, although the effect of the crystal field is non-negligible as confirmed by the changes in intensity patterns and frequency shifts of the bands.

#### 1.4.2 Pressure evolution of electronic structure

We measured the UV-visible absorption spectra of a picene single crystal as a function of pressure in a diamond anvil cell using argon as pressure medium[75]. The spectra are reported in figure 1.33. Due to the large thickness of the sample ( $\sim 10 \mu\text{m}$ ) and to the high absorptivity of solid picene [74], the spectra are saturated and only the red edge of the one-photon absorption is detect-



able. This prevents a direct identification of the exciton band frequency (optical band gap). An approximation to the evolution of the optical band gap as a function of pressure can be extracted by choosing a fixed absorbance value and reporting the wavelength at which this value is reached as a function of pressure. This method is not valid a priori, because the pressure may also affect intensity and bandwidth of the electronic transition, giving an overestimate of the band gap shift for the saturated band [24]. However, it seems here not the case, because the resulting pressure shift, estimated in about  $\sim 400 \text{ cm}^{-1}/\text{GPa}$ , is not dependent from the chosen absorbance value used for the calculation, apparently indicating that both bandwidth and intensity of the exciton band are not appreciably modified by pressure. This conclusion will be also confirmed by two photon measurements, which are not affected by saturation effects, that will be discussed in the following. The results are reported in figure 1.35. The huge red shift of the absorption edge as a function of pressure is similar in magnitude to that observed for other aromatic crystals like pentacene ( $\sim 650 \text{ cm}^{-1}/\text{GPa}$ ) whose first electronic state is  $^1L_a$ , giving support to the hypothesis that crystalline picene  $S_1$  derives from  $^1L_a$  state.

The spectra are perfectly reversible in compression-decompression cycles up to 14 GPa. However, for pressures above 11 GPa some regions of the crystal, apparently the most stressed, such as the extremity in contact with the gasket and the central part damaged upon loading, start becoming red as clearly visible from the absorption spectra (figure 1.33), being not reversible in pressure download. This is an indication of an irreversible transformation occurring preferentially at crystal defects. Indeed, the spectrum of the transformed parts undergoes a blue shift for pressure down to  $\sim 8 \text{ GPa}$ , and it abruptly changes for lower pressures with the formation of a broad band at  $\lambda > 480 \text{ nm}$ , indicating further chemical transformations.

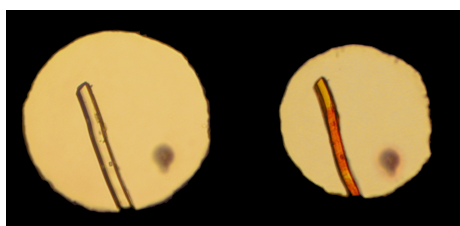
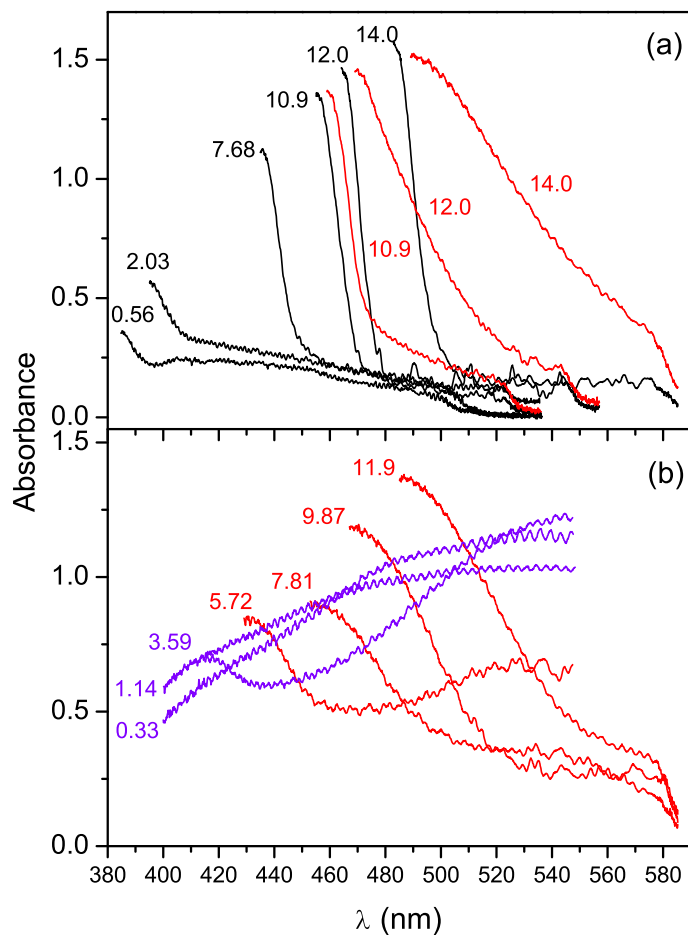


**Figure 1.33:** UV-visible absorption spectra of a single crystal of picene as a function of pressure (expressed in the graph in GPa). a) Spectra measured in compression on the transparent part of the sample (black traces) and on the red parts (red traces). b) Spectra measured in decompression on the red part of the sample. Abrupt changes in the spectrum are observed below  $\sim 4$  GPa (violet traces). On the bottom, two photograph of the sample recorded respectively at 0.56 (on the left) and 14.0 GPa (on the right).

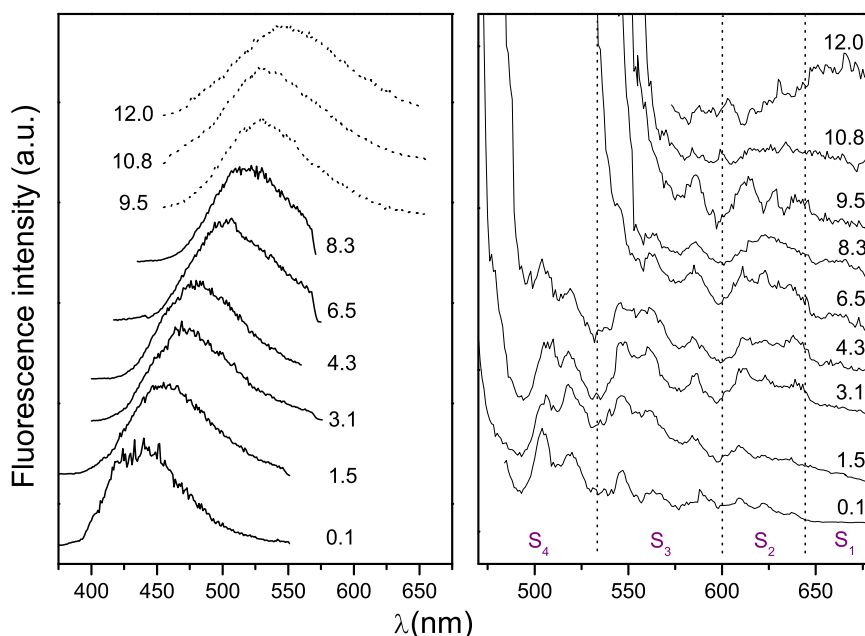


**Figure 1.34:** On the left, one (dotted lines, exciting range: 620-670 nm) and two photon (solid lines, exciting at 480 nm) induced fluorescence spectra reported as a function of pressure for polycrystalline picene. On the right, two photon excitation profiles measured as a function of pressure for polycrystalline picene revealing on the maximum of the fluorescence emission. The pressure values are reported in GPa.

We performed one and two photon induced fluorescence measurements on polycrystalline picene samples as a function of pressure up to 12 GPa, not using any pressure medium [75] (figure 1.34). Also in this case a perfect reversibility in decompression was found. At each pressure the fluorescence spectrum is found to be independent from the excitation wavelength, indicating a relaxed fluorescence mechanism. Applying the same kind of analysis already described for the ambient pressure crystal, we found at the lowest pressure (0.1 GPa) the same band patterns. The band centres obtained by a fitting analysis using Voigt profiles are reported in figure 1.35. We can observe a red shift of the whole spectrum, whose pressure dependence is perfectly in agreement with the  $S_0 \rightarrow S_1$  optical band gap estimation made by direct UV-visible ab-

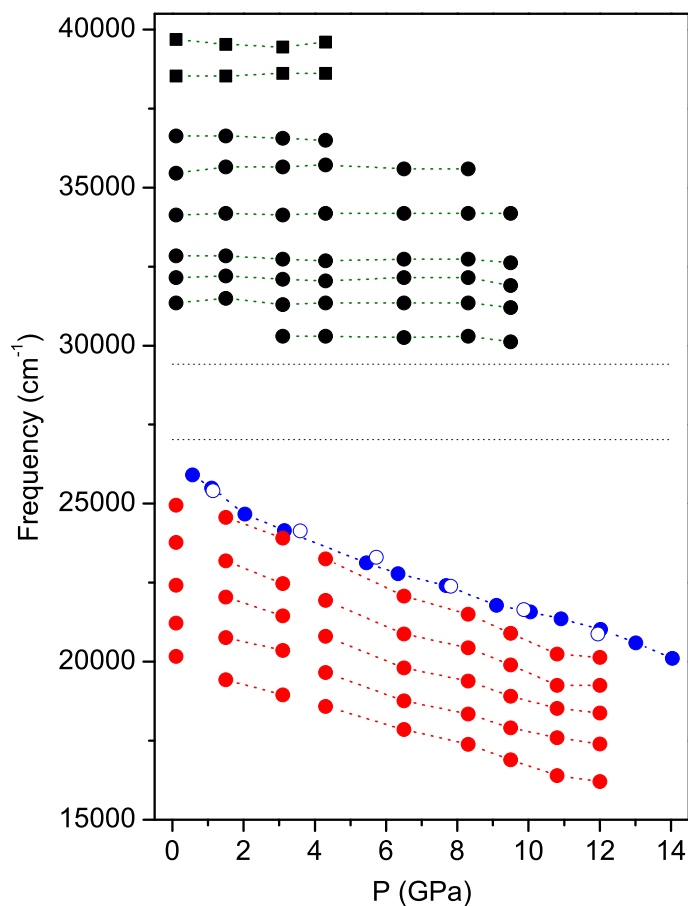


**Figure 1.35:** Central frequency reported as a function of pressure for the two photon excitation profile (black dots) and fluorescence spectra (red dots) superimposed to the optical band gap frequency obtained by one-photon absorption (blue dots, empty ones in decompression).

sorption. Above 9 GPa, one photon induced fluorescence was used for the characterisation, because the overlap of the fluorescence spectrum with the two photon exciting wavelengths prevented the complete analysis of the emission spectrum. The two set of data obtained by the two excitation mechanisms are however superimposable at the same pressure. Because of a limitation of our laser source we measured the two photon excitation profiles only for wavelength shorter than 680 nm, losing all the information about the first electronic transition. The first observed band centred at 638 nm, is in fact re-

lated to the  $S_0 \rightarrow S_2$  electronic transition. Examples of deconvolution made by Voigt profiles as a function of pressure are reported in figure 1.36 and the peak frequencies are reported in figure 1.35. A well defined vibronic structure is observed, for all transitions to  $S_2$ ,  $S_3$  and  $S_4$  states [75]. Despite the strong pressure dependence of the first electronic transition  $S_0 \rightarrow S_1$ , observed by the fluorescence analysis and by direct UV-visible absorption, these structures are not appreciably shifted by pressure as can be noted in figure 1.36, meaning that the compressibility of the higher energy electronic states is almost negligible, and conversely to the  $S_1$  they are not stabilised by the increased density. This is again consistent with the  $^1L_a$  nature of the first electronic excited state in crystalline picene. As reported in figure 1.34 a steep increase of the intensity is observed on the blue side of the excitation profile, whose edge undergoes to a remarkable red shift on rising pressure. The linear dependence of the intensity on the exciting radiation power indicates that it is the one photon absorption edge. The frequency at which the power dependence changes from quadratic to linear has the same pressure evolution as the estimated optical band-gap evolution. Moreover, both estimates of the optical band gap are in perfect superposition with the 0–0 fluorescence band in the whole pressure range. This fact is of particular interest because in general the pressure shift observed in the emission is more pronounced with respect to that observed in absorption [20, 82] because of the different compressibility of the ground and the excited states due to different equilibrium geometries<sup>¶</sup>. This suggests that in the case of picene the optical excitation does not affect the molecular geometry, and the equilibrium geometry of the ground and the first electronic excited states must be quite similar. When picene is compressed up to 10.8 GPa the vibronic structure is lost, and the original spectrum is not recovered in decompression. This is an indication of an occurred chemical reaction as also observed in the UV-visible absorption. The reaction prevents the attain-

---

<sup>¶</sup> When the relaxed geometry of the excited molecule differs from that of the ground states it is subjected to a perturbation from the surrounding. The larger pressure stabilisation of the “relaxed” excited state induces a shift between the absorption and emission origins and a larger pressure shift of the emission compared to the absorption. This effect is enhanced by the increased density

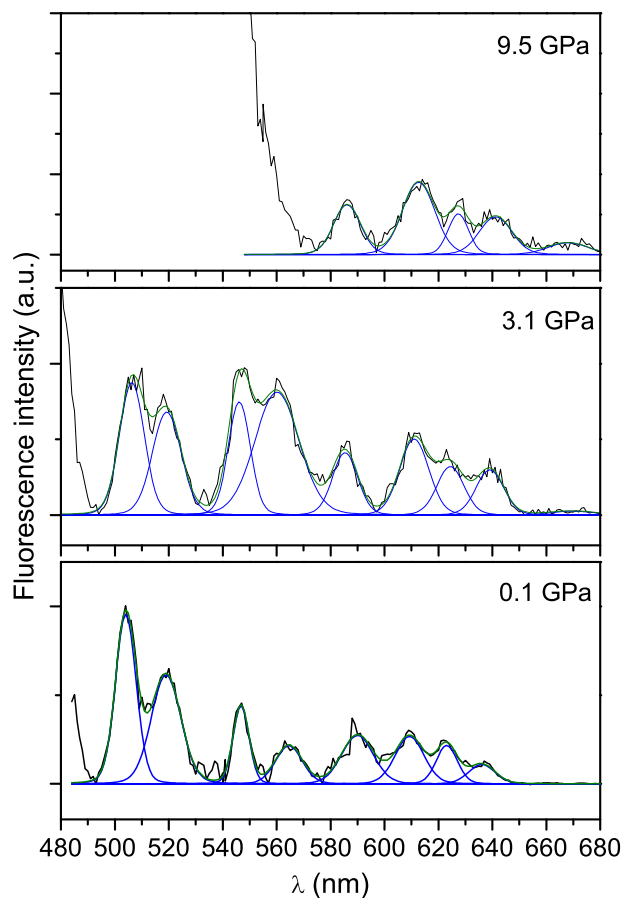


**Figure 1.36:** Deconvolution of the two photon excitation profiles made by Voigt profiles as a function of pressure for the polycrystalline picene.

ment of an eventual gap closure and consequent metallisation of picene that, by extrapolating the behaviour of the band gap as a function of pressure, is estimated to occur at about 64 GPa. No spectral evidence of the formation of excimeric species was observed, as expected from the molecular arrangement in the crystal structure, preventing the formation of structural excimers [80].

### 1.4.3 Chemical reactivity

The irreversible modifications observed in the optical absorption and in the fluorescence properties occurring by compressing above  $\sim 11$  GPa, were carefully analysed by FT-IR spectroscopy and definitely ascribed to a chemical re-

action. The infrared spectrum of fresh loaded picene is in perfect agreement with the literature data [78, 79]. On rising pressure, a continuous blue shift of all bands is observed with slopes of about  $1-2.5\text{ cm}^{-1}/\text{GPa}$  and no discontinuity neither in the frequency nor in the number of components, was observed, suggesting that no phase transition occurs up to the reaction threshold pressure. Upon microscope observation, all samples became orange for pressure of about 9 GPa and increasingly red for further compression as confirmed by UV-visible spectroscopy. The coloration is only partially reversible in decompression if the sample is not compressed up to the bulk reaction threshold pressure. Indeed, when the polycrystalline sample is compressed up to 16 GPa and then decompressed, the IR spectrum is perfectly reversible except for a slightly broadening of the bands due to a residual strain, and pristine picene is recovered without any sign of bulk reactivity. This evidence in addition to that observed in the UV-visible experiments, suggest a reactivity limited at crystal defects in this range of pressure. Instead, upon compression up to  $\sim 23.5\text{ GPa}$ , that is a reproducible value within several experiments, a bulk reaction starts as evidenced by the appearance of a broad band centred at  $\sim 3000\text{ cm}^{-1}$  due to C–H stretching involving saturated carbons, and further increasing in intensity for further compression (figure 1.37). The existence of a reproducible reaction threshold pressure could indicate a possible cooperative mechanism involved in the triggering and propagation of the reaction, possibly driven by the intermolecular contacts in the crystal as evidenced in benzene. The bulk reaction, once triggered, extends in decompression but not to the whole crystal as unreacted picene is always recovered. The higher is the pressure reached upon compression, the larger is the amount of reacted picene at the end of the experiment. Using the integrated absorbance of an isolated picene band it can be estimated that upon compression just above the reaction threshold pressure of 23.5 GPa the total amount of recovered picene at ambient condition is about 35%, while after compression up to 45 GPa it is less than 10%. Indeed, the crystal structure of picene doesn't allow the formation of structural excimers, as the equivalent molecules are too far, whereas

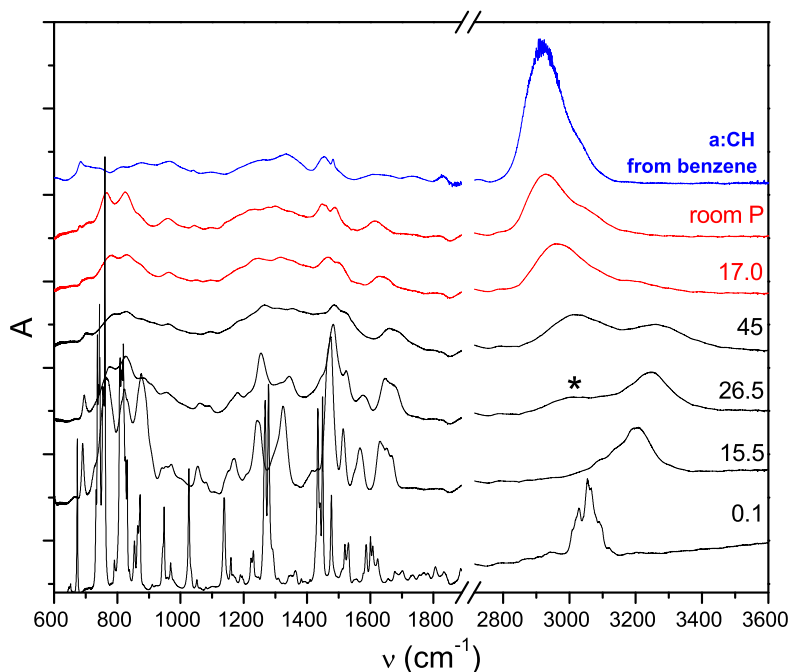


**Figure 1.37:** FT-IR spectra in compression and decompression cycle of polycrystalline picene and of the high pressure reaction product recovered at room conditions compared with the one of benzene [22] (blue line). The pressure values are in GPa.

unequivalent molecules within the unit cell are not in the correct configuration [80]. According to that, the reaction cannot extend to the whole crystal through the lattice modes as in the case of benzene, and the reaction proceeds from the generated seeds only for a limited extent, as confirmed by the unreacted picene always recovered at ambient pressure. The recovered product is disordered and very similar to the  $\alpha$ :CH obtained from the high pressure reaction of benzene. In addition to the aforementioned C–H stretching bands, we can observe infrared absorption in the 700–1000  $\text{cm}^{-1}$  region assigned to CH and  $\text{CH}_2$  bending modes, in the 1130–1530  $\text{cm}^{-1}$  region assigned to C–C stretching, and  $\text{CH}_2$  bending and C=C stretching at 1615  $\text{cm}^{-1}$  [19]. The ratio of saturated to unsaturated carbon can be calculated by analysing the stretching region band structure[19]. The product obtained from the reaction of pi-



cene is characterised by a  $sp^3/sp^2$  ratio of about 1.3, thus containing larger amounts of unsaturated carbon with respect to the product obtained from benzene in similar condition, whose  $sp^3/sp^2$  ratio is 3.2 [19] reflecting the different hydrogen content of the two reactants.

#### 1.4.4 Summary

The electronic properties of picene were studied in two solutions of different polarity and in the  $P2_1$  monoclinic crystal at ambient conditions by means of one and two photon induced fluorescence and by UV-visible spectroscopy. The pressure evolution of the electronic states was also studied in the crystal as a function of pressure up to the chemical reaction threshold pressure. The UV-visible absorption spectra of picene solution in the 240–380 nm region can be attributed to the four HOMO-LUMO transitions of the isolated molecule. The excited electronic states involved in the transition can be named in the Platt's notation as  $L_a$ ,  $L_b$ ,  $B_a$ ,  $B_b$ . By the analysis of the solvatochromic effect in solvent of different polarities, of the vibronic structure, and of the relative cross sections we were able to determine the energy sequence of the excited electronic states of the single molecule, being:  $^1L_b$  ( $S_1$ ),  $^1L_a$  ( $S_2$ ),  $^1B_a$  ( $S_3$ ),  $^1B_b$  ( $S_4$ ). We were also able to provide an accurate assignment of the vibronic structure in both absorption and fluorescence spectra. Upon crystallisation, both absorption and fluorescence undergo a red shift with respect to the solution, and the molecular character is still maintained. The observed steep increase of the transition moment in the 340–380 nm region compared to shorter wavelengths in the crystal can be attributed to an effect of the crystal field. In particular we hypothesise that nearest molecules can interact through a coupling between  $L_a$  states, forming an upper and a lower energy states, resulting in an enhancement of the dipole transition moment in the spectral region of  $S_1$ . Upon compression we observed a large linear decrease ( $\sim 400\text{ cm}^{-1}/\text{GPa}$ ) of the frequency of the optical gap ( $S_0 \rightarrow S_1$ ) as a function of pressure, whereas the energy of all the observed higher energy transitions is almost unaffected by the increased density. This means that only  $S_1$  is stabil-

ised by the increased density, probably because of a larger polarisability. In spite of an elevated pressure dependence of the optical band gap frequency, picene cannot metallise upon compression. In fact, the optical band gap closure is extrapolated to be at about 64 GPa, a pressure higher than the spontaneous reaction threshold that is found to be 23.5 GPa. Once the reaction is triggered it extends only to limited regions around the reaction seeds and not to the whole crystal, likely because the arrangement in the crystal structure is such that molecules in the relative position required for a chain reaction driven by lattice modes are too far for an efficient reactivity. For the same reason the formation of structural excimers is not allowed. Indeed no signature of excimers is observed by fluorescence measurements. The recovered product presents all the IR spectral features of the *a*:CH obtained for compression of benzene crystal, but richer in unsaturated carbons as expected by its lower hydrogen content.

## Two photon induced reactivity of simple R-OH molecules

### 2.1 Electronic properties of R-OH

As shown in the previous chapters, the pressure threshold of the chemical reactivity can be lowered for several pure compounds, as in the case of aromatics, by means of a suitable photoactivation, that can be efficiently achieved and controlled using two photon excitation. In fact, two photon excitation is non destructive for the sample due to the small cross section, and in addition, for several simple molecules, it falls at longer wavelength than the diamond absorption edge, avoiding possible anvil damages. However many simple molecular systems are not reactive at high pressure and no suitable photochemical process can be useful to induce reactivity. In these cases an optical initiator can be introduced within the sample, that can be used also as a reactant. Indeed, an interesting reactivity can be triggered in mixtures with molecular species that can be properly activated by optical excitation in pressure and temperature conditions in which the mixture is otherwise stable. It has been found that simple R-OH molecules such as water [16, 17] and simple alcohols [83] are able to act as initiators under moderate pressures. The prospect of using simple, inexpensive and environmental friendly materials as optical initiators and reactants at the same time, for the high pressure syntheses of

valuable products is an important step in the achievement of a green chemistry. The first excited electronic states of water, methanol and ethanol [84–86] have dissociative character and can be efficiently populated by two photon absorption of near UV light [87]. The dissociation generates reactive radicals that can trigger chemical reactions in the host material, benefiting of the high density conditions at high pressure. As a matter of facts the efficiency of these processes is intimately connected to the dissociative nature of the electronic states and the reactivity observed in several pure R–OH as a function of pressure has to be correlated to the pressure effect on the electronic structure.

Water is the simplest member of the R–OH family that can be employed in the photoactivated reactions. The electronic absorption of liquid water lies in the vacuum-UV for wavelength shorter than 200 nm [87]. The first absorption band of water is centred at  $\sim 166$  nm corresponding to the  $(1b_1) : \tilde{X}^1A_1 \rightarrow \tilde{A}^1B_1 : (4a_1)$  transition. The final state is dissociative, resulting in the homolytic splitting of the HO–H bond [88]:



It is clear that the electronic excitation of water generates very aggressive radicals that are capable of inducing reactivity in a host material. Similar conclusions can be drawn for the other simplest members of the R–OH family, such as methanol and ethanol, whose electronic absorption spectra are similar and both present excited electronic states of dissociative character [89]. However, the complexity of these two molecules, which are not symmetric like water, opens different dissociation channels. For example computational studies on the electronic excited state surfaces of methanol [86] show that the only electronic state which character is dissociative is the  $S_1$  ( $1A''$ ) state, and it is dissociative only along the  $CH_3O-H$  coordinate, while it is weakly bonding along the  $CH_3-OH$  coordinate. This implies that the main dissociation channel for both alcohols is the homolytic splitting of the O–H bonds which brings the formation of ethoxy or methoxy radicals and an hydrogen atom, while the formation of hydroxyl radical is a minor, but rather important dis-

sociation channel [84, 85]. Within this framework we investigated the effect of pressure on the photoinduced reactivity of simple alcohols, trying to elucidate the effect on the electronic structure of these molecules in an indirect way, also taking advantage by isotopic substitution [90–92].

## 2.2 Ethanol

The reactivity of the fully hydrogenated ethanol molecule was compared to the reactivity of one isotopomer in which the oxydrilic hydrogen is substituted with a deuterium atom (EtOD), at room temperature and at different pressures [90,91] in order to elucidate some aspects of the reaction mechanisms, namely how the O–H cleavage is involved in the photochemical process and how it is modified by pressure.

Both liquid ethanol isotopomers are chemically stable in the whole pressure range investigated, from the ambient value up to the melting at  $\sim 1.7$  GPa and no photoinduced reactivity is observed when irradiated using a high power (0.5 W) of laser wavelength equal or longer than 458 nm. On the other hand, a rich photoinduced reactivity is observed when ethanol is irradiated with  $\sim 0.1$  W of the 350 nm Ar<sup>+</sup> laser line. This wavelength is two-photon resonant with the S<sub>1</sub> state of the molecule, which has dissociative character as discussed in the previous section. The chemistry and the products obtained are highly dependent on the pressure conditions at which the irradiation is performed, and the comparison between the different reactivity observed for the two isotopomers led us to draw important conclusions about the effect of pressure on the first electronic excited state energy surface of the molecule [91].

### 2.2.1 Photoinduced reactivity of fully hydrogenated ethanol

At the lowest pressure of our experiment, that can be estimated in about 5-10 MPa, the main product of the two photon induced reaction is molecular hydrogen. After few hours of irradiation, gaseous bubbles appear in the sample

whose composition is estimated to be for the major part hydrogen and impurities of ethane and methane (figure 2.1 ) as can be revealed by Raman spectroscopy [90].

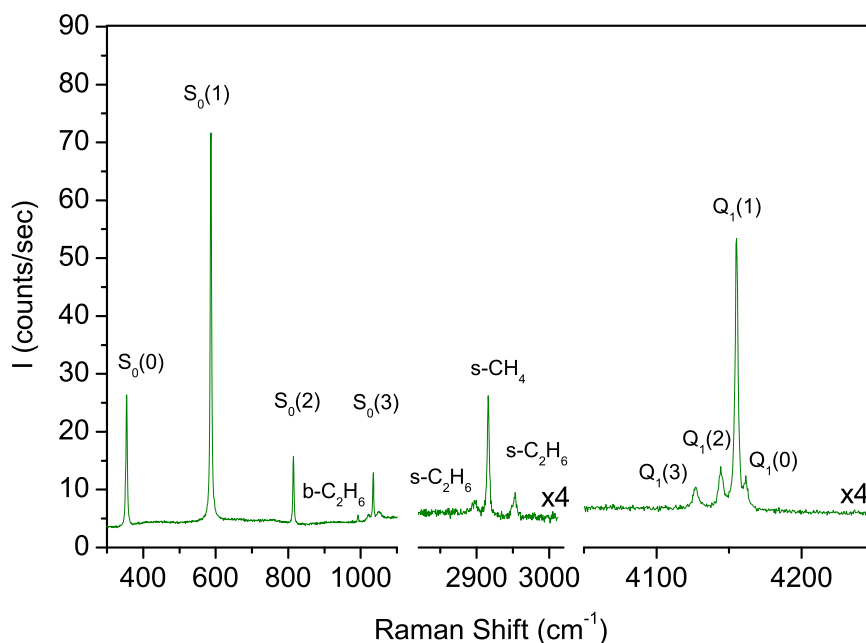


**Figure 2.1:** Raman spectra performed in the gaseous bubble formed in the ethanol sample after 5 h of irradiation with the  $\text{Ar}^+$  laser line at 350 nm (0.26 mW), at a pressure estimated of about 7 MPa. The more intense bands labelled as  $S_0(i)$  are the rotational lines of molecular hydrogen, while the  $Q_1(i)$  are the rotovibrational modes. In addition the bending (*b*-) of ethane and the stretching (*s*-) of ethane and methane are also observed.

In the liquid region surrounding the bubbles, no bands but that of ethanol are revealed by Raman spectroscopy. By FT-IR spectroscopy, that is sensitive to concentrations in the ppm range, several products bands can be identified as shown in figure 2.2.

To identify the products and the different reaction channels we performed irradiation cycles of few hours each for a total duration of about 20 h, with constant irradiation power. FT-IR and Raman spectra were recorded after each irradiation step, for three different pressures (0.5, 1.0 and 1.5 GPa), starting on a fresh sample for every investigated pressure. Examples of infrared spectra and

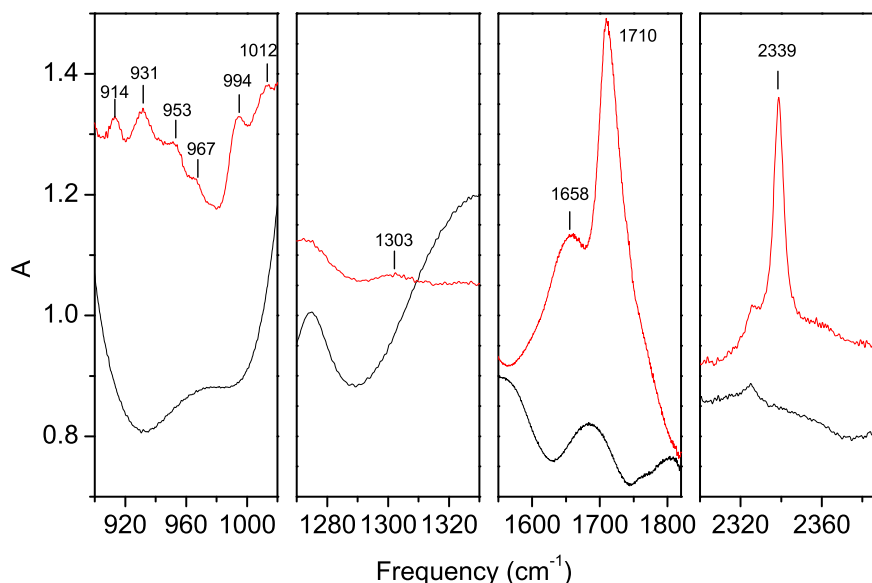


**Figure 2.2:** Infrared spectra performed in the ethanol sample after 5 h of irradiation with the  $\text{Ar}^+$  laser line at 350 nm (0.26 mW), at a pressure estimated of about 7 MPa. The spectra of pure ethanol (black trace) is reported for a better comparison.

the time evolution of the product band integrated areas at 1.0 GPa are reported in figure 2.3. Different product bands show different behaviour as a function of irradiation time, being also different compared to the consumption rate of ethanol itself, from which clearly appears that several reaction paths exist. By a careful analysis of the spectral evolution as a function of time for each pressure, we identified groups of bands having similar behaviour as a function of pressure and irradiation time, thus supporting the assignment of these bands to different products and remarking the important role of pressure in selecting among different reaction paths [90]. The identification of some products, like  $\text{H}_2$ ,  $\text{CO}_2$ ,  $\text{CH}_4$  and  $\text{H}_2\text{O}$  is straightforward, for the other bands a proposed assignment [90] is reported in tables 2.1 and 2.2.

In spite of the complexity of the whole spectral information, from these results appears that the best agreement of frequency and relative intensities of both Raman and IR spectra recorded at the three different pressure values,

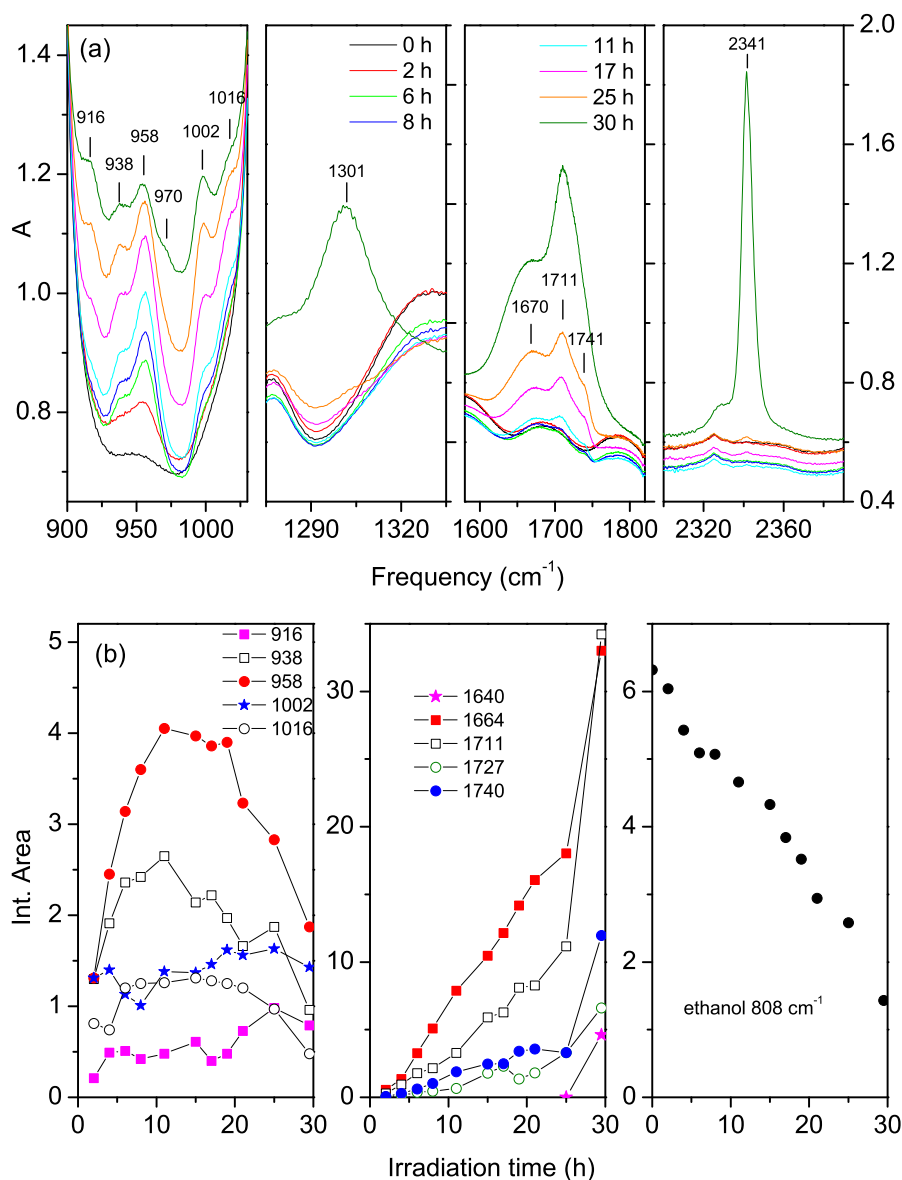


**Figure 2.3:** a) Evolution of the infrared spectra as a function of irradiation time (350 nm, 0.26 mW), at the pressure 1.0 GPa. b) Evolution of the integrated area for some selected bands.

is given only by three relatively simple molecules (2-butanol, 2,3-butanediol, 1,1-dietoxiethane) in addition to some decomposition products and the aforementioned compounds. Three groups of reaction were identified, and the relative weight of the several reactive paths depends both on pressure and irradiation time. The reactions of the first group are those that are initiated by



	ambient	0.007 GPa	0.5 GPa	1.0 GPa	1.5 GPa
ethane	822 <sup>a</sup>	822	822	826	828
methane	1306 <sup>a</sup>	1303	1303	1301	1298 <sup>c</sup>
2-buthanol	914 <sup>a</sup>	914	914	916	919
	968 <sup>a</sup>	967	968	970	
	992 <sup>a</sup>	994	994	1002	999
2,3-buthanediol	929 <sup>a</sup>	931	933	938	
	1011 <sup>a</sup>	1012	1010	1016	
1,1-diethoxyethane	953 <sup>a</sup>	953	958	957	957
acetone	1712 <sup>a</sup>	1710	1710	1711	1715 <sup>c</sup>
acetaldehyde	1727 <sup>b</sup>		1725	1728	
ethyl acetate	1742 <sup>a</sup>	1740	1742	1741	

**Table 2.1:** IR peak frequencies ( $\text{cm}^{-1}$ ) of the products bands and their assignment according to literature data. <sup>a</sup> ref.[93]; <sup>b</sup> liquid film; <sup>c</sup> estimated value from the saturating peak.

	ambient	0.007 GPa	0.5 GPa	1.0 GPa	1.5 GPa
hydrogen	354 <sup>a</sup>	354	355		
	587 <sup>a</sup>	586	590		
	814 <sup>a</sup>	814			
	1034 <sup>a</sup>	1033			
	4126 <sup>b</sup>	4127			
	4143 <sup>b</sup>	4143	4144		
	4155 <sup>b</sup>	4155			
	4161 <sup>b</sup>	4161			
ethane	995 <sup>c</sup>	993	996	1001	1004
	2896 <sup>d</sup>	2897			
	2954 <sup>c</sup>	2953			
methane	2917 <sup>e</sup>	2916	2911		2924 <sup>f</sup>
2-buthanol	502 <sup>d</sup>		504	506	
	776 <sup>d</sup>		777	783	
	819 <sup>d</sup>	819	822	823	
	914 <sup>d</sup>		915		
2,3-buthanediol	525 <sup>d</sup>		524		
	549 <sup>d</sup>		551	553	
	929 <sup>d</sup>		933	935	
1,1-diethoxyethane	529 <sup>d</sup>			532	
	808 <sup>d</sup>			810	

**Table 2.2:** Raman peak frequencies ( $\text{cm}^{-1}$ ) of the products bands and their assignment according to literature data: <sup>a</sup> ref.[94]; <sup>b</sup> ref.[95]; <sup>c</sup> ref.[96]; <sup>d</sup> ref.[93]; <sup>e</sup> ref.[97]; <sup>f</sup> here methane is crystalline ref.[98].

radical species in the first hours of irradiation, leading to products like  $\text{H}_2$ , ethane, 2-butanol, 2,3-butanediol and 1,1-diethoxyethane. The second group is related to the disproportion reactions occurring for longer irradiation times when the amount of ethanol is limited in the reaction volume, leading to  $\text{CH}_4$  and  $\text{CO}_2$ . The third group is related to formation of water and carbonic com-

pounds, continuously increasing with irradiation time. The observed behaviour suggests a radical initiated chemistry in which the first products undergo further transformations. Hydrogen formation is one of the main channels at ambient pressure, and its production is highly inhibited by pressure, being still detectable at 0.5 GPa and not present at all for  $P > 1.0$  GPa. As molecular hydrogen is demonstrated to mainly derive from the dissociation of the EtO–H bond [99], this is an indication that at least at ambient pressure the dissociation along this coordinate is the main photodissociation channel as already shown in the gas phase, while at higher pressure other channels possibly open or become more efficient.

The whole set of data can be used to draw a fundamental conclusion about the photochemistry of liquid ethanol in high pressure conditions. In fact, in the whole pressure range all the observed product can be justified taking into account only the following two out of four energetically similar photodissociation processes already reported for the gas phase [85]:



Ethane, that possibly derives from hydrogenation of the ethyl radical generated through the path 2.2, is barely detectable at the lowest pressure while it is one of the major products at higher pressures confirming that the reaction channel 2.1 gains relative importance with respect to the 2.2, whereas the global rate of consumption of ethanol is slowed down by the increasing density (figure 2.6). The formation of both 2-butanol and 2,3-butanediol likely derives from the radical in which the spare electron is localised in the  $\alpha$ C ( $CH_3\dot{C}HOH$ ). The latter radical can be formed directly by photodissociation of an excited ethanol molecule, or by rearrangement of the radical formed in the reaction 2.1, being its more stable form and considering the high mobility of the oxydrilic hydrogen. The formation of the 1,1-diethoxyethane can derive from both radicals formed in 2.1 and 2.2, through reaction with two

other ethanol molecules and its yield increases on rising pressure because of the high molecularity of the reaction. The formation of 1,1–diethoxyethane is competitive with that of the superior alcohols, as they are barely detectable at the highest pressure when the largest amount of 1,1–diethoxyethane is evidenced, suggesting that the  $\alpha$ C radical from which the superior alcohols derive arises from the rearrangement of the ethoxy radical produced in the dissociation process 2.1. Thus the increased density has the effect of inhibiting the rearrangements of the aforementioned radicals because of a shortening of the free mean path of the radicals themselves and favouring the reaction with higher molecularity. The reduction of the global consumption rate of ethanol at the higher pressures is not obvious and can be explained making a comparison with the ethanol isotopomer in which the oxydrilic hydrogen is replaced by a deuterium, as explained in the next section.

### 2.2.2 Isotopically marked ethanol: enlightening the effect of pressure on the excited electronic states

A comparison between the photoinduced reactivity at high pressure of fully hydrogenated ethanol and of the isotopomer in which the oxydrilic hydrogen is substituted by a deuterium, can provide fundamental information about the mechanisms ruling the photodissociation of the simplest R–OH systems, and on how the excited electronic surfaces of these molecules are affected by the pressure [91].

The photoinduced reaction was conducted in EtOD in the same conditions already discussed for the fully hydrogenated ethanol in section 2.2.1. In figure 2.4 are reported the FT–IR spectra at different irradiation times using  $\sim 0.26$  W of the laser emission of a continuous wave Ar<sup>+</sup> laser peaked at 350 nm, from which the spectrum of the unreacted sample was subtracted. The main spectral features, except for the bands around 1700 cm<sup>-1</sup>, are related to the formation of fully hydrogenated ethanol, clear evidence of the dissociation along the O–D coordinate, already identified to be the main dissociation

channel in ethanol. A fit performed in the 900-1050  $\text{cm}^{-1}$  region unveils the presence of the already observed bands that can be attributed to the same products obtained from fully hydrogenated ethanol and reported in table 2.1, that in the same way intensify linearly in the first 10 hours of irradiation time (figure 2.5). In conclusion the photoinduced reactivity of EtOH and EtOD is almost identical at the pressure of 0.5 GPa.

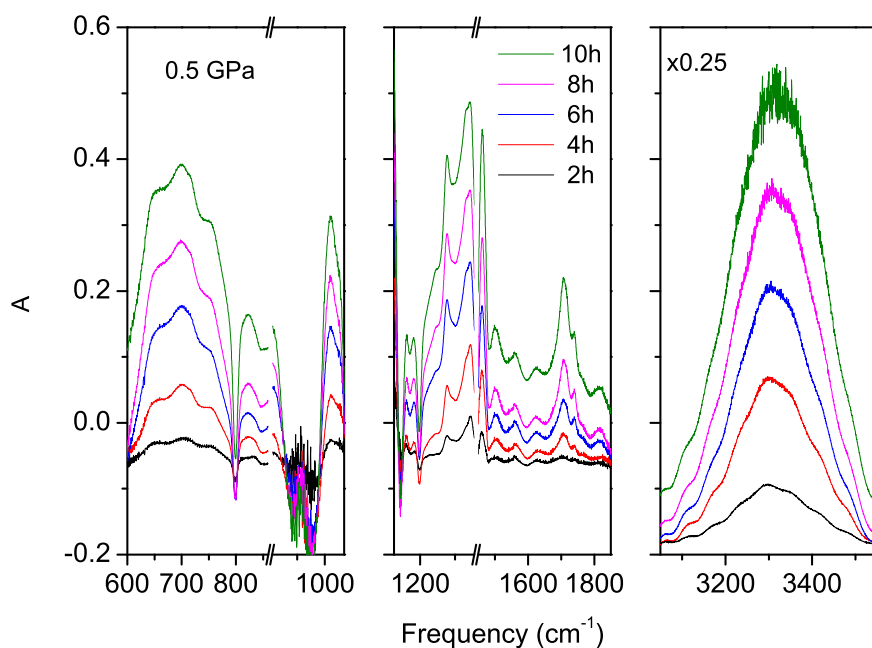


**Figure 2.4:** Differential FT-IR spectra measured as a function of irradiation time ( $\sim 0.26$  W at 350 nm), in the EtOD at 0.5 GPa

Conversely, the irradiation performed in the same conditions at 1.0 GPa induces only a reactivity that is barely observable in the deuterated ethanol, while it was remarkable in the fully hydrogenated isotopomer [91]. In figure 2.6 the amount of ethanol transformed as a function of the irradiation time is reported. Indeed, the consumption rate at 1.0 GPa is  $\sim 70\%$  of that at 0.5 GPa for the hydrogenated isotopomer, while it is  $\sim 13\%$  for the deuterated isotopomer. This is a sharp indication that the reduction of the reactivity has to be mostly related to the efficiency of dissociation along the O–H coordinate, the only one of interest for the isotopic substitution. Indeed, the deuterium sub-

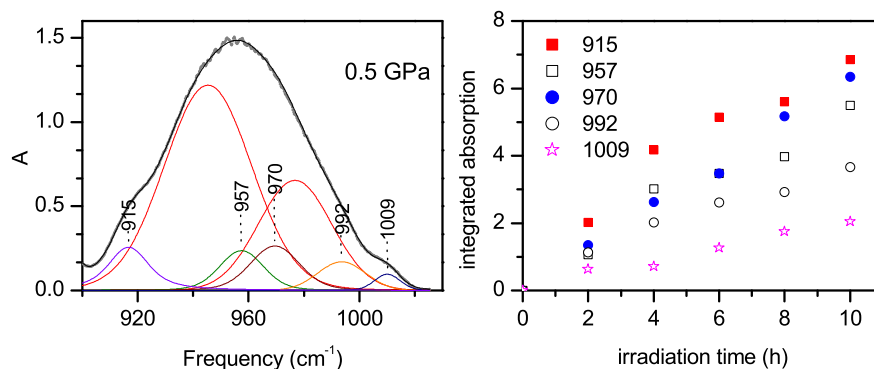


**Figure 2.5:** Fit of the FT-IR spectra after 10 h of irradiation ( $\sim 0.26$  W at 350 nm) of EtOD at 0.5 GPa, in the 900-1050 cm<sup>-1</sup> region made by Voigt profiles (upper panel), and evolution of the integrated area of the product bands (lower panel)

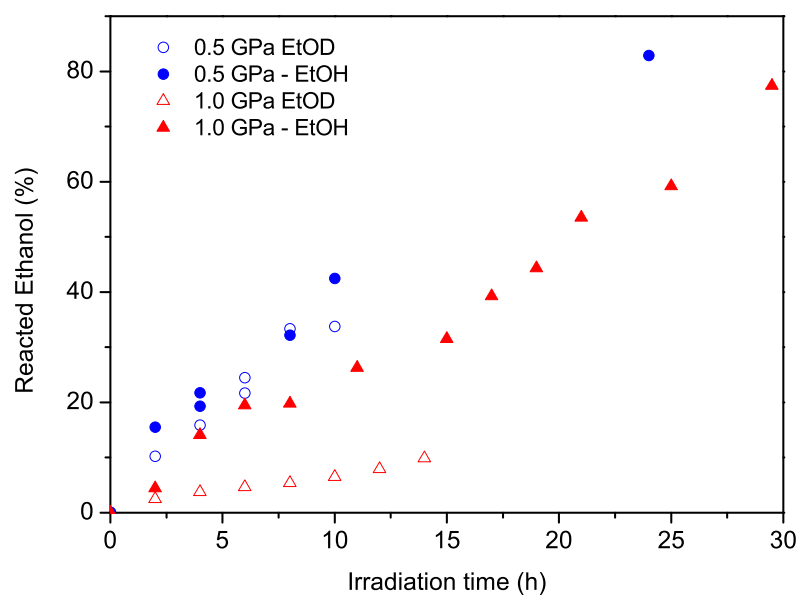


**Figure 2.6:** Transformed amount of the two ethanol isotopomers as a function of the irradiation time at 0.5 and 1.0 GPa. The amount of reacted ethanol is calculated evaluating the integrated area of the  $\nu_9$  bending mode laying at 800 cm<sup>-1</sup> for EtOD and 806 cm<sup>-1</sup> for EtOH (frequency values at 0.5 GPa)

stitution can provide information about the involvement of the dissociation along the marked bond in the rate limiting step of the reaction, through the

kinetic isotopic effect (KIE) [100].

At 0.5 GPa, the reaction rates of both isotopomers are almost identical, meaning that the rate limiting step of the photoinduced reaction is one of the steps of the radical reaction following the dissociation itself. Indeed, at 1.0 GPa an abrupt reduction of the reactivity is observed for the deuterated ethanol, whose consumption rate is reduced by a factor of  $\sim 5 - 6$  compared to the fully hydrogenated isotopomer. This is the typical value expected for a H/D primary kinetic isotopic effect\*, and it indicates that the O–H bond breaking is involved in the rate-limiting step of the reaction at high pressure. This effect can be explained hypothesising a significant modification of the excited electronic energy surface at least along the O–H coordinate, that reduces the dissociative character up to become weakly bonding [91]. A sketch of this change induced by pressure is reported in figure 2.7. The different vibrational energy content at the zero-point that is lower in presence of the deuterium, allows the minimum of energy that is formed by pressure to be better appreciated.

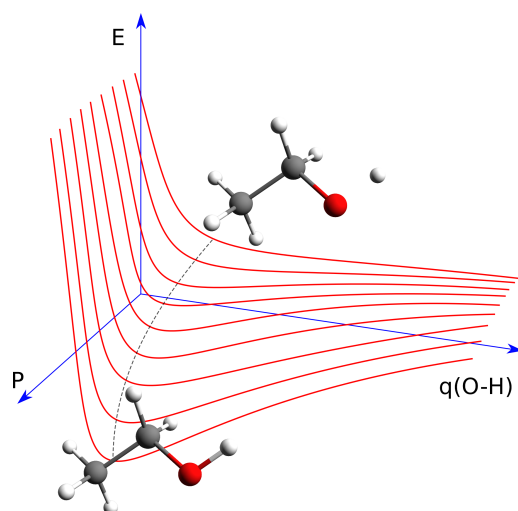


**Figure 2.7:** Schematic representation of the pressure effect on the potential energy surface of the lowest electronic excited state of ethanol reported along the O–H coordinate: starting from the non-bonding character of the excited electronic state at ambient pressure, an energy minimum is created and deepened by the pressure.

\* a primary KIE is observed when the bonds that is cleft in the transition state of the rate-limiting step of the reaction is directly involved in the isotopic substitution.

## 2.3 Methanol

The photoinduced reactivity of liquid methanol ( $\text{CH}_3\text{OH}$ ) was studied at ambient temperature as a function of pressure in comparison with that of one deuterated isotopomer ( $\text{CD}_3\text{OH}$ ) for a twofold purpose. The first aim was the evaluation of the relative importance, for the high pressure photoinduced reactivity, of the photodissociation path involving the direct cleavage of the C–H bond on the side chain, demonstrated to be one of the main dissociative channels in the ground state thermally induced reaction [101], but not shown to be of any relevance in the gas phase photodissociation [84]. The second issue is related to the claimed radical rearrangement process following the OH cleavage, leading in the ethanol case to the formation of 2-butanol and 2,3-butanediol (see section 2.2.1), which should be less important for methanol because of the minor stabilisation of the rearranged radical expected for a primary carbon [92].

### 2.3.1 Photoinduced reactivity and product identification

Methanol is chemically stable in the whole tested pressure range, up to the melting pressure, that is about 3.5 GPa at room temperature for the fully hydrogenated isotopomer [102]. Both the analysed isotopomers ( $\text{CH}_3\text{OH}$  and  $\text{CD}_3\text{OH}$ ) present similar UV absorption spectra [86]. Their first electronic excited states lie under  $\sim 180$  nm, and can be populated by two photon absorption as in the case of ethanol, resulting in aggressive radical species because of its dissociative character. The photoinduced reactions were performed using  $\sim 0.4$  W of the emission of continuous wave  $\text{Ar}^+$  laser, centred at 350 nm, at pressures ranging from 0.1 up to 1.8 GPa. The reactivity observed for the methanol case was always lesser than the one reported for ethanol, as longer irradiation time were necessary to observe detectable product bands. In the attempt to gain evidence for the products absorption we calculated the difference FT-IR spectra, by subtracting from the spectrum recorded after each irradiation cycle the spectrum measured at the same pressure before irradiat-

ing the sample. These spectra for  $\text{CH}_3\text{OH}$  at 0.3 and 1.2 GPa, as a function of the irradiation time, are reported in figure 2.8. The difference spectra were fit using Voigt profiles, and the assignment was made [92] considering among the possible products that can derive from the photodissociation of methanol, the ones whose IR bands match both the frequencies and the relative intensities of the experimentally observed ones, reported in table 2.3. As already observed for ethanol, the pressure has a fundamental role in selecting among different reactive channels. The first example is represented by three bands attributed to the ethylene glycol, namely at 866, 887 and  $1091\text{ cm}^{-1}$  (see figure 2.8), that are present in the lower pressure experiments (0.1 and 0.3 GPa) and totally missing for higher pressures up to 1.8 GPa. A confirmation of this assignment is given also by the irradiation of the deuterated methanol, in which the same behaviour is observed, and an ethylene glycol isotopomer ( $\text{HO}(\text{CD}_2)_2\text{OH}$ ) is found only among the photoinduced products obtained at low pressure (0.2 GPa, see table 2.3 and figure 2.9). All the product bands observed in the irradiation of  $\text{CD}_3\text{OH}$  can be assigned by considering the deuterated compounds corresponding to the products identified in the  $\text{CH}_3\text{OH}$  case. All the products observed in the irradiation cycles performed in the whole pressure range investigated, and for both isotopomers, are the same (see table 2.3) with the only exception of the aforementioned ethylene glycol that is observed only at the lower pressures. The two main products formed in the high pressure irradiation (for  $P > 1\text{ GPa}$ ) are the methylformate and the metoxymethanol, the hemiacetalic form of formaldehyde that is stable in excess of methanol [103]. Small quantities of carbonilic and unsaturated compounds are found especially at the higher pressures, the latter being likely responsible of the higher fluorescence of the samples, that prevented an accurate Raman characterisation. Differently from the ethanol case, also at the lowest pressure hydrogen formation is not a main channel, being HD molecule the only hydrogen isotopomers observed (by the Raman band at  $3612\text{ cm}^{-1}$ ) and only in the irradiation of  $\text{CD}_3\text{OH}$  at 0.2 GPa. In addition,  $\text{CD}_3\text{OD}$  is formed in the photodissociation of  $\text{CD}_3\text{OH}$ , and it is detected by the band at about  $2450\text{ cm}^{-1}$  due to the



OD stretching mode (figure 2.9). The formation of CH<sub>4</sub> from CH<sub>3</sub>OH cannot be demonstrated due to the interfering methanol bands that saturate the IR spectrum in the methane spectral region.

	CH <sub>3</sub> OH					CD <sub>3</sub> OH			
	1 bar	0.3 GPa	1.2 GPa	1.8 GPa		1 bar	0.2 GPa	1.0 GPa	1.5 GPa
ethylene glycol	864 <sup>a</sup>	866			HO(CD <sub>2</sub> ) <sub>2</sub> OH	897 <sup>a</sup>	908		
	882 <sup>a</sup>	887				946 <sup>a</sup>	947		
	1084 <sup>a</sup>	1091				1063 <sup>a</sup>	1063		
methoxy methanol	925 <sup>b</sup>	922	925	927	CD <sub>3</sub> OCD <sub>2</sub> OH	1197 <sup>a</sup>	1196		
	1067 <sup>b</sup>		1065			833 <sup>c</sup>	831	834	836
	1123 <sup>b</sup>	1127	1125			1109 <sup>c</sup>	1096	1099	1097
	1200 <sup>b</sup>	1198	1199	1201		1142 <sup>c</sup>	1140	1140	1141
	1303 <sup>b</sup>	1305	1305	1305					
methyl formate	910 <sup>d</sup>	907	911	912	CD <sub>3</sub> OCDO	834 <sup>e</sup>	822	824	826
	1158 <sup>d</sup>	1156	1163			1091 <sup>e</sup>	1090	1090	1091
	1208 <sup>d</sup>	1209	1212	1212		1199 <sup>e</sup>	1200	1195	1198
	1728 <sup>d</sup>	1728	1727	1726		1698 <sup>e</sup>	1693	1693	1693
						1740 <sup>e</sup>	1737	1740	1739
					CD <sub>3</sub> H	1003 <sup>f</sup>	1002		
						1036 <sup>f</sup>	1034	1035	1031

**Table 2.3:** Central peak frequencies (cm<sup>-1</sup>) of the product infrared absorption bands obtained in the photoinduced reaction and reference data. *a*: liquid data.[104]; *b*: our data; *c*: data obtained in Ar matrix at 10 K [105]; *d*: liquid data [93]; *e*: solution data [106]; *f*: gas data [107]

### 2.3.2 Pressure effects on the reaction mechanisms

The evolution of some selected bands was analysed as a function of the irradiation time to estimate the reaction rates (figure 2.10). The rates, expressed as the time derivative of the integrated area, are reported in the table below figure 2.10. Among the product bands, we selected the ones corresponding to pure stretching modes, as C=O stretching for the methylformate and C–O–C stretching for the methoxytmethanol, in such a way that the effect of isotopic substitution on the band intensity can be neglected. The consumption rate of the reactant can be followed only in the case of the CD<sub>3</sub>OH, by the intensity decrease of one in-scale of its infrared bands, namely the band at 887 cm<sup>-1</sup>. In both isotopomers the reaction rates increase as a function of pressure, indicating a greater reactivity due to the shorter intermolecular distances attained

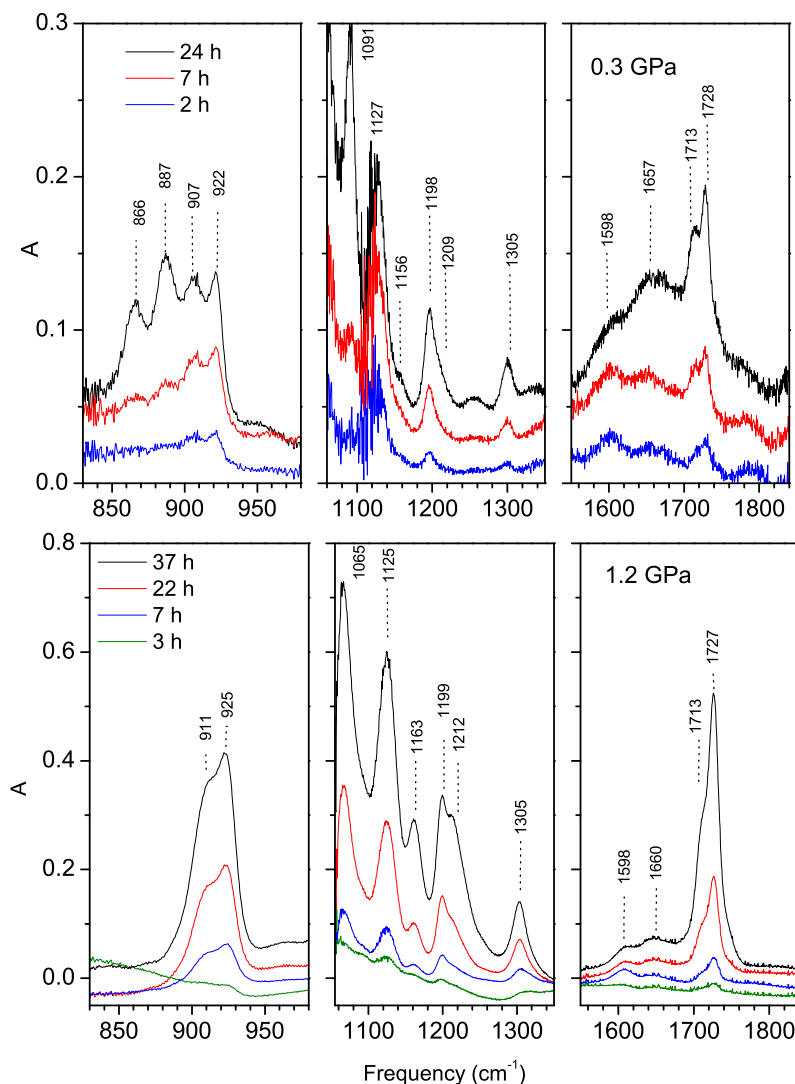


**Figure 2.8:** Difference FT-IR spectra as a function of the irradiation time using  $\sim 0.4$  W of the 350 nm  $\text{Ar}^+$  laser line, for  $\text{CH}_3\text{OH}$  at 0.3 and 1.2 GPa.

at high density enhancing the probabilities of reactive events. A maximum in the reaction rates is observed around 1.0 GPa for  $\text{CD}_3\text{OH}$ , and 1.2 GPa for  $\text{CH}_3\text{OH}$ , whereas further compression determines for both molecules an abrupt decrease of the reactivity, indicating that at least one of the reaction channels is strongly affected by the pressure. On the other hand, the production rate of methane ( $\text{CD}_3\text{H}$ ) is almost insensitive to pressure, being approximately the same in all experiments performed in  $\text{CD}_3\text{OH}$ . This is a clear evidence of

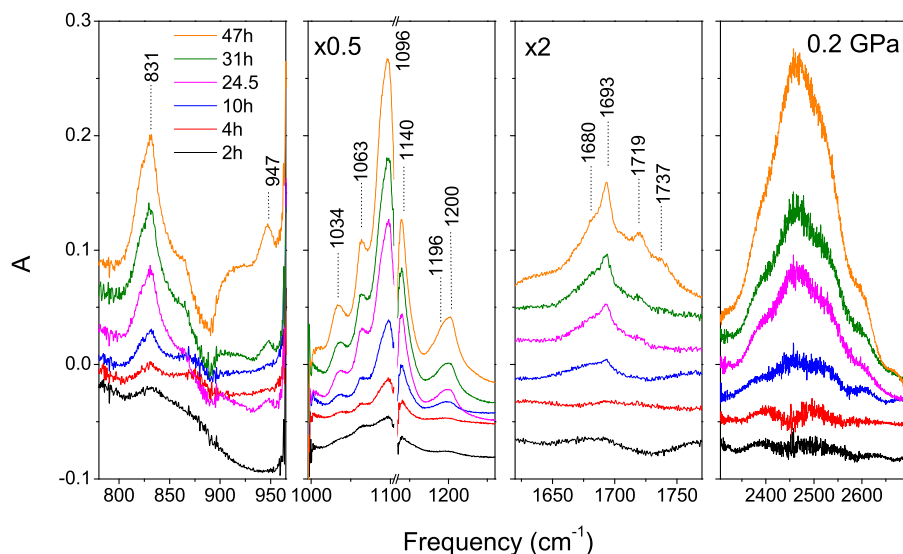
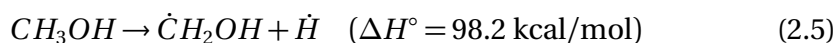
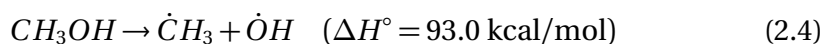
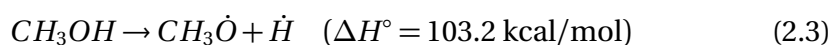
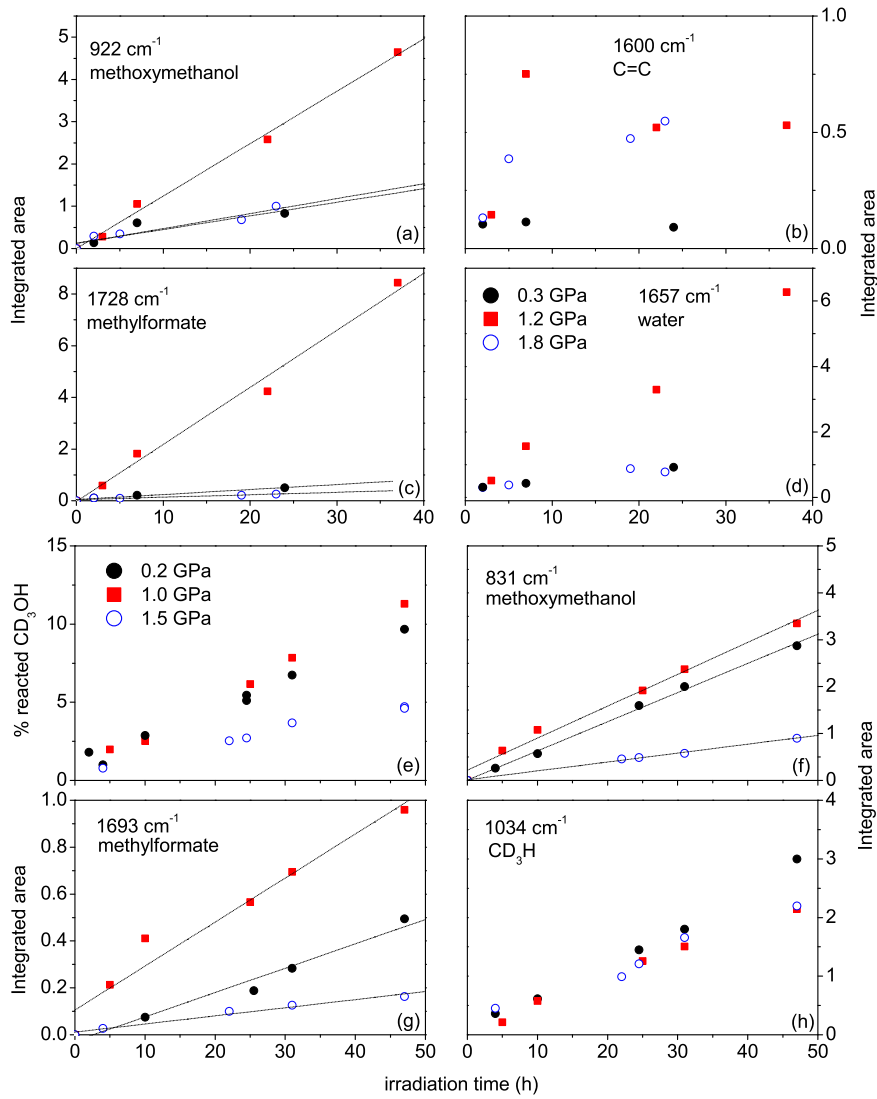


**Figure 2.9:** Difference FT-IR spectra as a function of the irradiation time using  $\sim 0.4$  W of the 350 nm  $\text{Ar}^+$  laser line, for  $\text{CD}_3\text{OH}$  at 0.2 GPa.

the existence of different reaction channels triggered by distinct initial photodissociation events, already observed for ethanol and also reported for the methanol gas phase. The main dissociation channels in the gas phase [84] are reported below:



In the gas phase, the photodissociation channel 2.3, involving the cleavage of the O–H bond, is found to be the main channel following the 193 nm excitation, contributing in about 86% of the whole initiation processes, while the channel 2.5 is almost negligible especially using low irradiation powers [84]. As our irradiations were performed using two photon absorption, this is surely the case, and we can rule out the channel 2.5 for the interpretation of the observed high pressure reactivity. As a confirmation, among all the observed



C-O-C str. methoxymethanol				C=O str. methylformate			
$\text{CH}_3\text{OH}$ (922 $\text{cm}^{-1}$ )		$\text{CD}_3\text{OH}$ (831 $\text{cm}^{-1}$ )		$\text{CH}_3\text{OH}$ (1728 $\text{cm}^{-1}$ )		$\text{CD}_3\text{OH}$ (1693 $\text{cm}^{-1}$ )	
P(GPa)	dA/dt	P(GPa)	dA/dt	P(GPa)	dA/dt	P(GPa)	dA/dt
0.3	0.032	0.2	0.061	0.3	0.019	0.2	0.010
1.2	0.124	1.0	0.068	1.2	0.221	1.0	0.019
1.8	0.035	1.5	0.019	1.8	0.010	1.5	0.002

**Figure 2.10:** Evolution of the integrated area of some products bands as a function of the irradiation time for  $\text{CH}_3\text{OH}$  (a-d frames) and  $\text{CD}_3\text{OH}$  (e-h frames) at three different pressures and slope values obtained by linear fit of selected data [92]

products, only the ethylene glycol could derive from the radicals generated in 2.5, however in this case we should observe in the deuterated methanol irradiation experiments also the products of the other radical generated in 2.5, first of all the  $D_2$  molecule, that conversely it is never observed. Thus the ethylene glycol was more reliably generated according to a two-step mechanism, involving the rearrangement of the methoxy radical generated in 2.3, to the hydroxymethyl radical and subsequent reaction with a methanol molecule. This process is the analogous invoked in the ethanol case to explain the formation of 2-butanol and 2,3-butanediol [90]. In a same way, pressure inhibits the formation of ethylene glycol, as the increased density shortens the free mean path of the radical itself preventing its rearrangement. All the products formation can be then explained, by taking into account only the channel 2.3 and 2.4, while the photodissociation channel 2.5 can be totally neglected. Unsaturated species containing C=C bonds, and methane are possibly generated by the photodissociation channel 2.4. The relatively low amount of such products is justified as the channel 2.4, involving the cleavage of the C–O bonds, is not a main channel as observed in the one-photon induced reaction in gaseous methanol. The production rate of methane ( $CD_3H$ ) is almost constant in the whole range of investigated pressures in contrast with all others products 2.10, meaning that the channel 2.4, from which methane is generated, is almost pressure insensitive. Methoxy methanol, being the formaldehyde hemiacetal equivalent, can form by reaction of the methoxy radical with a methanol molecule, either by elimination of another H atom to form formaldehyde. Formaldehyde itself, in excess of methanol can give the hemiacetal or it can further react giving the methyl formate. A clarification between the two proposed mechanism is given by the comparison between the photoinduced reactivity of the two methanol isotopomers. The formation rate of both methoxymethanol and methyl formate is reduced, for pressures greater than 1 GPa, on going from the hydrogenated to the deuterated isotopomer (figure 2.10) by a factor of about 2 for methoxymethanol and by an order of magnitude for methyl formate. The reduction of the formation rate of one order

of magnitude is a typical value for a primary kinetic isotopic effect, entailing the involvement of the C–H cleavage in the rate determining step of the reaction. This observation supports the formation of methylformate through the rearrangement of the methoxy radical to give formaldehyde [92], that is further oxidised for reaction with another methoxy radical. On the other hand, a reduction in the methoxymethanol formation rate of a value not exceeding 2 is possibly due to the presence of another reaction channel resulting in the same product, consisting in the direct reaction of the methoxy radical with a methanol molecule that does not require the radical rearrangement. However, these consideration cannot explain why the formation of all the products arising from channel 2.3 (cleavage of the O–H bond) is strongly reduced on rising pressure above  $\sim 1$  GPa, whereas the ones deriving from the channel 2.3 (cleavage of the C–O bond) are almost unaffected. As already proposed for the ethanol case [90, 91] and taking in account the similarities between the two molecules, a change in the dissociative character of the excited state of the molecule can give a satisfactory explanation of the observed behaviour also for methanol.

## 2.4 Summary

The two-photon induced reactivity of two ethanol and two methanol isotopomers were analysed and compared as a function of pressure in the gigapascal range for the purpose of better understanding the pressure effect on reaction mechanisms, selectivity and on the excited electronic states involved in the reaction mechanisms of simple R–OH molecules. Exploiting the dissociative character of the first electronic excited state of R–OH, a variegated chemistry initiated by the reactive radicals generated by the light absorption, is observed in the pure systems in the high density conditions typical of the gigapascal pressure range. For both alcohols we evidenced a strong pressure effect on the selectivity among several reactive channels. For both alcohols the main photodissociation channel is found to be the cleavage of the O–H

bond, whose generated radicals are responsible for triggering the reactions leading to the majority of the products, at least at the lower pressures. The other photodissociation channel, that is a minor though important channel, is the cleavage of the C–O bond, giving rise to aggressive radicals that have an important role in the reactivity. All the other dissociation channels found in the irradiation experiments of the methanol and ethanol gas phases, or induced by thermal effect can be confidentially neglected to explain the high pressure photoinduced reactivity for both alcohols. By a careful identification of the products by means of Raman and FT-IR spectroscopy and by an accurate analysis of the formation kinetics of the products and of the consumption rate of the reagents, the relative weight of the different reaction channels and how they are influenced by the increasing pressure were rationalised. The effect of pressure is found to be relevant on the selectivity among the two different photodissociation channels that have been identified. By the comparison of the reactivity of the different isotopomers, taking into account the kinetic isotopic effect, the induced selectivity was explained by a pressure effect on the electronic excited state surface. In particular, the comparative analysis performed on ethanol and methanol isotopomers shows that pressure is able to affect the dissociative character of the first excited electronic state, that is reduced on increasing pressure along the O–H coordinate, as an energy minimum is created and deepened by the increasing pressure.





## Water dynamics by ultrafast transient infrared spectroscopy

As already introduced, information about the pressure effects on fast dynamical processes has been so far prevented by technical limitations. In this chapter the application of an ultra-fast technique, the transient medium-infrared pump-probe spectroscopy, to molecular system in high pressure devices will be presented to show the effect of the pressure on the structure and dynamics of water, that is one of the most studied liquids, but not yet completely understood.

### 3.1 Anomalous behaviours of water

Despite its molecular simplicity, water is a very peculiar substance presenting a remarkably rich phase diagram and still within the liquid phase many thermodynamic properties change as a function of temperature and pressure in very unconventional ways [108]. Being different to most other liquids, called simple liquids, even water density has a non monotonic behaviour as a function of temperature or pressure, determining the well known maximum of density at ambient pressure observed at 4°C [109]. Many theories were developed to the purpose of explaining the water thermodynamic anomalies, that become much more evident in the non-equilibrium regimes such as in undercooled water. For the latter reason most of the studies are dedicated to

investigate this out-of-equilibrium range and most theories are based on observation or calculation performed in the out-of-equilibrium regime.

One of the first theories developed was the stability limit conjecture [110, 111] predicting that liquid water cannot be superheated (below the critical pressure), stretched\* or undercooled indefinitely in the range of thermodynamic non-equilibrium, but a stability limit exists, generally called spinodal line, defined as the locus of points  $P_s(T)$  or  $T_s(P)$  in the  $(P, T)$  plane where:

$$\left( \frac{\partial P}{\partial V} \right)_T = 0$$

When the thermodynamic conditions approach this line, the metastable forms become totally unstable, leading the system to the real equilibrium form. It was speculated that the stability limits in the supercooled and superheated regimes could be two branches of a continuous line which passes through negative pressures in the  $(P, T)$  plane, defining in there the limit of stability of the stretched water. As a consequence a unique spinodal line could exist, being defined without any references to the phase into which the liquid water transforms, and the exact location of this retracing spinodal line may lead to the correct prediction of the free energy surface of water accounting for the anomalous properties of water.

Other theories developed more recently can explain the anomalous behaviors of water in the ordinary condition by assuming the existence of another type of singularity in the thermodynamic quantities in the undercooled regime. A proposed theory bases its predictions on the existence of a second critical point  $C'$  [112], unrelated to the ordinary liquid-gas one, that could be the critical point associated to an eventual HDA-like to LDA-like liquid/liquid transition<sup>†</sup> in a deep undercooled regime, analogous of the apparent first order transition observed between the two forms of amorphous ice [113]. The

---

\* Stretched water is a metastable form of water on which is applied traction force that determines a negative pressure

<sup>†</sup> HDA and LDA are respectively the high density and the low density amorphous forms of solid water observed by many authors in the undercooled regime from which a first-order transition is predicted

theory is supported only by molecular simulation because the fast nucleation of crystalline ice prevents the attainment of so such undercooled liquid water lying in the so called “no man’s land” [114].

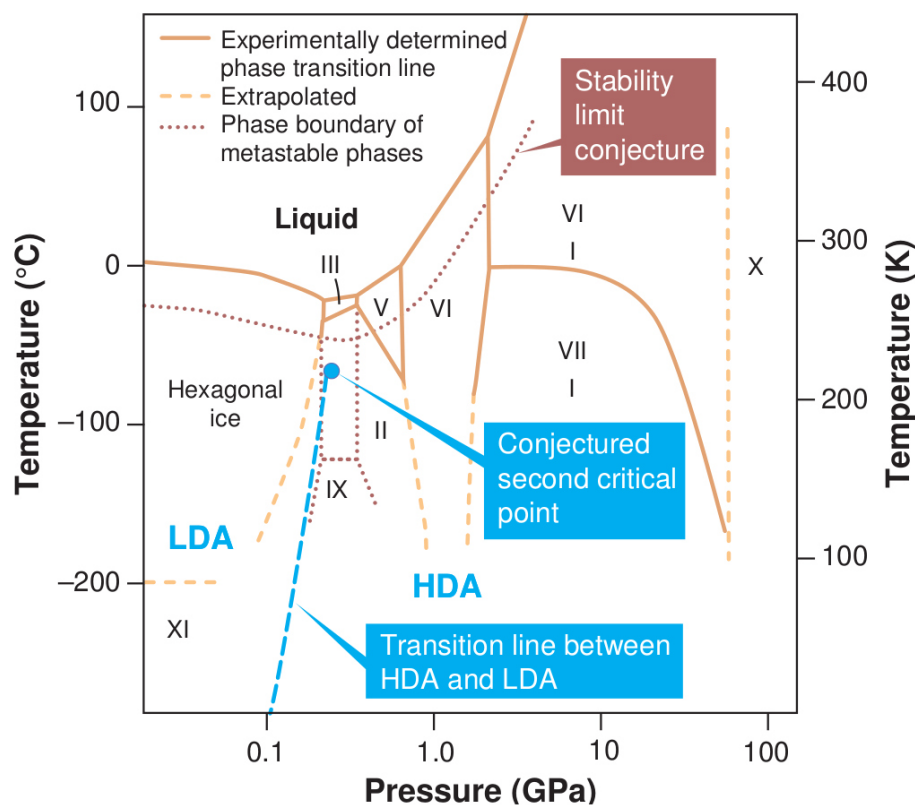


**Figure 3.1:** Phase diagram of water on which the spinodal line and the proposed LDA/HDA transition line up to the conjectured second critical point are superimposed [115].

Other theories draw similar conclusions even if a singularity is not expected. For example, the singularity free scenario [116], in which a water-like lattice model is proposed, predicts two local configurations, the first typical of molecules with strong hydrogen bond interactions, defined by a local state of minor energy because of the hydrogen bonds themselves, less entropy because of the directional hydrogen bonds, and less density because of the loosening of the packaging, the second typical of water molecules with weak hydrogen bonds interactions. Prediction made by this model, despite the simplicity of the model itself being free from any low-temperature singularities, are consistent with experimental observation. In a similar way a critical point

free scenario [117] explains the HDA/LDA transition between the amorphous forms via an order-disorder transition, not being a transition in the thermodynamic sense but defined by an abrupt decrease of heat capacity observed during the cooling as the translational and orientational degrees of freedom are frozen, changing from the typical value of a liquid to the one of a solid. This theory, even not requiring the existence of a second critical point, is anyway compatible with the second critical point interpretation.

The first conclusion that can be drawn from this overview is that most of the theories developed for the explanation of the water anomalies predict the existence of two different “phases” or local structures of liquid water in the undercooled regime, generally reported by many authors as low and high density liquids (LDL and HDL), as the liquid counterpart of the observed metastable high density and low density amorphous ice (HDA and LDA). Remnant of this two-phase system is supposed to influence the behaviour of water also in the ordinary liquid phase. The structure of liquid water is ruled by the self-association through the hydrogen bonds, which network is continuously destroyed and reformed to accomplish molecular motions [118], that has to be crucial in the determination of the anomalous properties distinguishing water from the simple liquids [109].

In the ordinary liquid phase two different limit local structures were identified [119]. Indeed the oxygen-oxygen partial structure factor  $S_{OO}(Q)$ , that was measured at 268 K as a function of pressure by means of neutron diffraction (figure 3.2), can be explained as the linear combination of two different local structures which relative ratio is a function of pressure itself. All the  $S_{OO}(Q)$  measured as a function of pressure can be interpreted using this approach and the two limit structures can be extrapolated for high and low pressure. The two forms are generally called high density water (HDW) and low density water (LDW), being characterised by a macroscopic density difference of about 30%. The reconstructed spatial density function for the two limit structures is reported in figure 3.2, showing a shortening of the distance between the central molecule and the second coordination shell that nearly collapses onto

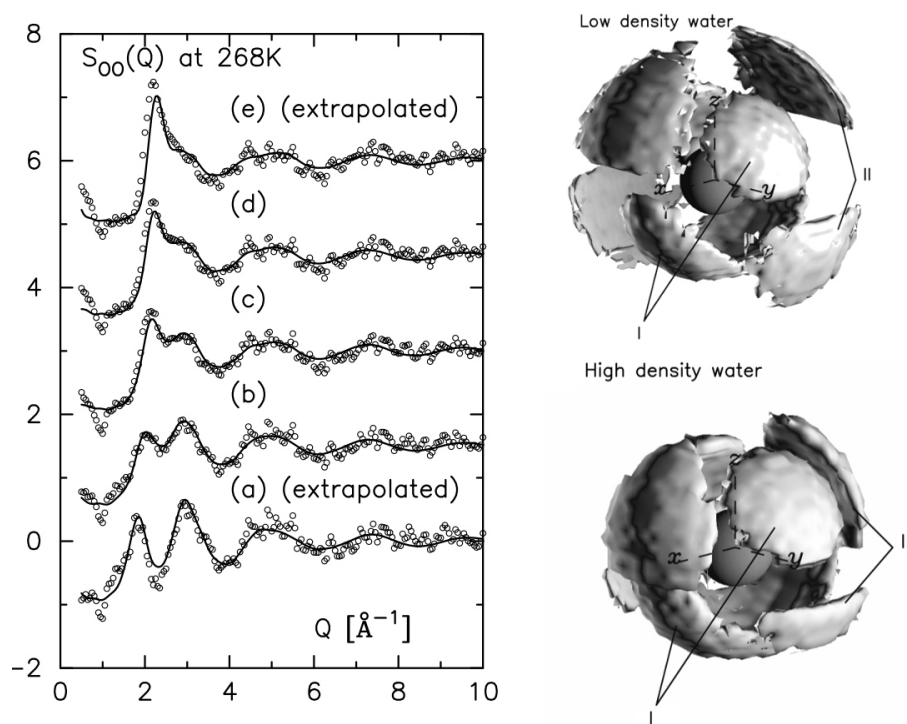


**Figure 3.2:** Oxygen-oxygen partial structure factor  $S_{OO}(Q)$  measured at 268 K as a function of pressure by means of neutron diffraction and reconstructed spatial density function for the two limit structures extrapolated for low and high density [119]. Measured values for 0.026 GPa (b), 0.209 GPa (c) and 0.400 GPa (d); (a) and (e) traces are the extrapolated  $S_{OO}(Q)$  corresponding respectively to the neat LDW and HDW structures.

the first one, on going from the LDW to HDW. Despite, the first coordination shell is almost unaltered staying perfectly tetrahedral. At now it is not clear if the two structure coexist together in the ambient conditions forming domains that inter-convert in a dynamical equilibrium and whose ratio depends on the thermodynamic quantities, as could be evidenced by some small angle X-ray scattering experiments [120], or if water structure transforms homogeneously from the one limit structure to the other as pressure and temperature are changed [113]. Classical molecular dynamics [121] shows a continuous transformation from LDW to HDW as the pressure is raised, consisting in the localisation of second shell molecules in the interstitial (octahedral) sites of the first one, that is almost unaffected by the increasing density, being consistent with the observation. Although, a definition of the boundaries between

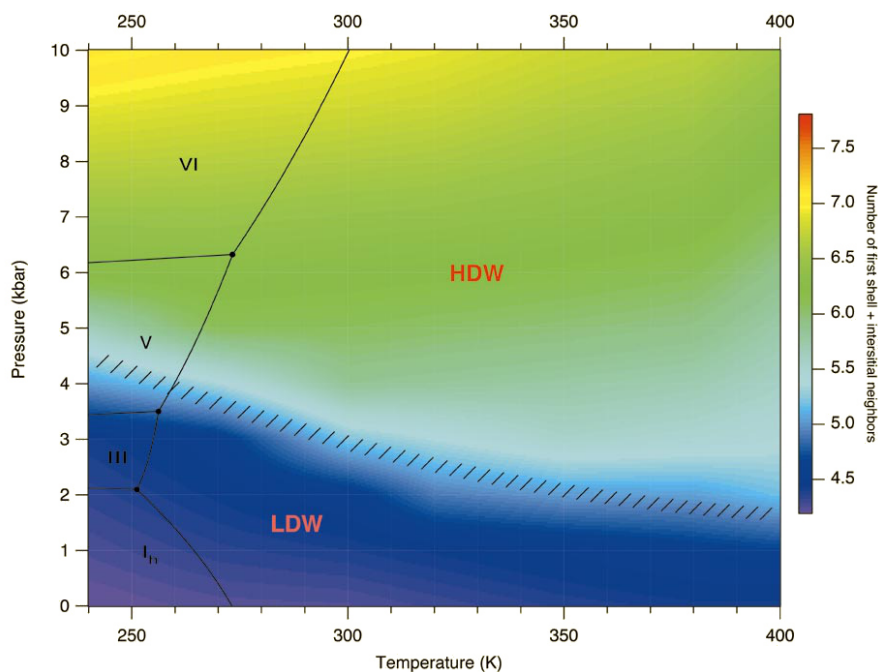


**Figure 3.3:** Number of first nearest neighbours consisting in the first coordination shell and interstitial water molecules reported in a chromatic scale superimposed on the phase diagram of water. The shaded area is the domain in which interstitial and hydrogen bonded molecules have equal contributions to the  $\angle O-H-O_2^H$  angle distribution, taken by the authors as separation between the LDW/HDW regimes [121].

the two form of water is tricky because the mean structure is found to change in a continuous way, making it impossible to trace a line able to separate the two density domains in the phase diagram of water, and in spite of years of research and measures performed with very different techniques[119, 122–126], an experimental quantity capable of distinguishing between the two forms or with a clear different behaviour into the two domains was never found.

## 3.2 Rotational and vibrational dynamics of water

As shown in the previous section, changing pressure and temperature is a powerful method to induce the transformation of the low density (LDW) into the high density water (HDW) within the thermodynamic range of the stable liquid water, which can be spanned using the diamond anvil cell technology.

On the other hand, the ultrafast mid-infrared pump-probe spectroscopy is a non-linear time resolved technique able to provide detailed information both on the orientational dynamics of water [127] and on the fast dynamics characterising the hydrogen bond network [128, 129], that has fundamental role in determining the structure of liquid water. The two techniques were combined together in this work for the first time, which represents in itself an experimental breakthrough, with the purpose of providing detailed information on the nature of the two water structures and their inter-conversion. We compressed the sample in a membrane sapphire anvil cell. We used sapphire with high optical quality and enhanced infrared purity in such a way that the spectral interference with the sample was negligible and the sapphire anvils were cut to have the non-birefringent optical axis parallel to the pump and probe beams to preserve their polarisation. The use of sapphire instead of diamond was motivated by the need of having a negligible absorption by the anvils at  $\sim 2600\text{ cm}^{-1}$ , as will be detailed in the following.

The dimensions of the samples was in the order of  $50\text{ }\mu\text{m}$  in thickness and  $400\text{ }\mu\text{m}$  in diameter, and it was contained in a gilded gasket to avoid any chemical reactivity with the bronze of which the gasket is made. We performed all the measures on a diluted mixture of  $\text{D}_2\text{O}$  in  $\text{H}_2\text{O}$  in a ratio of 7:199 ( $\text{D}_2\text{O}/\text{H}_2\text{O}$ ), in which we can confidently assume that, statistically, only isolated HOD molecules surrounded by  $\text{H}_2\text{O}$  molecules are present. In this situation the OD stretching of the HOD molecule is a well spectrally isolated and non-coupled infrared mode, being a suitable probe of water behaviour, namely of how its dynamic is affected by the strength of the hydrogen bonds and how the surrounding water local structure is modified by pressure or temperature [130].

In the ultrafast mid-infrared pump-probe spectroscopy an energetic broadband infrared pulse (pump), whose time duration is typically is tens of femtoseconds, is sent to the sample to induce an excitation whose residual is probed after different delay times by a second short pulse (probe). In this way a decay dynamics of the induced excitation can be reconstructed with a typical time

resolution of a hundred of femtoseconds, that is suitable for the analysis of phenomena evolving in the picoseconds time-scale. The signal is quantified by the transient absorbance  $\Delta A$  that is calculated according to the equation 3.1, as the logarithm of the ratio between the probe intensity with and without the pump beam, both normalised to the intensity of the reference beam, a pulse that probes the sample always in an unperturbed condition.

$$\Delta A = -\log_{10} \frac{I_{probe,pump\ ON}/I_{ref}}{I_{probe,pump\ OFF}/I_{ref}} \quad (3.1)$$

In the simplest experiment the pump pulse is absorbed by the sample, promoting population from the fundamental  $|0\rangle$  vibrational state to the first excited vibrational state  $|1\rangle$ . Then the system evolves until the second infrared pulse is sent to probe the residual excitation. The transient absorbance calculated according to the equation 3.1 describes both the depletion of the  $|0\rangle \rightarrow |1\rangle$  transition (bleaching), which gives a negative signal, and the  $|1\rangle \rightarrow |2\rangle$  transient absorption shifted in frequency from the fundamental absorption because of the vibrational anharmonicity. A sketch of the process is given in figure 3.4

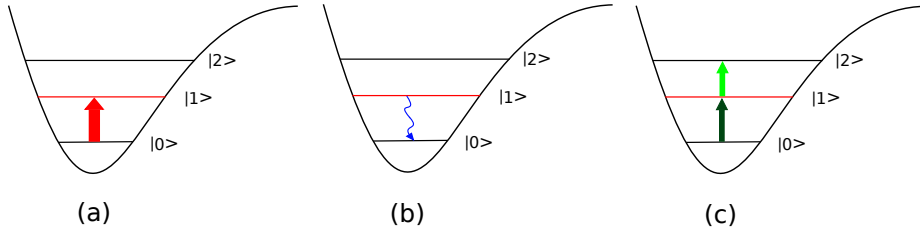


**Figure 3.4:** Sketch of the transient absorption mechanism involved in a basic experiment: (a) An intense polarised infrared pulse (the pump) excites the molecular oscillator; (b) The induced excitation evolves for a time  $\Delta t$ ; (c) A second polarized pulse probes the residual excitation consisting in a depletion of the  $|0\rangle \rightarrow |1\rangle$  transition (bleaching, in dark green) and in the  $|1\rangle \rightarrow |2\rangle$  transient absorption (in light green).

Both vibrational and orientational dynamics give contribution to the signal decay [127]. The vibrational decay is responsible for the relaxation of the vibrationally excited system to the initial unperturbed state in which all the population is in the fundamental vibrational state. On the other hand, the



effect of the orientational dynamics on the signal is due to the fact that the rotation of the molecule changes the direction of the transition dipole moment, that becomes not anymore detectable by a probe with same polarisation as the pump. In dilute solutions of HOD in H<sub>2</sub>O, intra- and intermolecular energy transfer between neighbour oscillators are negligible, then the orientational dynamics can be directly measured by the rotational anisotropy  $R(t)$ . Moreover, the two dynamic contributions can be individually accounted, performing transmission measurements in parallel ( $T_{\parallel}$ ) and perpendicular ( $T_{\perp}$ ) polarisation configurations of pump and probe pulses, and calculated using the following formulas:

$$\Delta\alpha_{iso} = \frac{\Delta\alpha_{\parallel} + 2\Delta\alpha_{\perp}}{3} \quad (3.2)$$

$$R(t) = \frac{\Delta\alpha_{\parallel} - \Delta\alpha_{\perp}}{3\Delta\alpha_{iso}} \quad (3.3)$$

$$\text{where } \Delta\alpha_{\parallel} = \ln\left(\frac{T_{\parallel}}{T_0}\right); \quad \Delta\alpha_{\perp} = \ln\left(\frac{T_{\perp}}{T_0}\right)$$

In the equation 3.2,  $\Delta\alpha_{iso}$  is the isotropic signal that is not dependent on the rotational dynamic, thus in our experimental condition it is a direct measure of the vibrational decay of the OD stretching and it is the same quantity that can be measured if the relative angle between pump and probe polarisation is the magic angle ( $\theta_m = \arctan(\sqrt{2}) \simeq 54.7^\circ$ ).

In order to calculate the correct value of the anisotropy decay and of the vibrational relaxation times, the time dependent thermal signal due to the temperature increase of the probed volume of sample caused by the absorption of the pump has to be taken in account [131–134]. Indeed, all the measured transient absorption data decay to a final offset, that is constant in the typical timescale covered by the experiment (hundreds of picoseconds), spectrally characterised by a bleaching contribution on the red side of the spectrum and by an induced absorption on the blue side (see figure 3.6). The time-dependence of the thermal signal can be extracted by fitting the isotropic sig-

nal  $\Delta\alpha_{iso}$  with a sequential three level kinetic scheme defined by the coupled rate equations reported in figure 3.5.

$$\frac{dN_e}{dt} = -\tau_v^{-1} N_e$$

$$\frac{dN_g}{dt} = \tau_v^{-1} N_e - \tau_T^{-1} N_g$$

$$\frac{dN_T}{dt} = \tau_T^{-1} N_g$$

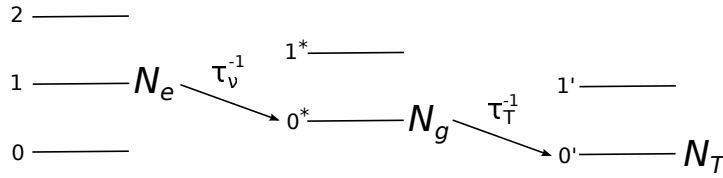


**Figure 3.5:** Scheme of the three states system employed for the interpretation of the dynamics that takes into account the thermal effect [133]. An excited HDO molecule decays from the  $|1\rangle$  level to the  $|0^*\rangle$  level with a time constant  $\tau_v$ , then in a second step it decays to the ground heated state  $|0'\rangle$  with a time constant  $\tau_T$ .

These equations involve the initially excited molecules  $N_e$ , the relaxed ones  $N_g$ , and the thermally excited molecules  $N_T$ . We used this model to fit all the recorded kinetic traces for a given value of temperature and pressure, at the same time imposing the constant  $\tau_v$ , that is the vibrational lifetime, and  $\tau_T$  as global parameters. Once the temporal evolution of the thermal contribution defined by the time constant  $\tau_T$  was obtained, we subtracted it from  $\Delta\alpha_{\parallel}$  and  $\Delta\alpha_{\perp}$  signals and recalculated the corrected anisotropy decay according to equation 3.3. The corrected  $R(t)$  was then fit by a single exponential function to obtain the time constant  $\tau_R$  that is frequency independent for each set of data recorded at the same pressure and temperature conditions. A set of transient spectra as a function of the pump-probe delay is reported in figure 3.6, and examples of decay kinetics for the corrected isotropic signal and rotational anisotropy are reported in figure 3.7.

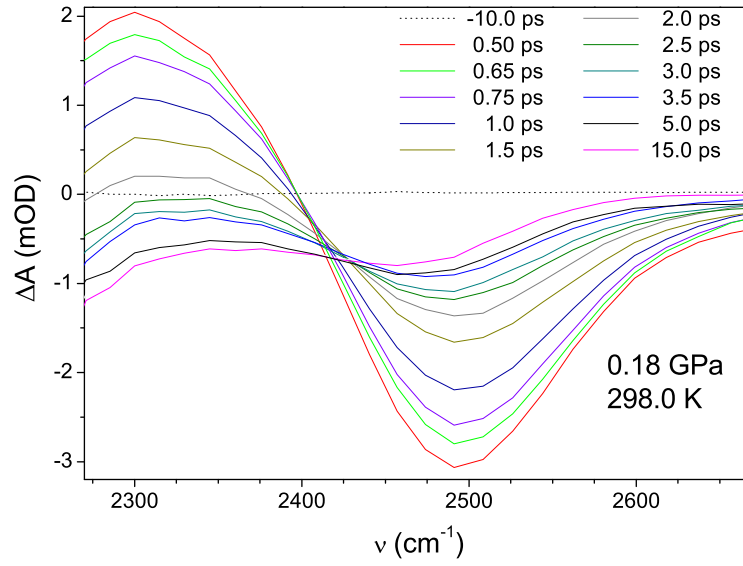


**Figure 3.6:** Transient absorption spectra of the OD stretching of HOD molecule, reporting the  $\Delta\alpha_{iso}(t)$  measured at 0.18 GPa, 298 K.

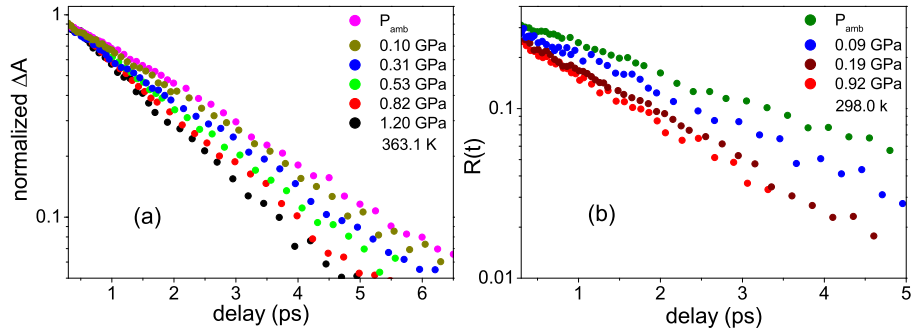


**Figure 3.7:** a) Example of the temporal evolution of the isotropic signal probed at  $2580\text{ cm}^{-1}$  and reported in a semi-log plot for different pressures at 361.1 K. b) Example of the temporal evolution of the  $R(t)$  reported in a semi-log plot for different pressures at 298 K

By applying the methods described above we measured the anisotropy decay time constant  $\tau_R$  and the OD stretching vibrational lifetime at two different temperatures (298.0 and 363.1 K) as a function of pressure up to about 1 GPa. The data are reported in figure 3.8. It is clear that at 363.1 K the evolution of both time constants is strictly linear as a function of density in the whole

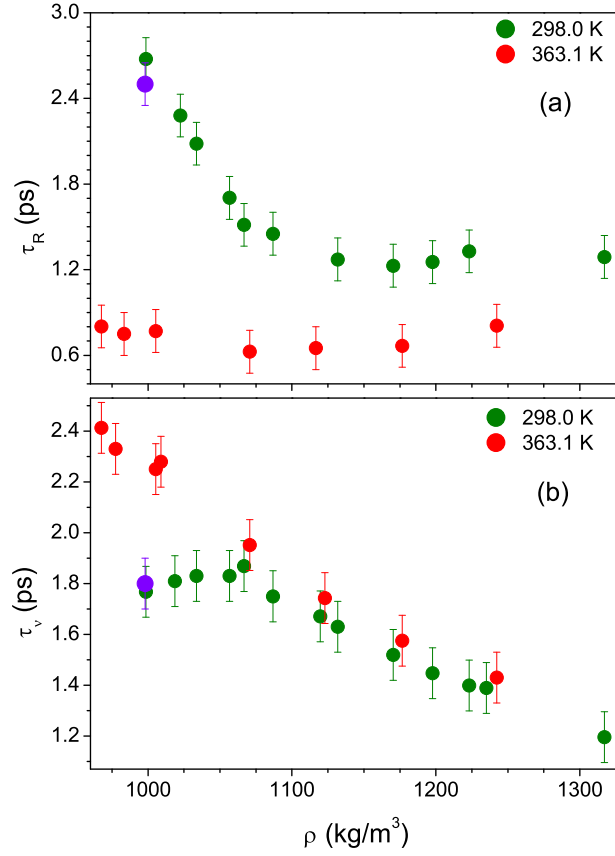


**Figure 3.8:** a) Rotational anisotropy time constant determined by single exponential fit of  $R(t)$  measured at 298.0 K (green bullets) and 363.1 K (red bullets) as a function of pressure. b) OD stretching lifetime obtained from  $\Delta\alpha_{iso}(t)$  as described in the text. The violet dots are the literature reference values at room conditions [127].

range analysed, whereas at 298.0 K a clear change in the slope is observed for both parameters around 1070  $\text{kg/m}^3$  <sup>‡</sup>, a density corresponding to about 0.2 GPa. In particular the rotational anisotropy constant  $\tau_R$ , that in our experimental condition is a direct measure of the orientational dynamics, is density independent at 363.1 K being in the whole range  $\sim 0.8 \pm 0.2$  ps, and at the same temperature the vibrational lifetime  $\tau_v$  is a linear decreasing function of the density. At 298.0 K  $\tau_R$  decreases almost linearly from the value of  $2.7 \pm 0.2$  ps measured at ambient pressure to  $\sim 1.3 \pm 0.2$  ps at 0.2 GPa, remaining constant

<sup>‡</sup>All the density reported are calculated from the equation of state of water resulting from the IAPWS formulation 1995. [135]

for further compression. At the same pressure  $\tau_v$ , that was almost constant at lower pressures, starts to linearly decrease as a function of density, with a slope similar to the that observed at 363.1 K.

### 3.2.1 Infrared analysis of water stretching mode

The evolution of the OD lifetime and the rotational anisotropy should reflect in the vibrational linewidth. We performed a careful infrared analysis of the OD stretching mode of the HOD molecule in  $\text{H}_2\text{O}$  as a function of pressure along several isotherms, by means of FT-IR spectroscopy. The same mixture described previously was compressed in a membrane sapphire anvil cell, whose temperature was controlled by a calibrated silicon diode and a K-type thermocouple soldered to the gasket near the sample and regulated by a remote controlled resistive heater for the high temperatures and by a closed-cycle helium cryostat for the low temperatures. An example of a recorded spectrum is reported in figure 3.9. As already described in the previous section, at the low concentrations of the experiments all deuterium atoms are present as HOD molecules surrounded by  $\text{H}_2\text{O}$  molecules. In this condition the OD stretching mode is non coupled and inhomogeneously broadened, thus the infrared band can be fit, after a baseline subtraction, with a single Gaussian function. As a confirmation, the accuracy of the Gaussian fit is excellent for all the temperatures and pressures inspected, ranging from 260 to 363 K and from near ambient pressure up to 1.4 GPa.

The density evolution of the full width at half maximum (FWHM) of the OD stretching band at the inspected temperatures is reported in figure 3.10. The key to the interpretation of all data sets is given by the density evolution at 298.0 and 363.1 K, temperatures at which the water dynamics was studied by the infrared pump-probe technique. In particular at 298.0 K we observed two distinct linear regimes in the density evolution of the FWHM with a change in the slope at  $\sim 0.175$  GPa, a pressure that is approximately the same, considering the measurement uncertainty, to the value at which the rotational anisotropy levels to a constant value. In the same way at 363.1 K the FWHM has a

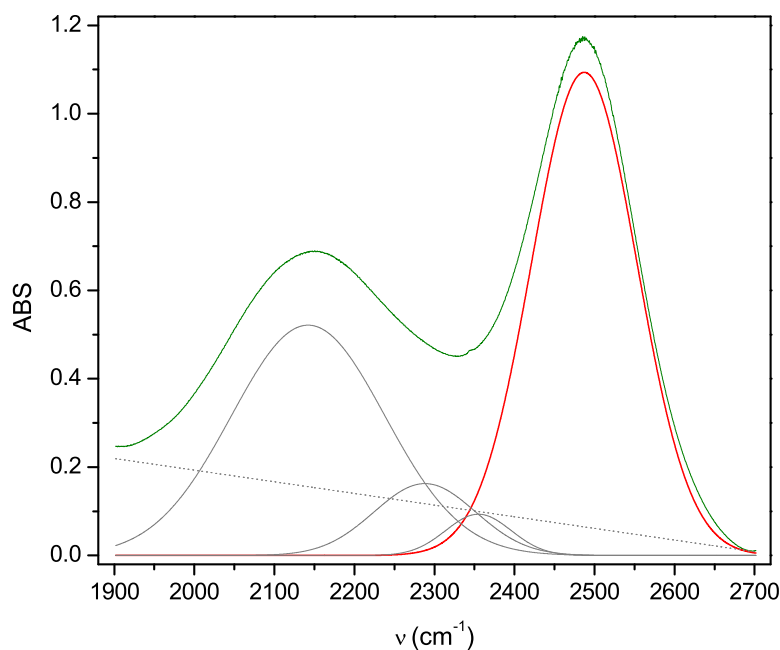


**Figure 3.9:** Example of a Gaussian fit of the OD stretching mode of the HOD molecule at  $T = 260$  K and  $P = 0.39$  GPa, after a straight baseline subtraction.

single linear behaviour as a function of density without any slope changes as already observed for the rotational anisotropy and vibrational time constants.

The slope change observed at 298 K and  $\sim 0.175$  GPa is easily explainable looking at the pressure evolution of the dynamic parameters measured in the pump probe experiment and reported in figure 3.8. Indeed, the line broadening of the inhomogeneously broadened mode depends on both vibrational and rotational dephasing terms, that can be taken into account by their measured time constants  $\tau_v$  and  $\tau_R$ . At 298.0 K, from low pressure up to  $\sim 0.175$  GPa, the line broadening as a function of pressure is dominated by the orientational term as the molecular rotation is constantly accelerated by the increasing density, while the vibrational life time is constant in this pressure range. Conversely for pressures higher than  $\sim 0.175$  GPa, the rotational anisotropy is constant as a limit rotational speed is reached, thus the orientational term does not give any further contribution to the line broadening as a function of

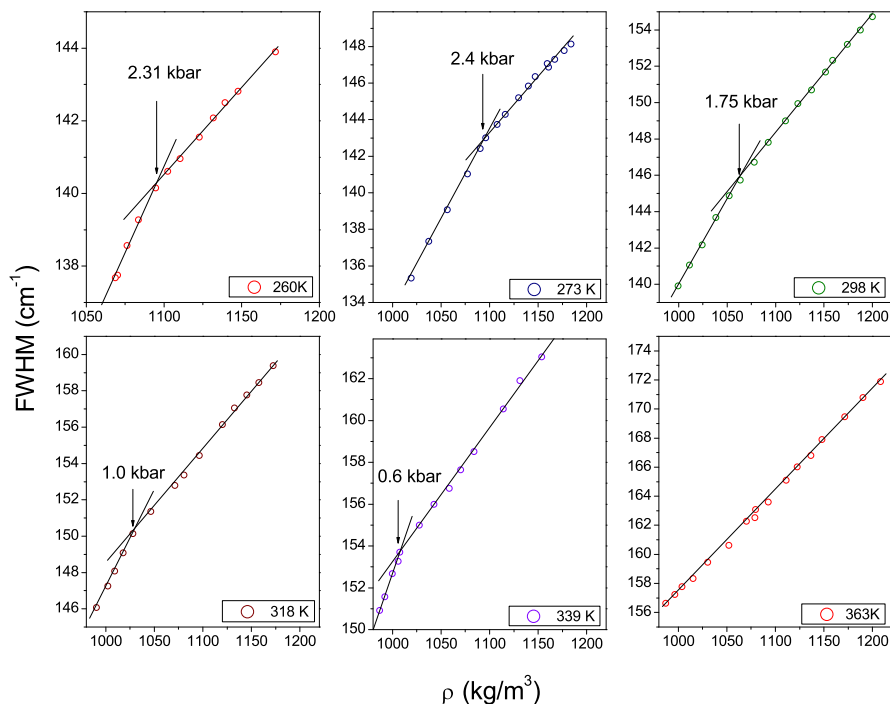


**Figure 3.10:** Full width at half maximum obtained by Gaussian fit of the OD stretching mode of the HOD molecule reported for several isotherms as a function of pressure. For each set of data a linear regression of the data for low and high density is reported. The pressure Values reported on the graphs are corresponding for each temperature to the density at which the intersection of the two linear regressions is observed.

pressure that is now dominated by the only vibrational term, whose dynamics is accelerated in this range of pressure. According to this, we can conclude that the pressure at which the kink is evidenced corresponds to the pressure at which the water limit rotational speed is reached. The single linear behaviour observed at 363.1 K for all the parameters gives further confirmation of this picture. Then we can easily obtain the pressure at which the limit rotational speed is reached for each temperature by means of the analysis of the FWHM of the OD stretching mode as a function of density. As observed in figure 3.10, this pressure value constantly shifts at low density as the temperature is raised till 363.1 K in which the kink is not any more detectable.

### 3.2.2 Computational analysis and data interpretation

A correlation between the structural evolution and the dynamics of water can be provided by computational methods, giving the possibility to fit all the observed data in a consistent picture able to explain the water dynamical behaviour in the range of density corresponding to the thermodynamic conditions of the stability of liquid phase. Classical molecular dynamics simulation were performed at ambient temperature and density ranging from 997 to 1233 kg/m<sup>3</sup>, and at ambient pressure and temperature ranging from 273 up to 363 K. The calculations were performed in the NVE ensemble using a recently developed polarisable force field (ASAP) [136] particularly effective in the description of structural properties of water both at ambient and at extreme conditions. The starting configurations were always obtained by simulation runs carried out with the Moldy program [137] and adopting the SPC/E potential [138]. Each sample, consisting in 96 H<sub>2</sub>O molecules and 7 HOD molecules, was hence thermalised by velocity rescaling at the temperature of the simulation for 500 ps using the SPC/E potential, followed by an accumulation run of about 1 ns with a time step of 0.25 fs, collecting the configurations every ten steps. Starting from the last configuration the system was then thermalised in the NVT ensemble for about 50 ps with the ASAP model, integrating the equations of motion with a time step of 0.24 fs and then collecting the trajectories in the NVE ensemble every 10 steps in the production run of about 200 ps. For comparison, simulations were carried out also using only the well known SPC/E model which was shown to be helpful in the description of ultrafast vibrational spectroscopy experiments for the study of water dynamics in the liquid phase [139]. Anyway, the set of data obtained using the two potentials are in good agreement. The resulting pair distribution functions  $g(r)$  obtained using the ASAP model are reported in figure 3.11. In agreement with previous results [119, 121, 122], the  $g(r)$  for the O $\cdots$ H contacts show that the hydrogen bonds are only slightly perturbed by pressure. Conversely the second maximum of the  $g(r)$  for the O $\cdots$ O gradually moves inwards with increasing density, filling the first minimum at 3.3 Å.



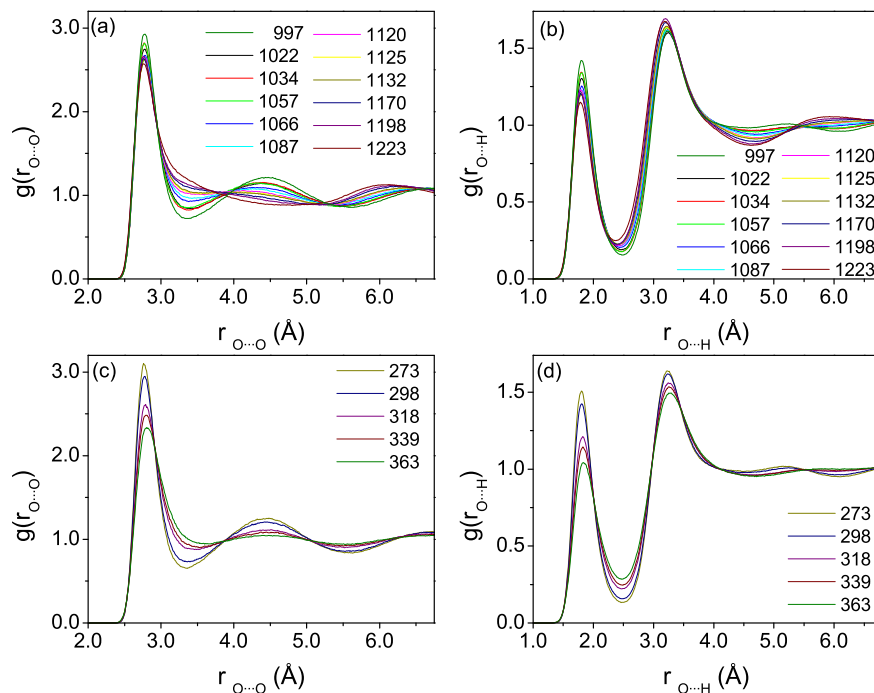


**Figure 3.11:** Pair radial distribution functions  $g(r)$  obtained from the simulations carried out with the ASAP polarisable force field [136] for O···O (a) and O···H (b) at ambient temperature as a function of density, and O···O (c) and O···H (d) at ambient pressure as a function of the temperature.

The information obtained from the  $g(r)$  at 1034 and 1198 kg/m<sup>3</sup> at room temperature is summarised in the 2D plots in figure 3.12, in which the surface represents the probability distribution for each O···H and O···O intermolecular distance. From this representation it is easy to notice that the two regions corresponding to the first coordination shell are only slightly affected by the density increase, whereas the second shell shifts with increasing density towards the first one occupying the interstitial sites. This is confirmed also by the value of the tetrahedral order parameter  $q_k$ , which remains almost constant with increasing density, when the analysis is restricted to the H-bonded water molecules (figure 3.13). The parameter was computed adopting the equation 3.4 [140]:

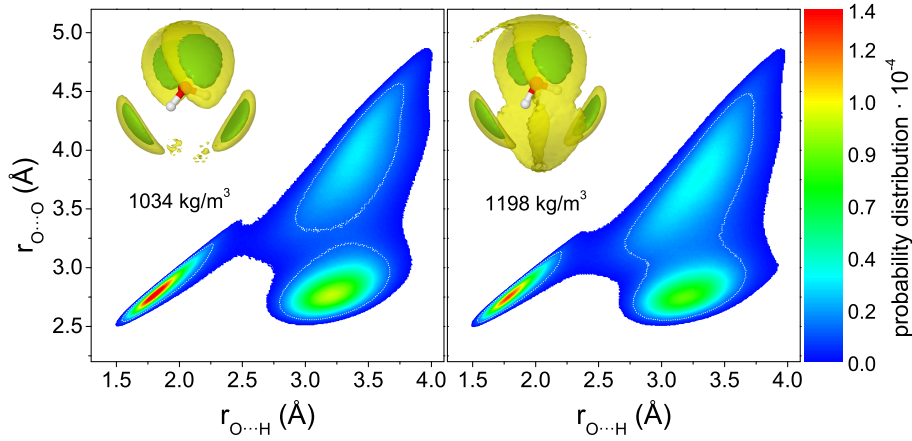


**Figure 3.12:** Configurational space for the water molecules in the first and second coordination shell, at ambient temperature and 1034 and 1198 kg/m<sup>3</sup>. In the insets, the space regions representing the probability of finding hydrogen bonded (in green) and second shell (in yellow) molecules are reported, with isosurface cut-off of 0.0015 and smoothed with a Gaussian function for longer distances.

$$q_k = 1 - \frac{3}{8} \sum_{i=1}^3 \sum_{j=i+1}^4 \left[ \cos \theta_{ikj} + \frac{1}{3} \right] \quad (3.4)$$

where  $k$  is the index of the water molecule taken as reference. The  $\theta_{ikj}$  angles were evaluated following two distinct approaches: the first, for the  $i$  and  $j$  water molecules hydrogen bonded to the  $k$  molecule and the second for the  $i$  and  $j$  water molecules with shortest O $\cdots$ O distance with the  $k$  molecule. The tetrahedral order parameter  $q_k$  assumes the value of 1 for a perfect tetrahedral arrangement and goes to 0 in absence of order. Only using the second approach a large shoulder grows in correspondence to  $q_k \approx 0.5$  at the higher density, being the consequence of the presence of interstitial water molecules at distances comparable to those of the hydrogen bonded first nearest neighbours and not corresponding to a real distortion of the tetrahedron of hydrogen bonded molecules.

Nevertheless, the increasing temperature has effect also on the first coordination shell as evidenced by the variations of the O $\cdots$ O pair radial distribution functions (figure 3.11), showing a progressive interpenetration of the

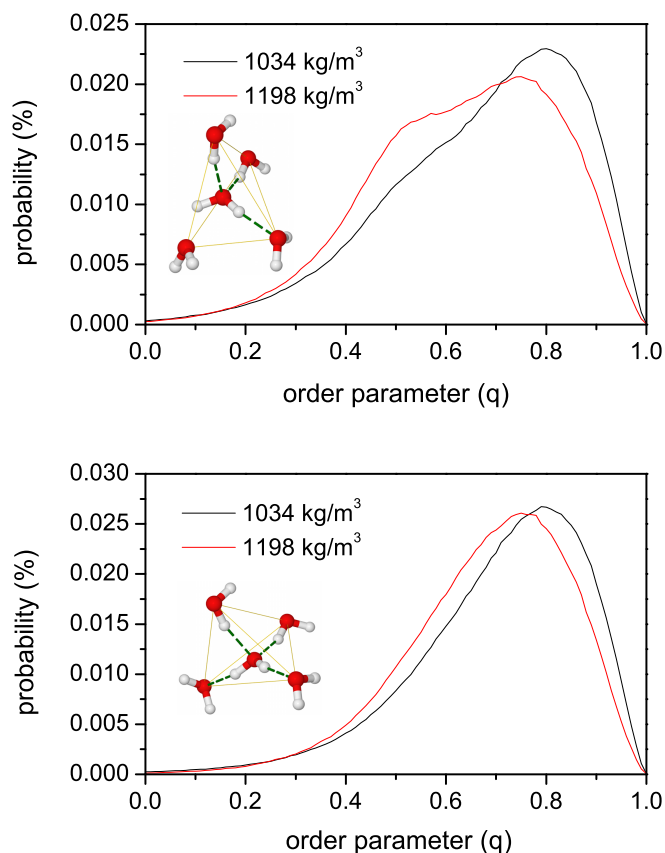


**Figure 3.13:** Tetrahedral order parameter for hydrogen bonded (lower panel) and nearest O···O neighbours (upper panel) water molecules with respect to that taken as reference.

first and second shell caused in this case by an increase of exchange between the molecules of the two shells. This behavior is confirmed by the variation in the  $g(r)$  for the O···H contacts which shows a modification of the hydrogen bond network not observed by increasing the pressure.

The rotational anisotropy decay was calculated at ambient temperature as a function of density, from the time correlation function of the second rank Legendre polynomial of the direction unit vector  $\vec{u}$  for each HOD molecule according to the formula 3.5.

$$R(t) = 0.4 \langle P_2[\vec{u}(0) \cdot \vec{u}(t)] \rangle \quad (3.5)$$

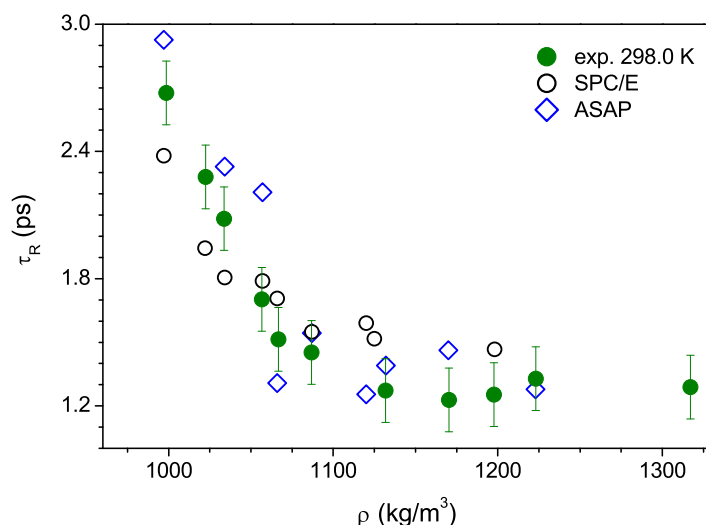


**Figure 3.14:** Rotational anisotropy time constant as a function of density at ambient temperature computed using ASAP and SPC/E potentials, compared to the measured one at the same temperature. An offset of 0.5 ps is subtracted from the ASAP values for sake of better comparison.

In figure 3.14 the values for the rotational anisotropy time constants  $\tau_R$  obtained by exponential fit of the  $R(t)$  decays calculated using the two potentials (SPC/E and ASAP) are reported in comparison with the experimental data at ambient temperature. Both sets of calculated data share the same behaviour seen in the experiments, namely an initial decay and a levelling off for density above 1100 kg/m<sup>3</sup>. The excellent agreement between the computed and the experimental data gives us confidence in the description provided by the simulation. The change in  $\tau_R$  can be thus related to the structural changes previously described and in particular to the collapse of the second shell molecules onto the first, corresponding to an increase in the number of non-bonded molecules at short distance from the central one, as discussed in the following.

By counting the number of the configurations in which at least one non hydrogen-bonded molecule is closer to the central molecule than the bonded ones, we can estimate the increase with density of the interstitial water molecules in the first solvation shell, whose evolution is reported in figure 3.15.

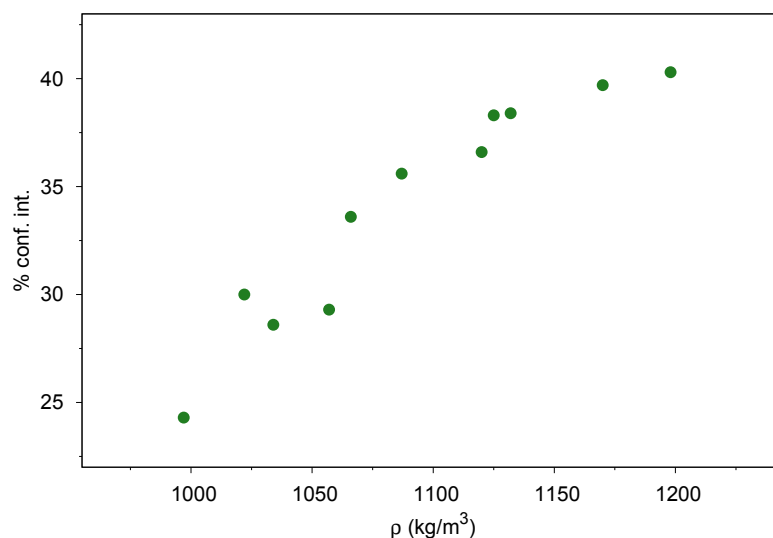


**Figure 3.15:** Density evolution of the ratio of configurations in which at least one interstitial molecule not hydrogen bonded is present within the first solvation shell.

The result provides an explanation for the pressure dependence of the measured anisotropy decay, as the larger number of interstitial molecules at high density increases the probability for the tagged molecule of jumping from one hydrogen bonded configuration to another. This phenomenon is able to speed up the rotation of the water molecule in perfect accord to the theory [118], predicting that the molecular rotation is not free in the hydrogen bonded liquid. These instantaneous events do not alter appreciably the overall number of H-bonds and leave the average hydrogen bond connectivity almost unchanged as confirmed by the fact that the mean number of hydrogen bonds formed by the oxygen atom of the water molecules does not change appreciably with increasing pressure, being about 2 in the whole range of explored density. The increased quantity of equally probable tetrahedral configurations then facilitates the orientational motions inducing a shortening of the molecular orientational time up to the density value of  $\sim 1100$  kg/m<sup>3</sup>. Above this value,  $\tau_R$  does not change with further compression meaning that a limit configuration in terms of rotational mobility is achieved. Thus pressure tunes with continuity the insertion of second shell molecules in the interstitial sites

of the first shell, which results in an acceleration of the process of breaking and making hydrogen bonds affecting the orientational dynamics but without altering the tetrahedral coordination. A continuous structural modification of the liquid is induced, until the high density configuration is achieved. These structural modifications are intimately connected to the change of the dynamical properties revealed by the spectroscopic data. At ambient temperature this process completes around  $1070 \text{ kg/m}^3$  ( $0.2 \text{ GPa}$ ) in a good agreement with the calculated value ( $1100 \text{ kg/m}^3$ ), and no further speeding up of the orientational motion is observed above this density. The same properties are also affected by the interpenetration of the first and second shell driven

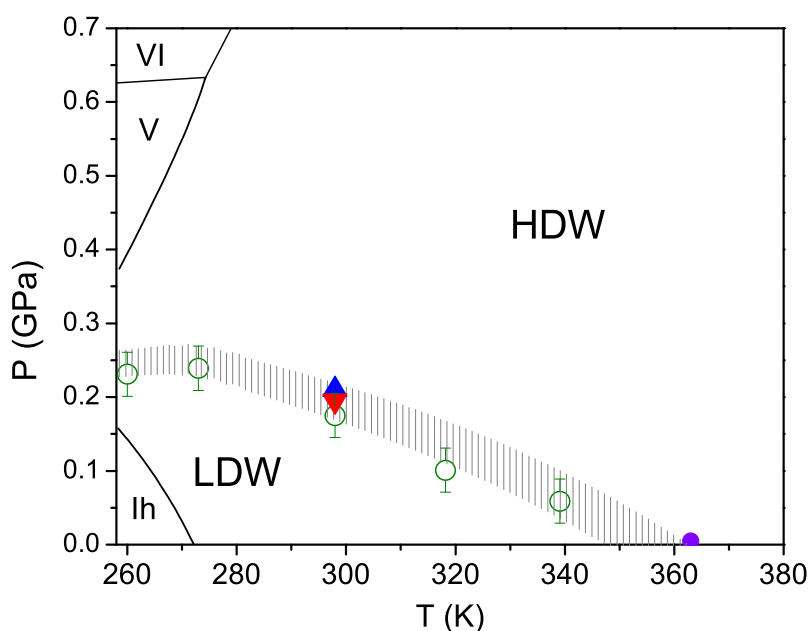


**Figure 3.16:** Identification of the P,T regions corresponding to the LDW and HDW dynamical regimes and tentative depiction of the P,T condition where the limit configuration corresponding to the completion of the insertion of the second shell molecules into the first shell is achieved, showed as a shaded area. Empty dots: slope change of the FWHM vs density; triangles: slope change of experimental (blue) and computed (red) rotational anisotropy with density; full dot: temperature value at ambient pressure where water behaves as HDW according to FWHM and rotational anisotropy data.

by the temperature that induces a decrease of the orientational correlation time up to the attainment of a structural configuration for which the orientational dynamics is not anymore significantly affected by pressure. Then we can conclude that liquid water can achieve two dynamical regimes depending on both temperature and pressure, characterised by different nearest neighbour configurations and differing by the orientational dynamics. Maintaining the nomenclature of low (LDW) and high density water (HDW) [119], we can now define the experimental boundaries between the two density regimes as the locus of (P,T) points at which the limit configuration in terms of rotational dynamics is achieved. These boundaries, revealed by the different methods described previously are reported in figure 3.16.

### 3.3 Summary

In this work we combined for the first time the pump-probe ultrafast infrared spectroscopy with ultra-high pressure devices to access the GPa range, providing new insights into understanding the dynamical behaviour of water in the whole range of thermodynamic stability of the liquid phase, from 273 to 363 K, from ambient pressure up to 1.2 GPa. We measured the OD stretching rotational anisotropy decay time-constant and vibrational lifetime, in a solution of HOD in H<sub>2</sub>O, pressurised in a sapphire anvil cell, as a function of pressure at different temperatures, and performed a careful infrared linewidth study of the OD stretching mode as a function of temperature and pressure. Aided by classical molecular simulations performed with the well known SPC/E potential as well as ASAP, a new polarisable force field particularly effective in the description of structural properties of water at ambient and at extreme conditions, we interpreted the pressure evolution of the measured parameters in terms of structural changes, identifying the key to correlate structure and dynamics. We find that the modification induced in liquid water by changing pressure and temperature is well described as the crossover between two regimes, for which the usual designation found in the recent literature of HDW

and LDW can be maintained. The main distinctive character of the two regimes is found to be the dynamic behavior, which results from the interplay of the structural modification induced by pressure and of the temperature effect. Another remarkable result is represented by the possibility of revealing the changes in the dynamical regime by the density dependence of the linewidth of the OD stretching mode which is an accessible and reliable experimental method to finely define the pressure and temperature region of the two density regimes.



## Experimental setup

### 4.1 FT-IR

All the infrared measurements presented in this work were performed with a Bruker-IFS 120 HR FTIR spectrometer modified for high pressure equipment [141]. The instrument is equipped with three different light sources to cover the whole spectral range from the visible/near infrared (tungsten lamp), through the medium infrared (Globar) up to the far infrared (mercury lamp) from about 5 up to  $25000\text{ cm}^{-1}$ . Interchangeable beam splitters of Mylar, KBr and  $\text{CaF}_2$  are also present. Four detectors are present: a bolometer ( $10 - 600\text{ cm}^{-1}$ ), a mercury–cadmium–tellurium semiconductor (MCT,  $500 - 6000\text{ cm}^{-1}$ ), an indium antimonide semiconductor (SbIn,  $1850 - 9000\text{ cm}^{-1}$ ) and a silicon diode ( $9000 - 32000\text{ cm}^{-1}$ ). The modifications to the original instrument were necessary to avoid the technical limitations arising from the small dimensions typical of the sample contained in the diamond anvil cell rarely exceeding a hundred of microns. Most of the technical limitations of the commercial instruments are due to the low brilliance of the typically employed thermal source in the medium infrared such as a Globar lamp and detectors with low sensitivity as the MCT associated to infrared beams of typical dimension in the order of millimetres that make impossible performing measures on such small samples without an appropriate condensing system. The system employed to this purpose in the experiments presented consists in a couple

of gold ellipsoidal mirrors mounted in an optical bench and coupled to the infrared beam of the spectrometer. The demagnification ratio of the ellipsoid mirrors is of about a factor of 4 resulting in a waist on the focus of the same dimensions of the sample determining an effective enhancement of the transmission through the diamond anvil cell of over than an order of magnitude.

The low temperature can be achieved by using a closed cycle double step helium compression cryostat (DE204SL by APD Cryogenics) that is coupled with the spectrometer. The cold tip of the cryostat holding the DAC by a copper conductive clip is inserted in the sample chamber that is isolated from the other parts of the instrument and evacuated using a turbomolecular pump down to pressures of  $10^{-2} - 10^{-3}$  Pa. The temperature is controlled by means of a calibrated Si-diode on the cold tip and a Si-diode or an appropriate thermocouple placed on the DAC near the gasket.

The high temperature can be achieved by means of a resistive heater that envelops the cell. The resistive heater can be remotely controlled from the outside of the instrument and uses as a feed-back of the temperature a thermocouple inserted either inside the heater itself or inside the cell, fixed near the gasket.

The pressure can be regulated remotely by a capillary connecting the pressure regulator outside the instruments to the membrane of the MDAC inside the sample chamber, via a vacuum feed-through. The pressure can be measured in situ by the ruby fluorescence method, using a microscope that focuses few mW of the second harmonic of a CW Nd:Yag laser onto the ruby chip and collects the fluorescence in a back scattering geometry.

## 4.2 Raman

Raman measurements were performed using a custom setup especially designed to have high spatial resolution in the diamond anvil cell. The setup is sketched in figure 4.1. The 641.7 nm emission line from a continuous wave  $\text{Kr}^+$  laser (Innova 300 by Coherent) is used as exciting source. A telescope is used to expand the beam that is sent to a 50/50 beam splitter. The reflected part is sent onto the sample contained in a diamond anvil cell, focused by a 20X microscope objective. The same microscope objective collects the signal in a back-scattering geometry that is sent back through the beam splitter. The expanded beam combined to the short focal length of the microscope objective are able to guarantee a beam waste in the focal plane of less than  $3\text{ }\mu\text{m}$  and a Rayleigh range in the order of few tens of  $\mu\text{m}$ . A spatial filter constituted by two confocal convex lenses of same focal length and a  $25\text{ }\mu\text{m}$  pin-hole placed in the focus point, is present before the revelation with the purpose of further reducing the effective depth of field and the active diameter of the collecting system. In this way a spatial resolution in the order of  $1\text{ }\mu\text{m}$  is achieved on the focal plane with a depth of field of less than  $20\text{ }\mu\text{m}$ , fundamental for gaining spatial resolution and thus avoid the strong Raman diamond signal from the windows. The collected radiation is then filtered by two distinct notch filters to avoid any residue of the excitation wavelength and focused onto the slit of the last stage of a triple stage monochromator equipped by a set of three gratings (300, 900 and 1800 grooves/mm) giving a maximum spectral resolution of  $0.7\text{ cm}^{-1}$ . The notch filter has a large rejection band, covering Raman shifts up to  $200\text{ cm}^{-1}$ . To analyse the frequency region typical of the lattice phonons at lower frequencies the collected signal is sent after the spatial filter to the first stage of the triple stage monochromator that is used in a subtractive way, allowing to perform measurements up to Raman shift of  $20\text{ cm}^{-1}$ . The signal is then analysed by means of a  $1024 \times 1024$  pixel liquid nitrogen cooled CCD placed on the exit of the third monochromator stage. The sample holder is provided with motorised micrometric movements allowing fine translations

on the focal plane of the sample with a precision of  $1\ \mu\text{m}$  that is software controlled, allowing automatic measurements and spatial sampling.

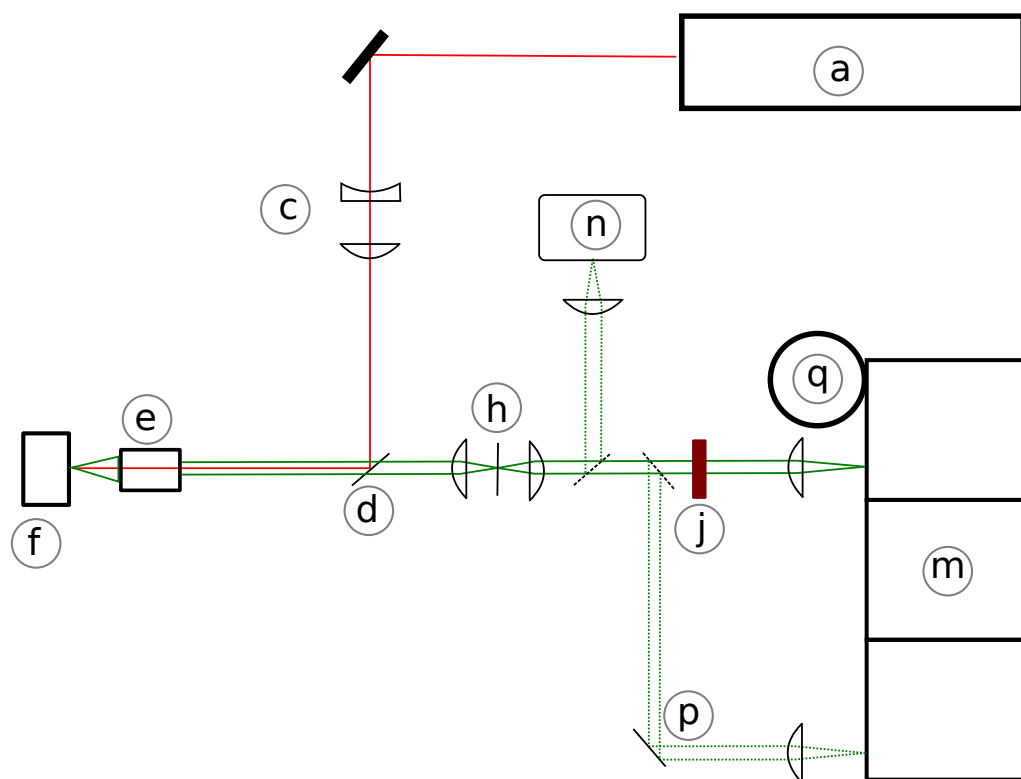


**Figure 4.1:** Raman setup: a) continuous wave Kr<sup>+</sup> laser; c) beam expander; d) beam splitter; e) microscope objective; f) diamond anvil cell; h) spatial filter; n) video camera; p) triple stage line; j) notch filter and single stage line; m) monochromator; q) CCD.

### 4.3 Two photon induced fluorescence

The two photon excitation profiles and fluorescence spectra reported in this work were recorded using the setup presented in the following. The excitation source was an optical parametric generator (PG401 from EKSPLA) pumped by the third harmonic at 355 nm of a Nd:YAG pulsed laser (PL2143A from EKSPLA) that has a pulse duration of 21 ps and a repetition rate of 10 Hz. The energy output of the optical parametric oscillator in the visible range as a function of the wavelength is reported in figure 4.2. The OPG output is then filtered to obtain a final energy onto the sample ranging from few hundreds of nJ to tens of  $\mu$ J by means of beam splitters and neutral optical density filters. A beam sampler reflects about 3% of the beam onto a silicon photodiode (S1722-02 by Hamamatsu) used for the fluorescence signal normalisation. The beam is focused onto the sample in the diamond anvil cell by means of an achromatic doublet with a focal length of 100 mm through a pierced parabolic mirror. The parabolic mirror with a focal length of 50 mm collects the emission from the sample in a back-scattering geometry that is sent to a single stage monochromator using an holographic grating with 2400 grooves/mm. Optical long pass filters were used in front of the monochromator to cut the residual excitation beam. The emission, depending on the spectral range, was then analysed by means of a Electron Tubes 9235QB photomultiplier in the 250-450 nm range, or by a cooled Hamamatsu R943-02 photomultiplier in the 400-900 nm range. The fluorescence spectra are always recorded using a fixed excitation wavelength and analysing the emission intensity as a function of the revelation wavelength. By properly setting the exit slit on the monochromator the resolution of the fluorescence spectra can be decided. Because of the broad nature of the emissions typical of the sample here presented, all the reported fluorescence spectra were recorded with a spectral resolution of 1 nm as a better resolution is not required. The excitation profiles were reconstructed detecting the fluorescence around its maximum as a function of the excitation wavelength. The spectral width of the excitation line is about

0.1 nm in the whole visible range, corresponding to the maximum resolution achievable with this setup. As the absorption spectra of the analysed compounds have not narrower features, we sampled all the excitation profiles in steps of 1 nm. The excitation profile is a good approximation to the absorption spectrum of the compound if the fluorescence quantum yield is independent of the excitation wavelength and all the fluorescence is relaxed, meaning that correspond to the  $S_1 \rightarrow S_0$  electronic transition. The two photon absorption mechanism is always verified by checking the quadratic dependency of the emission signal on the excitation energy. A sketch of the setup is presented in figure 4.3

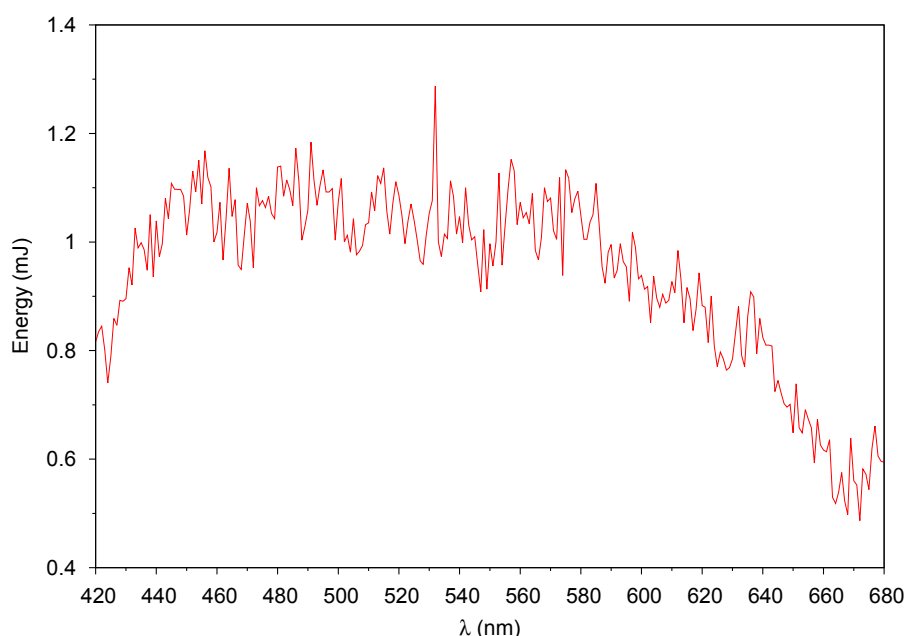


**Figure 4.2:** Energy output as a function of the wavelength of the EKSPLA PG401 measured with a Gentec Electro Optics QE25LP-S-MB energy meter

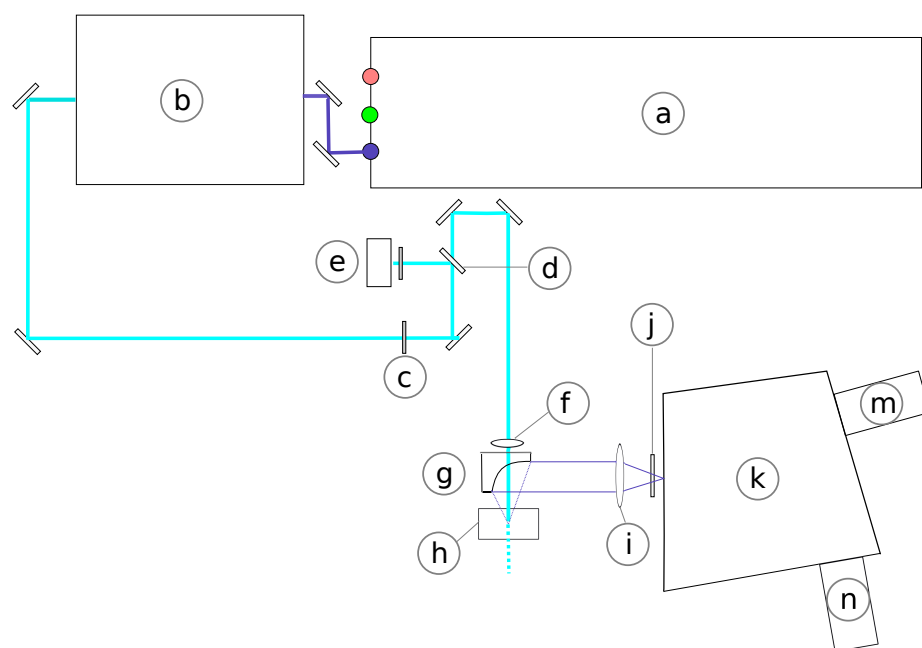


**Figure 4.3:** Sketch of the pulsed two photon induced fluorescence setup. a) Pulsed Nd:YAG laser; b) optical parametric generator; c) neutral optical density filters; d) beam sampler; e) silicon photodiode; f) achromatic lens,  $F=100$  mm; g) pierced parabolic mirror; h) diamond anvil cell; i) collecting lens; j) coloured filter; k) monochromator; m), n) photomultipliers .

## 4.4 Femtosecond transient IR (TRIR)

Mid-IR pump-probe experiments were performed by using the setup described in the following. The laser source is based on a Ti:sapphire oscillator (Micra by Coherent) and a regenerative amplifier (Legend Elite by Coherent), and it produces pulses with duration of about 35 fs with a repetition rate of 1 KHz and a maximum energy of 3 mJ. The output of the laser is used to pump two independent frequency optical parametric amplifiers, generating respectively the pump and the couple of probe/reference pulses, whose frequency is tunable in a wide spectral range of near and medium infrared. In details, the energetic pump beam centred around  $4\ \mu\text{m}$  ( $2500\ \text{cm}^{-1}$ ) is generated by a commercial optical parametric amplifier (TOPAS-800 by Light Conversion) that produces pulses of duration of 70 fs and energy up to  $6\ \mu\text{J}$ . The probe and reference beams are generated by an home made optical parametric amplifier that gives spectrally broad pulses of 80 fs of duration and an energy up to  $6\ \mu\text{J}$ . The medium infrared pulses are obtained in two steps. First, by optical parametric amplification in a type II BBO crystal ( $\beta\text{BaB}_2\text{O}_5$ ) seeded by filament white light, the 800 nm from the laser is converted into near infrared signal and idler pulses, whose wavelength is tunable from 1.2 up to  $2.4\ \mu\text{m}$ . The seeding white light is generated by focusing a portion of about 4% of the amplified 800 nm pulses into a sapphire plate that is recombined with half of the remaining energy of the 800 nm beam in the BBO crystal for the first generation step. Then, it is recombined with the remaining energy of the 800 nm pump beam for a second amplification passage in the BBO crystal. In the second step of light conversion, signal and idler coming from the amplification step are separated by dichroic mirrors and recombined into an  $\text{AgGaS}_2$  crystal to obtain medium infrared pulses by difference-frequency generation, giving a spectrum that can be tuned from 3 to  $10\ \mu\text{m}$ . An example of spectrum of the probe employed in our experiments and centred at  $\sim 4.1\ \mu\text{m}$  is reported in figure 4.4.

The pump beam generated by the TOPAS is then delayed through a con-



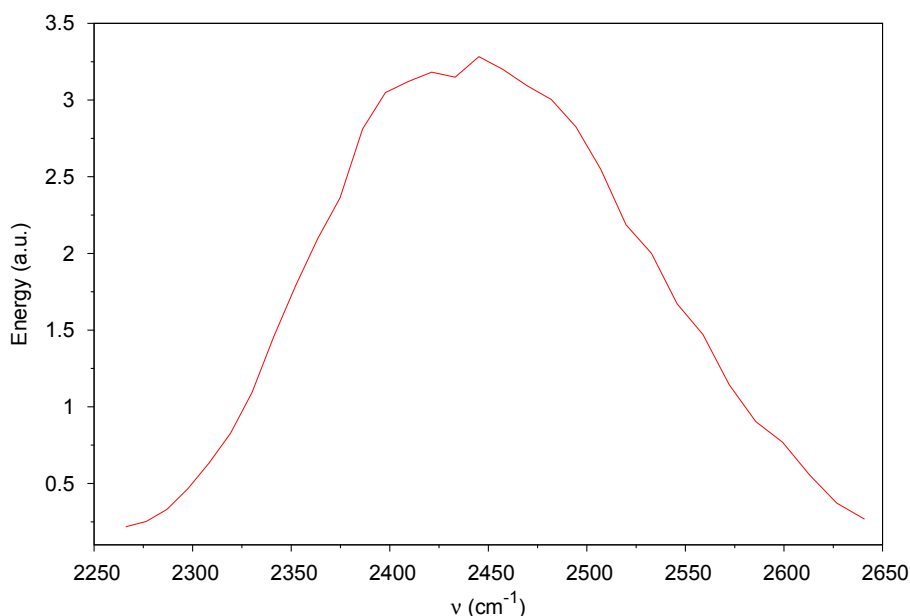


**Figure 4.4:** Spectrum of the probe pulse employed for the measures presented in this work centred in the region of the OD stretching mode.

trolled motorised stage and then overlapped to the probe onto the sample contained in the sapphire anvil cell. The beams are focused onto the sample and then collected by means of a couple of identical parabolic gold mirrors with focal length of 100 mm, assuring a minimum frequency dispersion and a beam waist comparable to the sample dimensions (less than  $400\ \mu\text{m}$ ) to avoid scattering from the gasket. In our setup, because of the little dimension of the sample, the reference beams used as energy normalisation passes outside the sample. Before the delay stage the polarisation of pump beam is controlled using a waveplate, allowing to perform measures in different pump and probe relative polarisation. A chopper synchronised at 0.5 KHz is placed on the pump beam allowing the measure of the probe and reference intensity in absence of the pump. After the sample, both probe and reference pulses are spectrally dispersed in a spectrometer (TRIAX 180 by Jobin Yvon) and imaged separately on a double 32-channel liquid nitrogen cooled MCT detector (InfraRed Associated Inc.) providing a resolution of  $13\ \text{cm}^{-1}$ . The setup of the sample chamber is reported in figure 4.5.

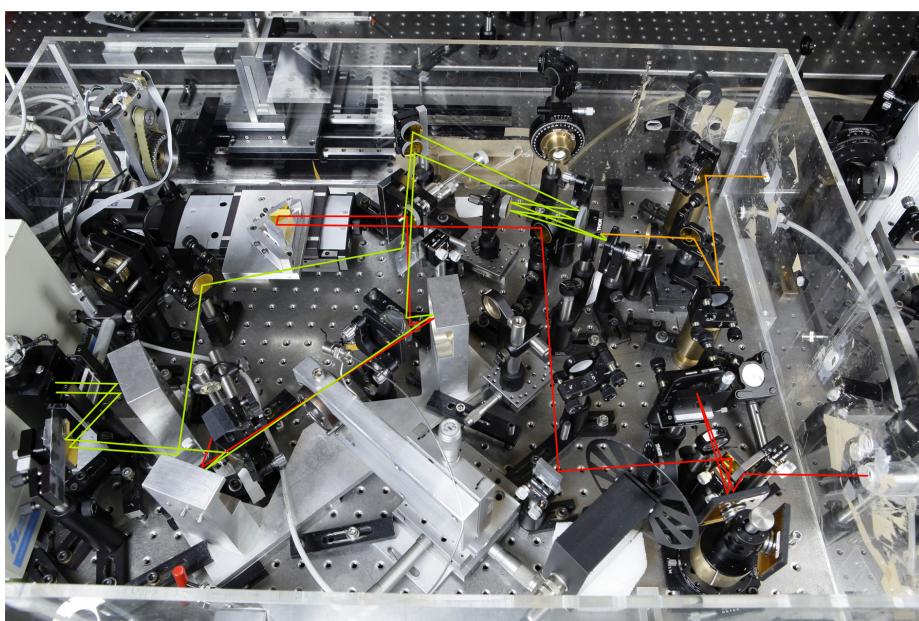


**Figure 4.5:** Photograph of the setup for transient absorption measures presented in this work. The output of the home made OPA is here reported in orange, from which the probe and reference beams are obtained (reported in yellow). The TOPAS output, that is used as pump, is reported in red.

# Conclusions

The application of an external pressure is shown to be a powerful method to tune the dynamics, the structural and electronic properties and the reactivity of molecular systems, that can be drastically modified from room conditions up to achieve properties that are peculiar of the dense state. The application of state of art frequency and time resolved spectroscopic techniques presented in this work in a perfect synergy with the technology of ultra-high pressure devices to access the GPa range of pressure, is demonstrated to be very reliable in the description of the aforementioned phenomena. Within them, the two photon induced fluorescence spectroscopy using pulses in the picosecond scale and the time-resolved transient infrared spectroscopy in the femtosecond time-scale, the latter applied here to high pressure studies for the first time, have to be mentioned for the very remarkable information that are able to provide, concerning the electronic structure and the ultra-fast dynamics, respectively.

It is shown how the pressure can be effective in the modification of both the electronic properties and the crystalline structure of molecules possibly implying huge consequences on the reactivity. The well known case of benzene is reported as typical example and the extension to other aromatic and etheroaromatic systems is presented demonstrating how concept extracted from the benzene study have general character and can be successfully applied to the studies of other systems. Among them, pyridine is a good example of molecular crystal which has a rich high pressure phase diagram. It is shown

how the pressure and temperature conditions can affect the crystal structure and how it is possible to identify the phase transitions by means of FT-IR and Raman spectroscopy. Pyridine is also a very peculiar system because of its characteristic low fluorescence quantum yield, being generally known as a fluorescence quencher. It is shown how the peculiar interactions in the high pressure phases of pyridine can induce deep modifications of the electronic properties determining an enhancement of the fluorescence quantum yield of more than five orders of magnitude at high pressure, possibly because of an energy inversion of  $n\pi^*$  and  $\pi\pi^*$  electronic states sequence. By means of the aforementioned two photon induced fluorescence technique we unveil a non-structural excimer in the pyridine phase II, and applying the knowledge acquired from the benzene case we demonstrate its implication in the reactivity. As the pyridine phase II does not allow the formation of structural excimers preceding the reaction seeds, they can form only at structural defects, thus the pressure threshold of the reaction is not reproducible greatly depending on the crystal quality. Moreover the reaction cannot be quantitative because of the molecular hindering induced by strong hydrogen bond interactions.

Picene and s-triazine are also good examples of the strong modifications of the electronic structure induced by pressure. The frontier molecular orbitals of triazine have respectively non-bonding (HOMO) and  $\pi^*$  (LUMO) character, whereas the  $\pi$  molecular orbital lies at lower energy. By means of the two photon induced fluorescence technique we evidenced a huge relative destabilisation of the  $\pi$  molecular orbital with increasing pressure. The destabilisation is so large, that at pressures in the order of 10 GPa the energy of the  $\pi$  molecular orbital is similar to the non-bonding orbital, meaning that the aromatic stabilisation is deeply reduced and as a consequence the molecular crystal rearranges to an amorphous extended compound. We were able to assign the lowest energy HOMO-LUMO electronic transitions in the single molecule and in the crystal of picene by performing absorption and fluorescence measurement on different solutions and solids of different crystalline qualities. In addition the electronic features of the crystal can be attributed considering that

the molecule identity is maintained. The behaviour observed in the picene crystal is drastically different with respect to s-triazine as the first electronic excited state is deeply red-shifted with increasing pressure, while the higher energy electronic states, including their vibronic structure which is well resolved up to the higher pressure achieved, are almost unaffected. The effect is so macroscopic being about 0.05 eV/GPa, that picene crystal, that is colourless at room condition, becomes of an intense red colour on compression. Anyway the gap closure determining the metallisation, that is predicted by extrapolation of our data to occur at a pressure of about 64 GPa, is prevented by a chemical reaction that takes place at about 23.5 GPa, leading to an amorphous hydrogenated carbon similar to the product of high pressure reaction of benzene, but richer in unsaturated carbon.

The experiments conducted on the photoinduced reactivity of simple alcohol allowed us to draw important conclusions on the pressure effect on the electronic state of the R–OH systems, possibly including water. Such knowledge was attained by a careful analysis of the reaction kinetics, the identification of the reaction products and the rationalisation of the reactive mechanisms along different channels, comparing two ethanol and two methanol isotopomers. This was done by using FT–IR spectroscopy which gives detailed information on the molecule fingerprint, thus being a reliable identification method. In addition, the integrated area of the infrared bands are directly correlated to the quantity of the absorbing species in the optical path, thus offering a quantitative method for probing the reaction. Raman spectroscopy is also used as identification tool. We demonstrated that the effect of the external pressure in the range of the GPa is able to change the character of the first electronic excited state of simple alcohols, that from being dissociative along the O–H coordinate at room conditions becomes weakly bonding at high density. Indeed, this is the only evidence of a minimum created and deepened by the increasing pressure on an excited electronic surface of a simple molecule.

The application of ultrafast time resolved techniques to the study of fast dynamics at high pressure is probably the most original contribution of this work. We demonstrated how the application of these techniques can be reliable for the characterisation of the sub-picosecond dynamics of molecular systems and how they are affected by pressure. For the first time we applied the pump-probe transient medium-infrared pump-probe spectroscopy to compressed water analysing the effect of the high density conditions on the rotational and vibrational dynamics of the water molecule. The whole study was aided by classical molecular dynamics performed using a new polarisable potential especially designed for the prediction of structural properties of water in extreme conditions and by careful infrared study about frequency and linewidth of the water stretching mode, in a wide range of temperature and pressure. We found two different regimes splitting in two the pressure and temperature range of the liquid water in the phase diagram. The low density regime (low temperature and low pressure) is characterised by a vibrational lifetime which is almost insensitive to the rising pressure while the rotational lifetime is deeply reduced being the rotation accelerated. In liquid water the rotation is not free, needing the breaking and reformation of hydrogen bonds to be accomplished. We demonstrated that the insertion of the second shell molecules into the interstitial sites of the first tetrahedral coordination shell induced by the increasing pressure is the key to understand the effect on the rotational dynamics. Changing the density regime, there is no more effect on the rotational dynamics that has reached a limit speed and it is no more affected by further compression. Indeed it is shown that on rising density the first coordination shell is almost unaffected while the second shell collapses onto the first one. As the probability of occupation of the interstitial sites is enhanced, the mechanism of breaking and reformation of an hydrogen bond involving one of those molecules and determining a switch of molecules from the two shells is favoured. As a direct consequence the rotation is accelerated, up to a limit speed corresponding to a limit structural configuration in which statistically there is always a second shell molecule in an interstitial site at the

right distance to form an hydrogen bond with the central molecule. In the same density range the vibrational lifetime starts to be affected by the pressure probably because of a modification induced on the molecular density of states.

The development of the application of ultrafast techniques to samples compressed in ultra-high pressure devices will be carried on as a future perspective, since we have demonstrated the reliability of these techniques in unveiling the effect of high density on the molecular dynamics. Possible future applications span from the identification of fast structural dynamics of pure fluids, solutions, crystals, but also of short living reaction intermediates or how energy transfer processes are affected by pressure, thus opening impressively large perspectives for the development of high pressure studies. As a matter of fact, no information is presently available on these issues and several different scientific communities will benefit of these studies. In greater detail we can think of additional studies of liquid water by other ultrafast techniques directed for example to the understanding of the hydrogen bond dynamics, a topic of extreme interest also in biology because water represents the fluid central for life. The effect of pressure on the hydrogen bond dynamics can be studied by means of bi-dimensional infrared pump-probe spectroscopy, a technique able to provide information on the dynamics of the intermolecular interactions. This spectroscopy has never been applied in conjunction with high pressure devices, which represents in itself an experimental breakthrough. Moreover, the chemistry and the physics of water solutions in high pressure conditions are of extreme geological interest being involved in many processes at the low crustal level and in the upper mantle, like the carbonate transportation and transformation from the sea level down to the mantle. These processes represent one of the most important elements in the Earth carbon cycle. The characterisation of the pressure and temperature dependence of the aforementioned fast dynamics in carbonate solutions, for instance, can be able to provide useful information for understanding such geological phenomena.

The access to the fast dynamics regulating the thermalization of electronic excited states could provide valuable information about the response to pressure of the electronic structure, an almost unexplored field mandatory to have access to the mechanisms regulating the purely pressure induced or high-pressure photo-assisted reactions. This knowledge adds to the crystal dynamics control for the exploration of entirely new synthetic methods.



## List of publications

1. M. Ceppatelli, S. Fanetti, M. Citroni, and R. Bini, "Photoinduced reactivity of liquid ethanol at high pressure," *J. Phys. Chem. B*, vol. 114, no. 47, p. 15437, 2010.
2. S. Fanetti, M. Citroni, and R. Bini, "Structure and reactivity of pyridine crystal under pressure," *J. Chem. Phys.*, vol. 134, no. 20, p. 204504, 2011.
3. S. Fanetti, M. Citroni, and R. Bini, "Pressure-induced fluorescence of pyridine," *J. Phys. Chem. B*, vol. 115, no. 42, p. 12051, 2011.
4. S. Fanetti, M. Ceppatelli, M. Citroni, and R. Bini, "Changing the dissociative character of the lowest excited state of ethanol by pressure," *J. Phys. Chem. B*, vol. 115, no. 51, p. 15236, 2011.
5. S. Fanetti, M. Ceppatelli, M. Citroni, and R. Bini, "High-pressure photoinduced reactivity of  $\text{CH}_3\text{OH}$  and  $\text{CD}_3\text{OH}$ ," *J. Phys. Chem. C*, vol. 116, no. 3, p. 2108, 2012.
6. S. Fanetti, M. Citroni, R. Bini, L. Malavasi, G. A. Artioli, and P. Postorino, "HOMO-LUMO transitions in solvated and crystalline picene," *J. Chem. Phys.*, vol. 137, no. 22, p. 224506, 2012.

7. S. Fanetti, M. Citroni, L. Malavasi, G. A. Artioli, P. Postorino, and R. Bini, "High-pressure optical properties and chemical stability of picene," *J. Phys. Chem. C*, vol. 117, no. 10, p. 5343, 2013.
8. M. Ceppatelli, S. Fanetti, and R. Bini, "Photoinduced reactivity of red phosphorus and ethanol at high pressure," *J. Phys. Chem. C*, vol. 117, no. 25, p. 13129, 2013.
9. S. Sciortino, F. Brandi, R. Carzino, M. Citroni, A. De Sio, S. Fanetti, S. Lagomarsino, E. Pace, G. Parrini, D. Passeri, A. Scorzoni, L. Servoli, and L. Tozzetti, "Electrical properties of laser-bonded silicon-on-diamond samples," *Nucl. Instrum. Meth. A*, DOI:10.1016/j.nima.2013.06.069, 2013.
10. S. Fanetti, A. Lapini, M. Pagliai, M. Citroni, M. Di Donato, S. Scandolo, R. Righini, R. Bini "Structure and dynamics of low-density and high-density liquid water at high pressure" *J. Phys. Chem. Lett.*, accepted.

# Bibliography

- [1] R. Bini and V. Schettino, *Materials Under Extreme Conditions - Molecular Crystals at High Pressure*. Imperial College Press, 2013.
- [2] V. Schettino, R. Bini, M. Ceppatelli, L. Ciabini, and M. Citroni, *Chemical Reactions at Very High Pressure*. John Wiley & Sons, Inc., 2005.
- [3] J. Bernstein, *Polymorphism in Molecular Crystals*. Oxford: Oxford University Press, 2002.
- [4] R. Parr and W. Yang, *Density-Functional Theory of Atoms and molecules*. New York: Oxford Science Publications, 1989.
- [5] H. G. Drickamer and C. W. Frank, *Electronic Transitions and the High Pressure Chemistry and Physics of Solids*. London: Chapman and Hall, 1973.
- [6] H. G. Drickamer, C. W. Frank, and C. P. Slichter, "Optical versus thermal transitions in solids at high pressure," *Proc. Natl. Acad. Sci. USA*, vol. 69, no. 4, p. 933, 1972.
- [7] R. L. Mills, B. Olinger, and D. T. Cromer, "Structures and phase diagrams of N<sub>2</sub> and CO to 13 GPa by x-ray diffraction," *J. Chem. Phys.*, vol. 84, no. 5, p. 2837, 1986.
- [8] S. Mitra, *High Pressure Geochemistry and Mineral Physics*. Amsterdam: Elsevier, 2004.

- [9] R. Hazen, *The Diamond Makers*. Cambridge: Cambridge University Press, 1999.
- [10] M. D. Cohen and G. M. J. Schmidt, "Topochemistry. Part I. A survey," *J. Chem. Soc.*, p. 1996, 1964.
- [11] M. D. Cohen, "The photochemistry of organic solids," *Angew. Chem. Int. Ed.*, vol. 14, no. 6, p. 386, 1975.
- [12] K. Dwarakanath and P. N. Prasad, "Raman phonon spectroscopy of solid-state reactions: thermal rearrangement of methyl p-dimethylaminobenzenesulfonate in solid state," *J. Am. Chem. Soc.*, vol. 102, no. 12, p. 4254, 1980.
- [13] D. Chelazzi, M. Ceppatelli, M. Santoro, R. Bini, and V. Schettino, "High-pressure synthesis of crystalline polyethylene using optical catalysis," *Nat. Mat.*, vol. 3, no. 7, p. 470, 2004.
- [14] D. Chelazzi, M. Ceppatelli, M. Santoro, R. Bini, and V. Schettino, "Pressure-induced polymerization in solid ethylene," *J. Phys. Chem. B*, vol. 109, no. 46, p. 21658, 2005.
- [15] M. Citroni, M. Ceppatelli, R. Bini, and V. Schettino, "Laser-induced selectivity for dimerization versus polymerization of butadiene under pressure," *Science*, vol. 295, no. 5562, p. 2058, 2002.
- [16] M. Ceppatelli, R. Bini, and V. Schettino, "High-pressure reactivity of model hydrocarbons driven by near-UV photodissociation of water," *J. Phys. Chem. B*, vol. 113, no. 44, p. 14640, 2009.
- [17] M. Ceppatelli, R. Bini, and V. Schettino, "High-pressure photodissociation of water as a tool for hydrogen synthesis and fundamental chemistry," *Proc. Natl. Acad. Sci. USA*, vol. 106, no. 28, p. 11454, 2009.
- [18] T. Elsaesser and H. Bakker, *Ultrafast Hydrogen Bonding Dynamics and Proton Transfer Processes in the Condensed Phase*. Understanding Chemical Reactivity, Springer, 2010.

- [19] L. Ciabini, M. Santoro, F. A. Gorelli, R. Bini, V. Schettino, and S. Rauegi, "Triggering dynamics of the high-pressure benzene amorphization," *Nat. Mat.*, vol. 6, no. 1, p. 39, 2007.
- [20] M. Citroni, R. Bini, P. Foggi, and V. Schettino, "Role of excited electronic states in the high-pressure amorphization of benzene," *Proc. Natl. Acad. Sci. USA*, vol. 105, no. 22, p. 7658, 2008.
- [21] F. Cansell, D. Fabre, and J.-P. Petitet, "Phase transitions and chemical transformations of benzene up to 550°C and 30 GPa," *J. Chem. Phys.*, vol. 99, no. 10, p. 7300, 1993.
- [22] L. Ciabini, M. Santoro, R. Bini, and V. Schettino, "High pressure reactivity of solid benzene probed by infrared spectroscopy," *J. Chem. Phys.*, vol. 116, no. 7, p. 2928, 2002.
- [23] L. Ciabini, F. A. Gorelli, M. Santoro, R. Bini, V. Schettino, and M. Mezouar, "High-pressure and high-temperature equation of state and phase diagram of solid benzene," *Phys. Rev. B*, vol. 72, p. 094108, 2005.
- [24] L. Ciabini, M. Santoro, R. Bini, and V. Schettino, "High pressure photoinduced ring opening of benzene," *Phys. Rev. Lett.*, vol. 88, p. 085505, 2002.
- [25] B. Stevens, "Some effects of molecular orientation on fluorescence emission and energy transfer in crystalline aromatic hydrocarbons," *Spectrochim. Acta*, vol. 18, no. 4, p. 439, 1962.
- [26] H. W. Offen, "Fluorescence spectra of several aromatic crystals under high pressures," *J. Chem. Phys.*, vol. 44, no. 2, p. 699, 1966.
- [27] P. F. Jones and M. Nicol, "Excimer emission of naphthalene, anthracene, and phenanthrene crystals produced by very high pressures," *J. Chem. Phys.*, vol. 48, no. 12, p. 5440, 1968.

- [28] A. Brillante, R. Della Valle, R. Farina, and E. Venuti, "Pressure-induced phase-transitions in 9,10-anthracene derivatives - anthraquinone," *Chem. Phys.*, vol. 191, no. 1-3, p. 177, 1995.
- [29] Z. A. Dreger, H. Lucas, and Y. M. Gupta, "High-pressure effects on fluorescence of anthracene crystals," *J. Phys. Chem. B*, vol. 107, no. 35, p. 9268, 2003.
- [30] J. A. Joule and K. Mills, *Heterocyclic Chemistry*. Blackwell Publishing Ltd, 2010.
- [31] K. K. Zhuravlev, K. Traikov, Z. Dong, S. Xie, Y. Song, and Z. Liu, "Raman and infrared spectroscopy of pyridine under high pressure," *Phys. Rev.B*, vol. 82, no. 6, 2010.
- [32] S. Fanetti, M. Citroni, and R. Bini, "Structure and reactivity of pyridine crystal under pressure," *J. Chem. Phys.*, vol. 134, no. 20, p. 204504, 2011.
- [33] A. Heyns and M. Venter, "Effect of pressure on the Raman-spectra of solids .2. Pyridine," *J. Phys. Chem.*, vol. 89, no. 21, p. 4546, 1985.
- [34] M. Podsiadlo, K. Jakobek, and A. Katrusiak, "Density, freezing and molecular aggregation in pyridazine, pyridine and benzene," *Cryst. Eng. Comm.*, vol. 12, no. 9, p. 2561, 2010.
- [35] S. Crawford, M. T. Kirchner, D. Blaeser, R. Boese, W. I. F. David, A. Dawson, A. Gehrke, R. M. Ibberson, W. G. Marshall, S. Parsons, and O. Yamamuro, "Isotopic Polymorphism in Pyridine," *Angew. Chem.*, vol. 48, no. 4, p. 755, 2009.
- [36] D. Mootz and H. Wussow, "Crystal structures of pyridine and pyridine trihydrate," *J. Chem. Phys.*, vol. 75, no. 3, p. 1517, 1981.
- [37] A. Gavezzotti, *Molecular aggregation: structure analysis and molecular simulation of crystals and liquids*. Oxford: Oxford University Press, 2007.

- 
- [38] A. Anghel, G. Day, and S. Price, "A study of the known and hypothetical crystal structures of pyridine: why are there four molecules in the asymmetric unit cell?," *Cryst. Eng. Comm.*, p. 348, 2002.
- [39] M. C. C. Ribeiro, "Correlation between quasielastic Raman scattering and configurational entropy in an ionic liquid," *J. Phys. Chem. B*, vol. 111, no. 18, p. 5008, 2007.
- [40] M. C. C. Ribeiro, "Low-frequency Raman spectra and fragility of imidazolium ionic liquids," *J. Chem. Phys.*, vol. 133, no. 2, p. 024503, 2010.
- [41] T. Yasuzuka, K. Komatsu, and H. Kagi, "A Revisit to High-pressure Transitions of Pyridine: A New Phase Transition at 5 GPa and Formation of a Crystalline Phase over 20 GPa," *Chem. Lett.*, vol. 40, no. 7, p. 733, 2011.
- [42] E. Castellucci, G. Sbrana, and F. D. Verderame, "Infrared spectra of crystalline and matrix isolated pyridine and pyridine-d<sub>5</sub>," *J. Chem. Phys.*, vol. 51, no. 9, p. 3762, 1969.
- [43] R. Boese and S. Parsons. Private communication, 2011.
- [44] P. R. Salvi, P. Foggi, R. Bini, and E. Castellucci, "The two photon spectrum of liquid pyridine by thermal lensing techniques," *Chem. Phys. Lett.*, vol. 141, no. 5, p. 417, 1987.
- [45] Z.-L. Cai and J. R. Reimers, "The low-lying excited states of pyridine," *J. Phys. Chem. A*, vol. 104, no. 36, p. 8389, 2000.
- [46] I. Yamazaki and H. Baba, "Observation of fluorescence of pyridine in the vapor phase," *J. Chem. Phys.*, vol. 66, no. 12, p. 5826, 1977.
- [47] B. Valeur, *Molecular fluorescence: principles and applications*. Weinheim: Wiley-VCH, 2002.
- [48] E. Villa, A. Amirav, and E. C. Lim, "Single-vibronic-level and excitation-energy dependence of radiative and nonradiative transitions in jet-cooled S<sub>1</sub> pyridine," *J. Phys. Chem.*, vol. 92, no. 19, p. 5393, 1988.
-

- [49] M. A. El-Sayed, "Triplet state. Its radiative and nonradiative properties," *Acc. Chem. Res.*, vol. 1, no. 1, p. 8, 1968.
- [50] S. Fanetti, M. Citroni, and R. Bini, "Pressure-induced fluorescence of pyridine," *J. Phys. Chem. B*, vol. 115, no. 42, p. 12051, 2011.
- [51] T. Handa, Y. Utena, H. Yajima, T. Ishii, and H. Morita, "Excimer emission in protonated pyridine systems. 1. Fluorescence spectroscopy of protonated pyridine and its methyl derivatives in rigid glass solution at 77 K," *J. Phys. Chem.*, vol. 90, no. 12, p. 2589, 1986.
- [52] Z. Yoshida and T. Kobayashi, "Electronic spectra and structure of organic  $\pi$ -systems," *Theoret. Chim. Acta*, vol. 20, p. 216, 1971.
- [53] H. G. Drickamer, "High pressure studies of molecular luminescence," *Annu. Rev. Phys. Chem.*, vol. 33, no. 1, p. 25, 1982.
- [54] S. J. Daunt, H. F. Shurvell, and L. Pazdernik, "The solid state vibrational spectra of s-triazine and s-triazine- $d_3$  and the monoclinic to rhombohedral phase transition," *J. Raman Spectr.*, vol. 4, no. 2, p. 205, 1975.
- [55] S. M. Prasad, A. I. M. Rae, A. W. Hewat, and G. S. Pawley, "The crystal structure of s-triazine at 5K," *J. Phys. C Solid State*, vol. 14, no. 31, p. L929, 1981.
- [56] M. T. Dove and P. J. S. Ewen, "A Raman-scattering study of the pressure-induced phase-transition in s-triazine," *J. Chem. Phys.*, vol. 82, no. 4, p. 2026, 1985.
- [57] E. B. Wilson, "The normal modes and frequencies of vibration of the regular plane hexagon model of the benzene molecule," *Phys. Rev.*, vol. 45, p. 706, 1934.
- [58] R. C. Hirt, F. Halverson, and R. G. Schmitt, "s-Triazine. II. The Near Ultraviolet Absorption Spectrum," *J. Chem. Phys.*, vol. 22, no. 6, p. 1148, 1954.



- 
- [59] F. Halverson and R. C. Hirt, "Near ultraviolet solution spectra of the diazines," *J. Chem. Phys.*, vol. 19, no. 6, p. 711, 1951.
- [60] G. Fischer and G. J. Small, "Jahn-Teller distortion of s-triazine in its lowest excited singlet state," *J. Chem. Phys.*, vol. 56, no. 12, p. 5934, 1972.
- [61] J. S. Brinen and L. Goodman, "Sequence and spacing of  $n \rightarrow \pi$  transitions in s-triazine," *J. Chem. Phys.*, vol. 31, no. 2, p. 482, 1959.
- [62] L. Goodman and R. W. Harrell, "Calculation of  $n \rightarrow \pi$  transition energies in n-heterocyclic molecules by a one-electron approximation," *J. Chem. Phys.*, vol. 30, no. 5, p. 1131, 1959.
- [63] J. D. Webb, K. M. Swift, and E. R. Bernstein, "Vibronic assignments and vibronic coupling in the  $^1E''$  state of sym-triazine by two photon spectroscopy," *J. Chem. Phys.*, vol. 73, no. 10, p. 4891, 1980.
- [64] N. Ohta and H. Baba, "An anomalous broad emission of s-triazine vapor," *Chem. Phys. Lett.*, vol. 106, no. 5, p. 382, 1984.
- [65] N. Ohta, O. Sekiguchi, and H. Baba, "Fluorescence polarization and intramolecular dynamics in  $S_1$  of pyrazine, pyrimidine, and s-triazine vapors," *J. Chem. Phys.*, vol. 88, no. 1, p. 68, 1988.
- [66] M. Heaven, T. Sears, V. E. Bondybey, and T. A. Miller, "The free jet cooled, laser induced fluorescence spectrum of sym-triazine," *J. Chem. Phys.*, vol. 75, no. 11, p. 5271, 1981.
- [67] G. Portella, J. Poater, J. M. Bofill, P. Alemany, and M. Solà, "Local aromaticity of [n]acenes, [n]phenacenes, and [n]helicenes ( $n = 19$ )," *J. Org. Chem.*, vol. 70, no. 7, p. 2509, 2005.
- [68] R. Mitsuhashi, Y. Suzuki, Y. Yamanari, H. Mitamura, T. Kambe, N. Ikeda, H. Okamoto, A. Fujiwara, M. Yamaji, N. Kawasaki, Y. Maniwa, and Y. Kubozono, "Superconductivity in alkali-metal-doped picene," *Nature*, vol. 464, no. 7285, p. 76, 2010.
-

- [69] M. Oehzelt, A. Aichholzer, R. Resel, G. Heimel, E. Venuti, and R. G. Della Valle, "Crystal structure of oligoacenes under high pressure," *Phys. Rev. B*, vol. 74, p. 104103, 2006.
- [70] T. Kambe, X. He, Y. Takahashi, Y. Yamanari, K. Teranishi, H. Mitamura, S. Shibasaki, K. Tomita, R. Eguchi, H. Goto, Y. Takabayashi, T. Kato, A. Fujiwara, T. Kariyado, H. Aoki, and Y. Kubozono, "Synthesis and physical properties of metal-doped picene solids," *Phys. Rev. B*, vol. 86, no. 21, 2012.
- [71] J. B. Gallivan and J. S. Brinen, "Polarization of electronic transitions of aromatic hydrocarbons," *J. Chem. Phys.*, vol. 50, no. 4, p. 1590, 1969.
- [72] J. R. Platt, "Classification of spectra of cata-condensed hydrocarbons," *J. Chem. Phys.*, vol. 17, no. 5, p. 484, 1949.
- [73] W. Moffitt, "The electronic spectra of cata-condensed hydrocarbons," *J. Chem. Phys.*, vol. 22, no. 2, p. 320, 1954.
- [74] S. Fanetti, M. Citroni, R. Bini, L. Malavasi, G. A. Artioli, and P. Postorino, "HOMO-LUMO transitions in solvated and crystalline picene," *J. Chem. Phys.*, vol. 137, no. 22, p. 224506, 2012.
- [75] S. Fanetti, M. Citroni, L. Malavasi, G. A. Artioli, P. Postorino, and R. Bini, "High-pressure optical properties and chemical stability of picene," *J. Phys. Chem. C*, vol. 117, no. 10, p. 5343, 2013.
- [76] M. Klessinger and J. Michl, *Excited States and photochemistry of organic molecules*. New York: Wiley-VCH, 1995.
- [77] M. Parac and S. Grimme, "A TDDFT study of the lowest excitation energies of polycyclic aromatic hydrocarbons," *Chem. Phys.*, vol. 292, no. 1, p. 11, 2003.
- [78] B. Joseph, L. Boeri, L. Malavasi, F. Capitani, G. A. Artioli, S. Protti, M. Fagnoni, A. Albini, C. Marini, L. Baldassarre, A. Perucchi, S. Lupi,

- P. Postorino, and P. Dore, "Vibrational spectrum of solid picene ( $C_{22}H_{14}$ )," *J. Phys. - Condens. Mat.*, vol. 24, no. 25, 2012.
- [79] A. Girlando, M. Masino, I. Bilotti, A. Brillante, R. G. Della Valle, and E. Venuti, "Phonon dynamics and electron-phonon coupling in pristine picene," *Phys. Chem. Chem. Phys.*, vol. 14, no. 5, p. 1694, 2012.
- [80] A. De, R. Ghosh, S. Roychowdhury, and P. Roychowdhury, "Structural-analysis of picene,  $C_{22}H_{14}$ ," *Acta Cryst. C*, vol. 41, p. 907, 1985.
- [81] J. B. Birks and L. G. Christophorou, "Excimer fluorescence. IV. solution spectra of polycyclic hydrocarbons," *Proceedings of the Royal Society of London. Series A. Mathematical and Physical Sciences*, vol. 277, no. 1371, p. 571, 1964.
- [82] M. Citroni, B. Costantini, R. Bini, and V. Schettino, "Crystalline indole at high pressure: Chemical stability, electronic, and vibrational properties," *J. Phys. Chem. B*, vol. 113, no. 41, p. 13526, 2009.
- [83] M. Ceppatelli, S. Fanetti, and R. Bini, "Photoinduced reactivity of red phosphorus and ethanol at high pressure," *J. Phys. Chem. C*, vol. 117, no. 25, p. 13129, 2013.
- [84] S. Satyapal, J. Park, R. Bersohn, and B. Katz, "Dissociation of methanol and ethanol activated by a chemical reaction or by light," *J. Chem. Phys.*, vol. 91, no. 11, p. 6873, 1989.
- [85] K. Xu, G. Amaral, and J. Zhang, "Photodissociation dynamics of ethanol at 193.3 nm: The H-atom channel and ethoxy vibrational distribution," *J. Chem. Phys.*, vol. 111, no. 14, p. 6271, 1999.
- [86] B.-M. Cheng, M. Bahou, W.-C. Chen, C. hui Yui, Y.-P. Lee, and L. C. Lee, "Experimental and theoretical studies on vacuum ultraviolet absorption cross sections and photodissociation of  $CH_3OH$ ,  $CH_3OD$ ,  $CD_3OH$ , and  $CD_3OD$ ," *J. Chem. Phys.*, vol. 117, no. 4, p. 1633, 2002.

- [87] R. Mota, R. Parafita, and A. Giuliani, "Water VUV electronic state spectroscopy by synchrotron radiation," *Chem. Phys. Lett.*, vol. 416, p. 152, 2005.
- [88] G. H. F. Dierksen, W. P. Kraemer, T. N. Rescigno, C. F. Bender, B. V. McKoy, S. R. Langhoff, and P. W. Langhoff, "Theoretical studies of photoexcitation and ionization in H<sub>2</sub>O," *J. Chem. Phys.*, vol. 76, no. 2, p. 1043, 1982.
- [89] J. Jung and H. Gress, "Single-photon absorption of liquid methanol and ethanol in the vacuum ultraviolet," *Chem. Phys. Lett.*, vol. 359, no. 12, p. 153, 2002.
- [90] M. Ceppatelli, S. Fanetti, M. Citroni, and R. Bini, "Photoinduced reactivity of liquid ethanol at high pressure," *J. Phys. Chem. B*, vol. 114, no. 47, p. 15437, 2010.
- [91] S. Fanetti, M. Ceppatelli, M. Citroni, and R. Bini, "Changing the dissociative character of the lowest excited state of ethanol by pressure," *J. Phys. Chem. B*, vol. 115, no. 51, p. 15236, 2011.
- [92] S. Fanetti, M. Ceppatelli, M. Citroni, and R. Bini, "High-Pressure Photoinduced Reactivity of CH<sub>3</sub>OH and CD<sub>3</sub>OH," *J. Phys. Chem. C*, vol. 116, no. 3, p. 2108, 2012.
- [93] S. B, *Raman/IR Atlas of Organic Compounds*. Weinheim: VCH-Verl.-Ges. 2 ed., 1989.
- [94] L. Ulivi, L. Zoppi, L. Gioè, and G. Pratesi, "Molecular hydrogen internuclear distance in high-pressure fluid and solid phases at room temperature," *Phys. Rev. B*, vol. 58, p. 2383, 1998.
- [95] S. Sharma, H. Mao, and P. Bell, "Raman measurement of hydrogen in the pressure range 0.2-630 Kbar at room temperature," *Phys. Rev. Lett.*, vol. 44, p. 886, 1980.

- [96] M. Lee and D. Benamotz, "Pressure-induced vibrational frequency-shifts of ethane and methyl iodide. Evidence for the formation of C–H hydrogen bonds in high-density fluids," *J. Chem. Phys.*, vol. 99, p. 10074, 1993.
- [97] F. Lin, J. Bodnar, and S. Becker, "Experimental determination of the Raman CH<sub>4</sub> symmetric stretching ( $\nu_1$ ) band position from 1-650 bar and 0.3-22 °C," *Geochim. Cosmochim. Ac.*, vol. 71, p. 3746, 2007.
- [98] P. Hebert, A. Polian, P. Loubeyre, and R. Le Toullec, "Optical studies of methane under high pressure.," *Phys. Rev. B*, vol. 36, p. 9196, 1987.
- [99] K. N. Jha and G. R. Freeman, "Effect of pressure on the rates of reaction of solvated electrons in liquid ethanol," *J. Chem. Phys.*, vol. 57, no. 4, p. 1408, 1972.
- [100] J. Bigeleisen and M. Goeppert-Mayer, "Calculation of equilibrium constants for isotopic exchange reactions," *J. Chem. Phys.*, vol. 15, no. 5, p. 261, 1947.
- [101] D. S. Bomse, S. Dougal, and R. L. Woodin, "Multiphoton ionization studies of IR multiphoton dissociation: direct carbon-hydrogen bond cleavage in methanol," *J. Phys. Chem.*, vol. 90, no. 12, p. 2640, 1986.
- [102] G. J. Piermarini, S. Block, and J. Barnett, "Hydrostatic limits in liquids and solids to 100 kbar," *J. Appl. Phys.*, vol. 44, no. 12, p. 5377, 1973.
- [103] D. C. Silverman and J. J. Freeman, "Associated species in vaporized methanol-formaldehyde solutions," *Ind. Eng. Chem. Proc. DD*, vol. 22, no. 3, p. 441, 1983.
- [104] W. Sawodny, K. Niedenzu, and J. Dawson, "The vibrational spectrum of ethylene glycol," *Spectr. Acta A*, vol. 23, no. 4, p. 799, 1967.
- [105] R. Wrobel, W. Sander, E. Kraka, and D. Cremer, "Reactions of dimethyl ether with atomic oxygen: a matrix isolation and a quantum chemical study," *J. Phys. Chem. A*, vol. 103, no. 19, p. 3693, 1999.

- [106] H. Susi and J. R. Schecker, "The normal vibrations of formic acid and methyl formate," *Spectr. Acta A*, vol. 25, no. 7, p. 1243, 1969.
- [107] J. K. Wilmshurst and H. J. Bernstein, "The infrared spectra of CH<sub>4</sub>, CH<sub>3</sub>D, CH<sub>2</sub>D<sub>2</sub>, CD<sub>3</sub>H, and CD<sub>4</sub>," *Can. J. Chem.*, vol. 35, no. 3, p. 226, 1957.
- [108] F. Franks, *Water, a Comprehensive Treatise*. New York: Plenum Press, 1972-1982.
- [109] F. Mallamace, "The liquid water polymorphism," *Proc. Natl. Acad. Sci. USA*, vol. 106, no. 36, p. 15097, 2009.
- [110] R. J. Speedy, "Stability-limit conjecture. An interpretation of the properties of water," *J. Phys. Chem.*, vol. 86, no. 6, p. 982, 1982.
- [111] R. J. Speedy and C. A. Angell, "Isothermal compressibility of supercooled water and evidence for a thermodynamic singularity at 45°C," *J. Chem. Phys.*, vol. 65, no. 3, p. 851, 1976.
- [112] P. Poole, F. Sciortino, U. Essmann, and H. Stanley, "Phase-behavior of metastable water," *Nature*, vol. 360, no. 6402, p. 324, 1992.
- [113] A. Nilsson and L. G. M. Pettersson, "Perspective on the structure of liquid water," *Chem. Phys.*, vol. 389, no. 1-3, p. 1, 2011.
- [114] P. G. Debenedetti and H. E. Stanley, "Supercooled and glassy water," *Phys. Today*, vol. 56, no. 6, p. 40, 2003.
- [115] A. K. Soper, "Water and ice," *Science*, vol. 297, no. 5585, p. 1288, 2002.
- [116] S. Sastry, P. G. Debenedetti, F. Sciortino, and H. E. Stanley, "Singularity-free interpretation of the thermodynamics of supercooled water," *Phys. Rev. E*, vol. 53, no. 6, B, p. 6144, 1996.
- [117] C. A. Angell, "Insights into phases of liquid water from study of its unusual glass-forming properties," *Science*, vol. 319, no. 5863, p. 582, 2008.

- [118] D. Laage and J. T. Hynes, “A molecular jump mechanism of water reorientation,” *Science*, vol. 311, no. 5762, p. 832, 2006.
- [119] A. K. Soper and M. A. Ricci, “Structures of high-density and low-density water,” *Phys. Rev. Lett.*, vol. 84, no. 13, p. 2881, 2000.
- [120] C. Huang, K. T. Wikfeldt, T. Tokushima, D. Nordlund, Y. Harada, U. Bergmann, M. Niebuhr, T. M. Weiss, Y. Horikawa, M. Leetmaa, M. P. Ljungberg, O. Takahashi, A. Lenz, L. Ojamäe, A. P. Lyubartsev, S. Shin, L. G. M. Pettersson, and A. Nilsson, “The inhomogeneous structure of water at ambient conditions,” *Proc. Natl. Acad. Sci. USA*, vol. 106, no. 36, p. 15214, 2009.
- [121] A. M. Saitta and F. Datchi, “Structure and phase diagram of high-density water: The role of interstitial molecules,” *Phys. Rev. E*, vol. 67, p. 020201, 2003.
- [122] T. Strässle, A. M. Saitta, Y. Le Godec, G. Hamel, S. Klotz, J. S. Loveday, and R. J. Nelmes, “Structure of dense liquid water by neutron scattering to 6.5 GPa and 670 K,” *Phys. Rev. Lett.*, vol. 96, p. 067801, 2006.
- [123] M. Krisch, P. Loubeyre, G. Ruocco, F. Sette, A. Cunsolo, M. D’Astuto, R. LeToullec, M. Lorenzen, A. Mermet, G. Monaco, and R. Verbeni, “Pressure evolution of the high-frequency sound velocity in liquid water,” *Phys. Rev. Lett.*, vol. 89, p. 125502, 2002.
- [124] M. Santoro, F. A. Gorelli, T. Scopigno, M. Krisch, F. Sette, and G. Ruocco, “Pressure behavior of the sound velocity of liquid water at room temperature in the terahertz regime,” *Phys. Rev. B*, vol. 84, p. 092301, 2011.
- [125] F. Li, Q. Cui, Z. He, T. Cui, J. Zhang, Q. Zhou, G. Zou, and S. Sasaki, “High pressure-temperature brillouin study of liquid water: Evidence of the structural transition from low-density water to high-density water,” *J. Chem. Phys.*, vol. 123, p. 174511, 2005.

- [126] T. Kawamoto, S. Ochiai, and H. Kagi, "Changes in the structure of water deduced from the pressure dependence of the Raman OH frequency," *J. Chem. Phys.*, vol. 120, p. 5867, 2004.
- [127] H. J. Bakker and J. L. Skinner, "Vibrational spectroscopy as a probe of structure and dynamics in liquid water," *Chem. Rev.*, vol. 110, no. 3, p. 1498, 2010.
- [128] C. J. Fecko, J. D. Eaves, J. J. Loparo, A. Tokmakoff, and P. L. Geissler, "Ultrafast hydrogen-bond dynamics in the infrared spectroscopy of water," *Science*, vol. 301, p. 1698, 2003.
- [129] M. L. Cowan, B. D. Bruner, N. Huse, J. R. Dwyer, B. Chugh, E. T. J. Nibbering, T. Elsaesser, and R. J. D. Miller, "Ultrafast memory loss and energy redistribution in the hydrogen bond network of liquid H<sub>2</sub>O," *Nature*, vol. 434, p. 199, 2005.
- [130] D. E. Moilanen, E. E. Fenn, Y. S. Lin, J. L. Skinner, B. Bagchi, and M. D. Fayer, "Water inertial reorientation: Hydrogen bond strength and the angular potential," *Proc. Natl. Acad. Sci. USA*, vol. 105, p. 5295, 2008.
- [131] T. Steinel, J. B. Asbury, J. Zheng, and M. D. Fayer, "Watching hydrogen bonds break: A transient absorption study of water," *J. Phys. Chem. A*, vol. 108, p. 10957, 2004.
- [132] Y. L. A. Rezus and H. J. Bakker, "Orientational dynamics of isotopically diluted H<sub>2</sub>O and D<sub>2</sub>O," *J. Chem. Phys.*, vol. 125, p. 144512, 2006.
- [133] Y. L. A. Rezus and H. J. Bakker, "On the orientational relaxation of HDO in liquid water," *J. Chem. Phys.*, vol. 123, p. 114502, 2005.
- [134] V. V. Volkov, D. J. Palmer, and R. Righini, "Heterogeneity of water at the phospholipid membrane interface," *J. Phys. Chem. B*, vol. 111, no. 1377, 2007.



- [135] W. Wagner and A. Pruss, "The IAPWS formulation 1995 for the thermodynamic properties of ordinary water substance for general and scientific use," *Chem. Ref. Data*, vol. 31, p. 387, 2002.
- [136] C. Pinilla, A. H. Irani, N. Seriani, and S. Scandolo, "Ab initio parameterization of an all-atom polarizable and dissociable force field for water," *J. Chem. Phys.*, vol. 136, p. 114511, 2012.
- [137] K. Refson, "Moldy: a portable molecular dynamics simulation program for serial and parallel computers," *Comput. Phys. Commun.*, vol. 126, p. 310, 2000.
- [138] H. J. C. Berendsen, J. R. Grigera, and T. P. Straatsma, "The missing term in effective pair potentials," *J. Phys. Chem.*, vol. 91, p. 6269, 1987.
- [139] J. R. Schmidt, S. T. Roberts, J. J. Loparo, A. Tokmakoff, M. Fayer, and J. L. Skinner, "Are water simulation models consistent with steady state and ultrafast vibrational spectroscopy experiments?," *Chem. Phys.*, vol. 341, p. 143, 2007.
- [140] J. Errington and P. Debenedetti, "Relationship between structural order and the anomalies of liquid water," *Nature*, vol. 409, no. 6818, p. 318, 2001.
- [141] R. Bini, R. Ballerini, G. Pratesi, and H. J. Jodl, "Experimental setup for Fourier transform infrared spectroscopy studies in condensed matter at high pressure and low temperatures," *Rev. Sci. Instr.*, vol. 68, no. 8, p. 3154, 1997.



# Acknowledgements

Too many people to acknowledge, I'll try not to be mawkish. I wish to thank, first and foremost, Roberto Bini for the continuous support and for giving me the possibility to do all here reported. His guidance and paramount mentorship helped me in all the time of research. I cannot find words to express my gratitude to Margherita Citroni, together we shared all the wonderful good times and some bad times related to the immense work activity hiding behind those few pages. I would like to express the deepest appreciation to Andrea Lapini and Marco Pagliai, together with we produced and consumed a lot of fascinating, stimulating and intriguing things. I consider it an honour and a pleasure to work with all of you.

I would also like to thank for all the constructive discussions, for the collaborations, for the help and also for the very useful monkey wrench thrown in the works:

Matteo Ceppatelli, Federico Gorelli, Mario Santoro, Roberto Righini, Paolo Foggi, Paolo Bartolini, Andrea Taschin, Renato Torre, Demetrio Scelta, Agnese Marcelli, Mariangela Di Donato, Paolo Postorino, Silvio Sciortino and Sandro Scandolo (in casual order).

Thanks to all my real friends and my family for all that you have done.

Not worth mentioning:

```
samuele@bruco:~$ uname -nmov
```

```
bruco #1 SMP Debian 3.10.5-1~bpo70+1 (2013-08-11) x86_64 GNU/Linux
```

The word “pressure” was used 468 times.

---